Bridging the gap: fragmentation, filamentary feeding and cluster formation in the ISM

Bridging the gap: fragmentation, filamentary feeding and cluster formation in the ISM

By
Rachel Pillsworth, B.Sc.

A Thesis Submitted to the School of Graduate Studies in the Partial Fulfillment of the Requirements for the Degree Master of Science

McMaster University
Master of Science (2022)
Hamilton, Ontario (Department of Physics & Astronomy)

TITLE: Bridging the gap: fragmentation, filamentary feeding and cluster formation in the ISM
AUTHOR: Rachel Pillsworth (McMaster University)
SUPERVISOR: Ralph E. Pudritz
NUMBER OF PAGES: xi, 84

Abstract

Star formation is an inherently multi-scale process, connecting scales from the kiloparsecs of the galactic disk to the single AU scale of a protostar. In the middle of these scales are star clusters and molecular clouds, the structures in which most stars form. The clouds and clusters are connected via the interstellar medium, the gas and dust making up the matter between stars. In the cold phases of this medium rests the first steps of star formation, the formation of molecular gas and networks of filaments. This cold, neutral medium (CNM) hosts a handful of physical mechanisms, all contributing to the structures that feeds star formation. In this thesis work, we present a suite of simulations using the magneto-hydrodynamical code Ramses to investigate the role of turbulence, magnetic fields and cooling on the formation of filaments and clusters in the CNM. Through 9 different models we find that velocity dispersions in the CNM play a significant role in the formation of structure, requiring a balance between turbulence, self gravity and cooling to form filaments. We find magnetic fields, initialized at strengths of $7\mu G$, affect the formation of filaments, creating higher percentages of star-forming dense gas and lower percentages of molecular gas. Both magnetic fields and velocity dispersion in the gas affect the formation rate of clusters early in the simulation. Our 8 km/s simulations present a good initial condition for star formation that can include multiple scales of the process and recreate accurate clouds and filamentary structure.

Acknowledgements

First and foremost, to Ralph, I owe all my knowledge to you. Your guidance and supervision got me through this, even with all the bumps in the road along the way. Though I could never enumerate the ways you've taught me, you're the reason I am the scientist I am today and I am forever grateful for the patience and grace you approach all your students with.

To my fellow group members Kaitlin Cerrillo, Alix Dujardin, and Gillian Bogert. The camaraderie and support I've received from each of you means the world to me. I am glad we can get along so well and poke fun at Ralph in group meeting with ease. I would not have been able to get through some of the challenges of this thesis without you all to rant to.

To Davide Decataldo, Romain Teyssier and Bo Zhao for all the numerical technique and support you have all passed on to me during this thesis work. Most of what I present here could not have been done without your individual expertise.

To my friends, who mean the world to me. You know who you are, and I am so thankful to have each of you with me on this journey. Specifically to my roommates: the stress will only get worse in the coming years, I'm sorry in advance. Peanut butter toast will continue to fuel me most of the time, and I will always smother the kitten with affection.

To Alison, for giving me a chance. I never knew what I wanted or if I could survive academia until I worked with you. Thank you for being so sure you wanted to work with me, it set me on my path today.

To my sister, without whom I don't think I would have ever realized I could study physics, and who showed me what astronomy really is. I am infinitely in awe of everything you can do, and you are the best sister I could ask for. We don't do mushy, but I do love you so much. And I'm only half saying that so that your software engineering industry money will support me when I'm very poor.

Finally, and in no way least, thank you to my parents. I am so lucky to have parents who are cool, supportive and understanding. Though it's not chemistry, it's still pretty cool what I'm doing, you have to admit.

Contents

Abstract iii

Acknowledgements iv

Declaration of Authorship xi

1 Introduction 1

2 Review of Star Formation Theory & Magneto-Hydrodynamics 4
2.1 Elements of Star Formation . . . 4
2.1.1 The Interstellar Medium . . . 4
2.1.2 Molecular Clouds . . . 6
2.1.3 Star Clusters . . . 9
2.2 Magnetic Fields . . . 10
2.2.1 Magnetic Fields in the ISM . . . 11
2.2.2 Magnetic Fields and star formation . . . 13
2.3 Hydrodynamics & RAMSES Code . . . 14
2.3.1 Adaptive Mesh and Adaptive Time . . . 15
2.3.2 Hydrodynamics . . . 16
2.3.3 CLUMPFINDER . . . 18
2.3.4 Sink Particles . . . 18

3 The effects of CNM environment on filament and star formation 22
3.1 Introduction . . . 22
3.2 Bridging scales . . . 24
3.2.1 Filamentary Structures on Many Scales . . . 24
3.2.2 The transition of the CNM to GMCs . . . 28
3.3 Numerical Methods . . . 30
3.3.1 Physical Mechanisms . . . 30
3.3.2 Models . . . 32
3.4 Results . . . 35
3.4.1 When do massive clusters form? . . . 37
3.4.2 Molecular gas and cloud morphology . . . 42
3.4.3 Hydro vs. magnetic fields . . . 44
3.4.4 Angular Momentum and Filament Stability . . . 51
3.4.5 Magnetic Criticality of protoclusters . . . 56

3.5 Conclusion 56

4 Summary & Future Work **60**
4.1 Key results 60
4.2 Future work on the cluster scale 61
4.3 Future work on galactic scales 63
4.4 Summary 65

A Supplemental work **67**
A1 The Dispatch code 67
A2 The effects of box size 68

Bibliography **72**

List of Figures

2.1 250 μm wavelength image, depicting column densities $10^{21} cm^{-2} \leq N(H_2) \leq 10^{22} cm^{-2}$, in a $2° \times 2°$ region. Blue circles represent compact objects detected. Filamentary structure appears with lighter colour indicating high column density, and has estimated length scale of 2.8 pc. Image from Molinari et al. (2010). 5

2.2 Schematic of the process of Adaptive Mesh Refinement. Simulations start with a rough, low resolution grid, as in the top right of the figure, and as needed the code will impart more resolution in the form of greater patch density for those areas which need it, as in the bottom left. Figure taken from Schive, Tsai, and Chiueh (2010). 15

2.3 Visual representation of the steps in the clump finding algorithm written into RAMSES for the purpose of sink particle creation. From 1-6, areas over the threshold density are identified, then split into individual peaks based on local maxima. Peaks with little difference between them are relabelled as one clump. The process continues until every clump left is sufficiently distinguished from any other nearby clumps, and are then saved as a clump object, with individual masses and radii determined by peak properties. Figure from Bleuler and Teyssier (2014). 19

3.1 Image from Chevance et al. (2022). Orion A GMC dust emission map (grayscale) and $^{12}CO(1-0)$ emission (contour lines in position-position space. 29

3.2 Column density projections of our high resolution hydrodynamical bottoms at 4.4 Myr. *Top:* Model for our 5 km/s dispersion case. Projections in both the x and z plane are shown, with the center of our box centred at (0,0). *Middle:* Same as above, but for the 8 km/s dispersion case. Black filled circles show sink particle locations at any plane depth. *Bottom:* Projections for our 10 km/s dispersion case. As before, black filled circles represent sink particle positions at any plane depth. 36

3.3 Slices through the center of the box of our disp8 model with density (left) and temperature (right) plotted at a time of 4.5 Myr. Sharp filamentary features are seen in the density, which is mirrored in the black contours in the temperature, tracing the highest density gas ($\sim 10^3 cm^{-3}$ and above). 37

3.4 Sink formation over time for each of the three models and their three dispersions. We show the formation of the first ten sinks to form in each model, denoted by the coloured stars along the lines. Final number of sinks for the low resolution, hydro and MHD models are depicted as coloured pentagons, hexagons and octagons respectively. Coloured vertical lines show the point in time at which each group of velocity dispersions hit 10% of the initial global crossing time. This corresponds to one crossing time in a 100 pc patch, the scale of a molecular cloud. 38
3.5 Accretion rates of sink particles for the disp8LRes model. Multicoloured lines show individual sink particles' accretion rates, with their formation corresponding to the vertical portion of the line. Thick black line shows the mean accretion rate across all sink particles over time. Limits on the x axis have been adjusted to start just before first sink forms. 41
3.6 Side-by-side comparison of the molecular gas structure for the disp8 model. *Left:* Z-plane projection of gas, cut to contain only that above $10^{-21} g \cdot cm^{-3}$. Sink particles are represented by filled aqua circles. Maximum resolution is 0.2 pc, chosen to approach typical filament widths of 0.1 pc. *Right:* Same, with added contours to simulate observations of molecular gas structures. Contours are drawn from $10^{20} cm^{-3}$ to $10^{23} cm^{-3}$ to mimic resolution range of Lombardi et al. (2014). 43
3.7 Zoom-in of contoured region in Fig. 3.6. Density projection and contours are the same, though plotting has been recentered on the center of the location and the domain plotted is 150 pc. Sink particles are represented by filled aqua circles. 44
3.8 Density PDF for all 9 models at their final time. Minimum density is truncated to 0.1 cm^{-3}, maximum density is not truncated. Low resolution models are represented by dashed lines, while all 6 high resolution models are represented by solid lines. 45
3.9 Line integral convolution of magnetic field structure overlaid on density projections for each of our MHD models. From left to right: x, z and y projections of column density. Black lines show the magnetic field lines, while sink particles are represented by filled white circles. Magnetic field is initialized as a constant in the y-direction, such that z is perpendicular to the field. 47
3.10 Magnetic field magnitude maps for each of our MHD models. From left to right: x, z and y plane slices through the center. Sink particles are represented by white filled circles. 48
3.11 Density projections of the disp8 (top) and disp8MHD (bottom) models, at times with significantly sharp structure forming. Magnetic field lines are depicted by green streamlines, and both frames show simulation time in the bottom left. 49

3.12 *Top:* Pressure-density profiles of disp8 (blue line) and disp8MHD (orange line) models. *Bottom:* pressure-density profile of only the magnetic pressure of the gas in our disp8MHD model. Note the difference in scales, with magnetic pressure making up a small amount of the total pressure (maximum $10^4 Kcm^{-3}$. 50
3.13 Mass-weighted pressure-density phase plot of the disp8 model. The majority of the mass is found in median pressure, molecular to star-forming gas. 51
3.14 Same as Fig. 3.13, but for our disp8MHD model. 52
3.15 Angular momentum profile of gas throughout the box, moving radially outwards from the center, for our disp8MHD model. Both the individual components and total magnitude of the gas's angular momentum are plotted. Gold stars show the angular momentum magnitude of the sink particles and their radius from the center of the box. 53
3.16 Line mass ratio maps for a slice of *top:* our disp8 model and *bottom:* our disp8MHD model. White streamlines in the bottom panel show the flow of the magnetic field. Slices are taken for the x and z plane, as they showcase the most structure. Critical line mass is calculated as $M_{crit} = 2c_s^2/G$. Line mass is taken as cell mass/cell width and sampled for each cell, therefore providing a lower bound. 55
3.17 Normalized mass to flux ratio over time for the first ten sink particles to form in the disp8MHD (top) and disp10MHD (bottom) models. Mass to flux ratios are normalized against the critical ratio from Mouschovias and Spitzer (1976) which states $M/\phi_{crit} = (5/9G\pi^2)^{-1/2}$. 57

A1.1 Free-fall vs. crossing time for all dispersal test models. Red diamonds indicate those which dispersed their gas quickly and out of the box, blue diamonds indicate the tests which had collapsed to the center of the box. 70
A1.2 Time evolution of CNM gas set at a density of $50cm^{-3}$ and a crossing time of 20 Myr. No clusters form at any point in the evolution of the structure. All high density gas flows out of the box. 71

List of Tables

3.1 Parameters for all models computed. The first three models represent our fiducial models with no magnetic fields and maximum resolution of 0.48 pc. We set our magnetic field runs to have a field strength of 7 μG, in accordance with average values of ISM magnetic field strengths. The final three runs are set with lower maximum resolution (0.97 pc) in order to investigate sink particle evolution until 15 Myr. $\sigma_{turb,initial}$ and $\sigma_{turb,10}$ represent the velocity dispersion in the simulations on initialization and once 10% of the initial global crossing time has gone by, respectively. $\lambda_{J,thermal}$ and $\lambda_{J,kinetic}$ give the initial Jeans lengths of each simulation calculated using the average temperature and the velocity dispersion, respectively. 33

3.2 Masses and percentages of different gas cuts for both disp8 and disp8MHD models. From left to right: total gas mass above 100 cm^{-3} in solar masses, percentage of initial and final gas mass, same for cuts of 1000 and 10000 cm^{-3}. 42

A1.1 Relevant parameters set for dispersal testing in a 1 kpc^3 box on CNM gas. 68

Declaration of Authorship

I, Rachel Pillsworth, declare that this thesis titled, "Bridging the gap: fragmentation, filamentary feeding and cluster formation in the ISM" and the work presented in it are my own.

Chapter 1

Introduction

> Before we invented civilization our ancestors lived mainly in the open out under the sky. Before we devised artificial lights and atmospheric pollution and modern forms of nocturnal entertainment we watched the stars. There were practical calendar reasons of course but there was more to it than that. Even today the most jaded city dweller can be unexpectedly moved upon encountering a clear night sky studded with thousands of twinkling stars. When it happens to me after all these years it still takes my breath away.
>
> Carl Sagan, Pale Blue Dot: A Vision of the Human Future in Space

The stars we see in the night sky look isolated but, this is a consequence of eons of dynamical evolution after their formation in a galaxy. In truth, astronomers have known for many hundreds of years that stars reside in structures called clusters. These clusters are groupings of up to millions of stars. Observations of the frequency of very young clusters soon after they emerge from their parental gas clouds indicate that they provide the birth sites for individual stars, feeding their mass growth as a young protostar from their own gas reserves. In fact, these clusters form from even larger cloud-like structures of molecular hydrogen, called molecular clouds. Surveys show that 70-90% of all stars likely appeared as members of forming star clusters in molecular clouds (Lada and Lada 2003). Most young clusters are either gravitationally unbound after their remaining natal gas is dispersed, or are not bound enough to resist the galactic tidal field which gradually pulls them apart (Banerjee and Kroupa 2013). Astronomers understand that star formation as a physical process is connected to so much more than just the star it is forming. As a field, we have deciphered many questions surrounding star formation and, just like any good subject, the deeper you delve the more questions there are.

The interconnected nature of molecular clouds and star clusters has guided the way we have studied star formation, specifically of the stars within these structures. In particular, understanding the formation of massive stars requires an understanding of massive cluster and cloud formation. Massive stars, $>8M_{\odot}$, have been an enigma in star formation theory for some time now. Unlike their lower mass counterparts and despite their intrinsically higher luminosities, the fact that massive stars are very rare (1% of the total stellar population) means their formation sites are typically very distant and obscured by ionized gas, therefore making them more difficult to resolve. A lower mass star will form via local collapse in a star cluster, in which a dense pocket collapses to a small scale ($\sim$0.01 pc) and begins its protostellar phase. During this phase the protostar accretes material to grow in mass and eventually reach hydrogen burning and the main sequence, where it is officially a star. Massive stars, as far as we can tell, do not follow this path exactly. While they still form from dense pockets, we instead see larger scales, up to even 1 pc, for the clumps that form. Furthermore, given lifetimes of $\sim 10^5$ yr and observations of infalling gas at multiple physical scales, when massive stars form they are still interacting with their surroundings through accretion and radiation (Motte et al. 2018).

This idea of the massive protostar interacting with its nearby environment is further supported by hierarchical collapse scenarios, such as that outlined in Vázquez-Semadeni et al. (2009). In such theories, large scale collapses within a molecular cloud will create parsec-scale clumps. Within observational studies, these clumps have been described as hubs which represent intersections of filaments (described in both Kumar et al. (2022) and Motte et al. (2018)). It is within the massive hubs that massive star formation preferentially takes place (Schneider et al. 2012). These hubs receive gas inflow from the filaments creating them, with the densest filaments feeding the precursors to massive star clusters. In other words, the filamentary structure of a molecular cloud directly feeds the growth of a massive protostellar core, binding the various scales to each other. Given this, it is incredibly important to understand molecular cloud and star cluster formation in order to begin to further understand the formation of massive stars. Observations have been able to get us extremely far. We are able to observe anywhere from entire molecular cloud complexes with *Herschel* down to singular massive protostellar cores with NOEMA and the CORE team (Cesaroni et al. 2019). Yet, these observational views can only provide brief snapshots in time.

Collecting the whole picture is necessary in order to understand the physical processes contributing to the birth of our most massive stars; however, up until now the vast majority of simulations have presented only one or two scales of a problem. As we have just seen, massive star formation involves scales up to at least the molecular cloud ($\sim$100 pc) and down to the protostellar core. Due to previous limitations in computing, including this many physical scales in one simulation was once practically impossible. Many treatments of massive star formation have started at the scale of an idealized spherical cloud, treating massive cloud formation as a separate problem (Howard et al. 2018; Sakre et al. 2021; Grudić et al. 2022). Recently, large improvements in computing

have allowed for the inclusion of multiple physical scales. We suggest that the hub-filament structure of clouds and the large-scale interactions massive protostars have with their environment both push the necessity of analyzing the full range of scales in this problem. The separation between molecular cloud formation and massive cluster formation gives limited knowledge towards the birth sites of massive stars. In this thesis, we argue that the first step towards a better understanding of massive star formation is a better understanding of the links between clouds and clusters.

We will present our work towards bridging these scales in the following sections. Chapter 2 presents a review of the background information necessary for this thesis work. We will cover the interstellar medium, as well as the basics of molecular clouds and star clusters. We will give a brief description of the role of magnetic fields on the three scales mentioned above. We will also discuss the basic functions of the code we use, and explain in detail the two most important functionalities we include. In Chapter 3 we include our paper for publication, which will cover more detail introductory information, numerical methods & our models, as well as results and conclusions of the research. Finally, in Chapter 4 we summarize the results of this thesis work and outline the role they play in future work. We will discuss next steps in research and preliminary results of those efforts.

Chapter 2

Review of Star Formation Theory & Magneto-Hydrodynamics

2.1 Elements of Star Formation

In this thesis we present a view of star formation that extends much further than the single star. As a consequence of that, it is necessary to look at what scales exist above the star and how they themselves come about. In our view, there are three scales which are the most important to this work. We start at the interstellar medium, the initial scale of this thesis work. From there, we will explain the basic formation and properties of molecular clouds and star clusters, focusing specifically on the massive end of both scales. Through a hierarchical flow from interstellar medium to star cluster, we explain the basic physical mechanisms creating the environments for single stars to form.

2.1.1 The Interstellar Medium

The interstellar medium, henceforth referred to as the ISM, embodies the dust and gas components of matter present between stars. The medium is dispersed throughout a galactic disk and halo and hosts a variety of densities and temperatures, creating environments for various structures to form. These variations in density and temperature are described by the multiphase model of the diffuse ISM, consisting generally of stable phases of cold, warm and hot gas as observed in multiple studies of galaxies (Haffner et al. 2003; Lombardi et al. 2006; Arzoumanian et al. 2011). The ISM also contains cold (typically 10 K), dense ($n \geq 10^2 Hcm^{-3}$), molecular gas which is self-gravitating and in which stars are observed to form (McKee and Ostriker 2007). Structure in the ISM is formed from the intersection of supersonic shock waves, which will compress the gas and heat cold phases. This is driven by feedback processes including, but not limited to, supernovae explosions, massive star radiation, protostellar jets, turbulence and galactic shear (Lopez et al. 2011; Villagran et al. 2020; Lucas et al. 2020). Different types of feedback will be dominant in different galaxies. For example, Lucas et al. (2020) suggests that supernovae are the most important type of feedback for ISM evolution in Milky-Way type galaxies, whereas Combes (2017) suggests that in high-redshift (early

Universe) galaxies there is need for more than just supernovae lest your galactic disk be too luminous. No matter the feedback though, we always see a multiphase ISM.

As mentioned above, there are cold, warm and hot phases of the diffuse ISM. In this thesis we are particularly interested in how the cold diffuse phase evolves into much denser molecular gas structures where star formation takes place. This phase is called the cold neutral medium, or CNM. As the name suggests, it consists of cold gas, mostly neutral atomic hydrogen, that sits at temperatures of roughly 80 K. Average densities of the CNM are around 30 cm^{-3}. Perhaps the most important feature of the CNM, and indeed all phases of the ISM, is the fact that it is filamentary: composed not of smooth components of gas but rather observed to be organized into strands of denser material. This filamentary structure (see Fig.2.1) has been best studied and demonstrated from various *Herschel* surveys, including the Hi-GAL Milky Way survey (Molinari et al. 2010), which performed infrared observations of cold dust at the peak of its spectral energy distribution, from $70 - 500\mu m$.

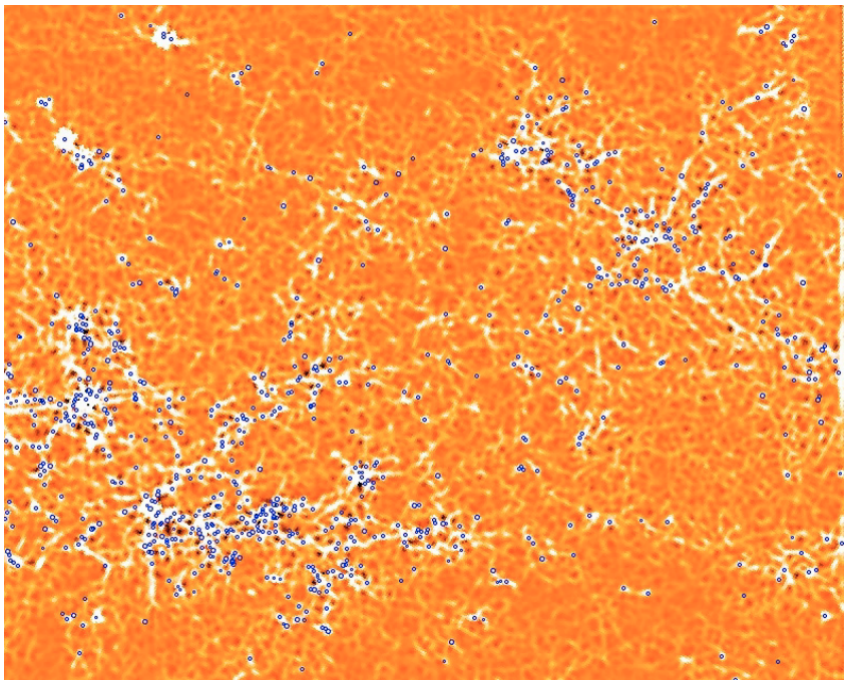

Figure 2.1: 250 μm wavelength image, depicting column densities $10^{21} cm^{-2} \leq N(H_2) \leq 10^{22} cm^{-2}$, in a $2° \times 2°$ region. Blue circles represent compact objects detected. Filamentary structure appears with lighter colour indicating high column density, and has estimated length scale of 2.8 pc. Image from Molinari et al. (2010).

At the intersections of these molecular gas filaments, clumpy structures form. On the scale of a molecular cloud, these clumps will be the star clusters that form within the cloud. The clusters are likely fed by the flow of matter along filaments, centralizing at the clump forming at intersections (Williams et al. 2018; Kumar et al. 2020), a concept we

will explore more in subsequent sections. Thus, the ISM may be intrinsically connected to molecular clouds and star clusters.

We argue that this environment leads the way on the properties of the molecular clouds that form. Furthermore, due to the inherent connection between clouds and their clusters via their filamentary structure, the ISM then may play a crucial role in the formation and properties of star clusters. Hence, an accurate understanding of the cold neutral medium in a simulation is essential for detailed cloud and cluster formation.

2.1.2 Molecular Clouds

Molecular clouds are collections of gas, primarily made up of molecular hydrogen, and dust, which result from the cooling of regions of the CNM with column densities sufficiently large ($\geq 10^{21} cm^{-3}$) such that molecular gas can self-shield from UV radiation. The observation of these clouds was not possible until Wilson et al. (1970) made their first detection of carbon monoxide in the Orion nebula. From that, a burst of observational work paved the way for molecular cloud studies, with more CO observations finding large complexes of molecular gas forming what we now call giant molecular clouds (or GMC's) (Lada 1976). The particular work of Lada (1976) found a molecular gas complex that measured 10×20 pc and more than $10^4 M_\odot$ in mass. The recent PHANGS surveys of molecular cloud populations inidcate molecular cloud masses range up to a million solar masses or more (Lee et al. 2022; Thilker et al. 2021; Sun et al. 2022). Perhaps the most interesting aspect of this observation though, was the fact that they determined this cloud could not be undergoing a uniform, global, spherical collapse.

Previous to this observation, clouds had been theoretically modelled as uniform, isothermal spheres of gas which, in order to create the structure we knew to be within them, had to undergo collapse. This collapse is motivated by the simple concept of hydrostatic equilibrium. For a fluid, there will be a balancing act between pressure and gravity. The pressure, providing internal support, comes about from thermal motions within the fluid. In equilibrium, this must support the gas against its own self-gravity. The balance between these two forces determines whether a structure is expanding, collapsing, or maintaining its form. For molecular clouds, this manifests in the virial balance. This balance is defined through the virial parameter:

$$\alpha_{vir} = \frac{2E_k}{U_g} = \frac{5\sigma_v^2 R}{GM} \tag{2.1}$$

for an isolated sphere of uniform density, where σ_v is the virial velocity in the sphere, R is the radius and M the mass, and the right-hand side of the equation is derived from the ratio of kinetic to gravitational potential energy. For a viriliazed cloud, we have $\alpha_{vir} = 1$, hence the name of the virial alpha parameter. Without considering any other external effects, this parameter also suggests that for $\alpha_{vir} \leq 2$ a cloud is dominated by its self-gravity and is considered gravitationally bound. A bound cloud will form structure, while an unbound cloud will expand and disperse throughout the ISM. In order to get a

feel for the kinds of virial velocities associated with bound clouds, we note that a cloud of mass $\sim 10^5 M_\odot$, radius $100pc$ and $\alpha_{vir} = 2$, we expect virial velocities of

$$\sigma_v = \sqrt{\frac{\alpha_{vir} GM}{5R}} \approx 1.3 kms^{-1} \tag{2.2}$$

Thus, on average, the typical massive cloud will have small internal velocities. Since observations of clouds showed non-uniform collapse, and observations from Herschel showed filamentary structure further supporting a local collapse scenario, a discussion of the global boundedness of molecular clouds has emerged.

For a parcel of gas to collapse due to gravity, it must overcome its Jeans mass, a minimum mass required for self-gravity to dominate and for compression to begin a run-away collapse scenario. The Jeans mass, for a spherical cloud, is defined:

$$M_J = \frac{\pi}{6} \frac{c_s^3}{G^{\frac{3}{2}} \rho^{\frac{1}{2}}} \tag{2.3}$$

Where c_s is the sound speed of the gas and ρ the density. For a cloud without a uniform density, the denser areas will begin collapse before the lower density areas, causing a scenario we call local collapse. Shock waves arise throughout the cloud at similar times, propagating through the medium. They collide with each other at different times and different locations in the cloud which is why we see clouds fragment into filamentary networks and form sub-structures throughout the volume at different times. It is also this local variation within clouds that makes determining the virial parameter and, as a consequence, its boundedness difficult.

Furthermore, using the virial parameter to estimate whether or not a cloud is bound soon showed that the critical assumptions underlying the theory were incorrect. Based on the concept of an isolated, uniform density sphere a cloud should be undergoing a monolithic collapse scenario, which would create just one central cluster in the cloud. Introducing non-uniform density distributions, with the most common choice being a density profile of $r^{-3/2}$, is essential to preventing global collapse and allowing the sphere to fragment to form many clusters throughout (McKee and Ostriker 2007). Another issue with monolithic collapse arises when we consider the efficiency of star formation. Though clouds are observed at only a few percent ($0.5 - 2\%$, as in Johnstone et al. 2004; Young et al. 2006), the monolithic collapse scenario requires clouds to have efficiencies of 50% or greater (Ramírez-Galeano et al. 2022). Thus, we instead favour the scenario of localized collapse and internal support, allowing the cloud to fragment. In McKee and Ostriker (2007), they describe the scenario of molecular clouds being supported by internal mechanisms adding to the thermal pressure effects. This scenario is now the popular scenario for molecular cloud formation theory, and introduces to us a possible modification to the sound speed which is, for the case with no magnetic fields is

$$c_{s,eff}^2 = c_s^2 + \frac{1}{3}\sigma_v^2 \tag{2.4}$$

where σ_v is the 3D velocity dispersion due to non-thermal effects. By introducing these non-thermal motions, we can see an increase in the Jeans mass of the cloud, thereby correcting it so that clouds must be higher mass in order to collapse, balancing the percentage of clouds that should collapse. The non-thermal motions acting as support to a cloud also represent the physical mechanism to explain the localized collapse scenario, wherein non-thermal motions cause non-uniform densities in clouds, leaving only small areas of high density that overcome their local Jeans mass while other areas of the cloud are lower density and, therefore, below their Jeans mass.

With the consideration of both thermal and non-thermal motions, the virial parameter now becomes essential to determining whether gravitational collapse or turbulent support is the most dominant, and we now notice the velocity dispersion in the equation represents the 1D velocity dispersion in the cloud, acting as a proxy for overall kinetic energy. Although, even with this distinction of motions, issues still arise. We note that the gravitational energy used in the virial parameter is the gravitational energy of an isolated, uniform sphere, whereas actual molecular clouds are neither uniform density spheres nor are they isolated. Instead, clouds have been observed to be oblong with radial density distributions (see Figure 1 of Chevance et al. 2022). We also point out the various works in both observations and numerical simulations, that show that the virial parameter does not accurately determine whether or not a cloud has converging motions (see, for instance, Bertoldi and McKee 1992; Vázquez-Semadeni et al. 2008; Padoan et al. 2016). These two points combined to push the field towards a more realistic view of molecular clouds, namely that they are not spherical and isolated.

The morphology of molecular clouds has been shown in numerous observations, typically depicting fragmented, filamentary clouds in elongated cigar shapes, instead of the toy model of a uniform sphere (André et al. 2014; Alves de Oliveira et al. 2014; Pineda et al. 2022; Hacar et al. 2022). This changes how we consider the physical mechanisms inside the cloud. In particular, André et al. (2014) discussed the formation of molecular clouds through the collapse of a sheet-like section of gas in a galactic disk, creating clouds that were overall flatter and more disk-like in shape. This is also a pertinent result we find in our galactic-scale work from Zhao et al. (2022, in prep.). Modern interpretations of cloud collapse and formation combine the ideas of global and local collapse. We can consider a packet of molecular gas, ready to form a molecular cloud. In Vázquez-Semadeni et al. (2019), a large-scale global collapse will begin as gravity is initially strongest. But, they note that when turbulent motions in the cloud become strong enough, the motions can balance the gravity, supporting the cloud on a global scale. Meanwhile, smaller, dense pockets of the cloud will overcome their local turbulent support and collapse and fragment, leading to star forming cores and clusters. This model matches well with observations of molecular cloud complexes, and highlight the physical connection between all scales of star formation. In our work, we will show that

this model is reproduced in our simulations, further supporting the connection from ISM down to single stars.

2.1.3 Star Clusters

In the same work of Lada (1976) mentioned in the previous section, there was a hypothesized connection between the molecular cloud complex and a star cluster located within it, NGC 6618, that rested in a high density filamentary area. A popular way to distinguish forming star clusters is the difference between embedded and exposed clusters (as in Lada and Lada 2003). The exposed clusters are so named as they contain little to no ISM gas within their structure. Their stars are done forming, and the cluster is left to evolve dynamically and eventually disperse due to tidal interactions with the galaxy. The embedded clusters, on the other hand, are still embedded in the gas from their natal molecular cloud, actively accreting more of it and gaining mass to feed the forming protostars they host. These may also be called protoclusters, as we will refer to them from now on.

The vast majority of protostars in a cloud will form within only a few very rich embedded clusters, usually the most massive ones (Lada and Lada 2003), such that the anywhere from 70-90% of stars form in embedded clusters. This corresponds well even to present-day theories of star formation, wherein clusters form from the collapse of molecular clouds, forming out of local overdensities along filaments throughout the molecular clouds. Protostars then form from a similar collapse that takes place within the clusters, such that the protostars are linked through filamentary networks all the way to the ISM gas that starts the chain. This scenario naturally explains the variation in cluster environments we observe. While some embedded clusters contain mostly cold, dense molecular gas having only just formed from the molecular cloud (observations of these clusters are often performed at infrared wavelengths, such as in the work of Hennemann et al. 2010), others contain large amounts of hot, HII gas, as the massive protostars within them have started forming, which can be observed in the work of Cesaroni et al. (2019).

The formation of star clusters is usually described using a simple model that features the collapse of a spherical, isothermal clump of gas formed in the filamentary network of a molecular cloud, with typical surface densities of $100 M_{\odot} pc^{-2}$ (Krumholz et al. 2019). Their initial masses follow a cluster mass function (CMF), which describes the range of initial masses one can expect of a population of clusters. This function can be described by a truncated power-law, with the upper mass cutoff varying based on the region observed. The CMF will depend very strongly on the efficiency of the conversion from molecular gas to stars. For a free-fall time defined as t_{ff}, we can define an efficiency per free-fall time

$$\epsilon_{ff} = \frac{\dot{M}_* t_{ff}}{M_g} \tag{2.5}$$

where M_g is the gas mass in the cloud, $\dot{M}_*$ the rate of star formation, and we ignore the effects of winds for simplicity. For this very simple assumption of efficiency, we expect a general efficiency of only a few percent, signifying that the transition to star formation is an inefficient process, leaving us with clumps that may never turn to star clusters (Johnstone et al. 2004). The observations suggest that clusters contain filaments on even smaller scales, which may feed individual stars in formation. Therefore, the idea of global collapse of a sphere is not an obvious solution to how clusters form, though it is still a useful guide for some purposes.

However, clusters have been described by the Bonnor-Ebert sphere (Bonnor 1956), a model which describes the instability of an isothermal sphere which causes it to collapse. Though this model likely does not describe the actual collapse happening in a cluster, it gives an interesting model for the balance between surface gravity and central gravity. The most important parameter in this model is the ratio of central density to surface density λ. For smaller values of λ, where surface gravity and central gravity begin to balance each other, the spheres are stable against collapse. It is only as the central density climbs to high values compared to the surface that these spheres collapse. This provides a neat description of star clusters in a mathematical model, as we know that the lower density clumps which first form will not immediately collapse. Rather, they will collapse local as pockets of overdensities develop, just as in clouds. This can also provides support to the representation of star clusters as sink particles.

As is discussed in the numerical methods of this thesis both in Sec. 2.3 and Chap. 3, we aim to represent clusters as sink particles in this thesis work due to resolution limits. We can ensure that our sink particles represent only those clumps of gas that will form stars, and therefore become star clusters, because of the Bonnor-Ebert sphere. In the case of a star cluster, the Bonnor-Ebert sphere will collapse, and therefore trigger star formation, due to high central densities. In the case where a clump of gas does not collapse, it will never trigger star formation. These clumps will not become sink particles because of this missing collapse criteria, and therefore do not meet the standards of sink formation as outlined in Federrath et al. (2010a). In this way, the use of a Bonnor-Ebert model for sink particles means we can consider only star-forming clusters in this work. This is also the limit to how much we consider the internal structure of clusters, where the nature of sink particles as numerical tool necessarily force us to assume that these are simply dense, spherical objects. We place considerations into radiation effects and stellar mass distributions in future work, and so do not discuss them here.

2.2 Magnetic Fields

Magnetic fields are a crucial mechanism in star formation problems, affecting all the scales from the galactic disk down to the star cluster. They also remain a poorly understood factor in star formation problems, with many technical details still needing to be deciphered. However, we have been able to make progress in the investigations of magnetic fields, learning many important effects they play in fragmentation, collapse and accretion.

When we discuss magnetic fields as a theoretical concept, it is important to keep in mind the limitations in observing them as well. While full 3D information is easy to come by in simulations, the mapping of magnetic fields with various observational techniques have really only just begun being able to map fields in their 3D orientations (see, for instance Tahani et al. 2022; Tahani et al. 2019; Tahani et al. 2018, and references therein). Furthermore, magnetic field observations are further complicated by our limitations in observing field lines only in parallel and perpendicular components. Our knowledge of 3D orientations and strengths relies solely on our ability to extract the information from a set of planar data points and strengths.

Magnetic fields have a variety of techniques for observation, though only a few of them are popular. One method uses the Zeeman effect on emission lines to observe magnetic fields along the line of sight (Crutcher and Kemball 2019). Research has found that weakly magnetized ISM gas has a shifted 21-cm line emission due to high ($\sim 10^4$ K cm^{-3}) magnetic pressures in diffuse media (Draine 2011). This shift will be systematic, the same at every point based on the field strength and, therefore, magnetic pressure. Shifted lines can be compared to known 21-cm lines, and we use the magnitude of the shift to determine field strengths. Another method of observation looks at polarized thermal dust emission. In magnetized gas, dust grains will align with their minor axes aligned parallel to the magnetic field, which can create a net linear polarization on the light we observe perpendicular to the magnetic field lines (Sullivan et al. 2021). This polarization can map the magnetic field in a region, provided the gas density is somewhat suitable. In high density gas, there is a greater rate of scattering and absorption events, such that the alignment between dust grains and the magnetic field could be less efficient and give larger errors on magnetic field measurements and mapping. As well, weakly magnetized gas will have more disordered fields, such that dust grains have little resistance to turbulent motions, making measurements more difficult as one needs sufficiently higher resolution to see the small, erratic changes in field orientation (King et al. 2019).

2.2.1 Magnetic Fields in the ISM

In the ISM, large scale effects from magnetic fields on the flow of fluid can be seen. The median field strength for gas of densities $10^4 cm^{-3}$ is $5\mu G$, though some areas, such as the HI region around the Orion A GMC, can have stronger fields on the order of $10\mu G$ (Draine 2011). These changes in field strength do not happen suddenly, but rather the magnetic field flows with the rest of the gas, ending up in naturally stronger collections, just like the gas will collect into overdensities. The description of the magnetic field's strength can be represented through the Alfvén waves, which are transverse waves propagating along the field lines, representing magnetic energy as opposed to thermal energy. These Alfvén waves have a propagtion speed of

$$v_A = \frac{B}{\sqrt{4\pi\rho}} \tag{2.6}$$

and the relative strength of the magnetic fields to the turbulent motions in the gas is given by $(v_A/\sigma_v)^2$. When the numbers are comparable, such that the ratio is no more than a few tens and no less than 1, then the magnetic fields are dynamically important in the gas, helping to create filamentary networks by squeezing the gas together. When the magnetic field is much greater than turbulent motions, it dominates the diffuse medium, and no other mechanisms can overcome them.

In simulations of purely hydrodynamical galactic disks, the fragmentation of the medium will create spirals in the galactic disk, with short filaments within the arms of the spirals. Körtgen et al. (2019) showed that the addition of magnetic fields changes this fragmentation pattern, creating longer filamentary structure that can quickly create massive clouds. In comparing field strengths, they found that while their inclusion at all will delay the onset of fragmentation, the stronger fields cause earlier fragmentation due to the shortened timescale to reach Parker instabilities forming magnetic field loops. The inclusion of magnetic fields also worked to speed up the transition to star-forming gas, overall increasing the amount of mass formed into stars. Finally, they found that magnetic fields can act to bulk up the scale height of the disk, pushing cold (20 K), dense ($10^4 cm^{-3}$) gas to heights of several hundred parsec, spreading out especially the CNM material in a disk.

Whereas Körtgen et al. (2019) performed simulations of an entire galactic disk, local shearing boxes have also found a thickened disk plane height, such as in Girichidis et al. (2018). In their investigation of magnetic fields, the authors find the scale height is increased, with especially the cold gas being expanded further out. Investigating the effects the magnetic fields have on star formation, they also find that magnetic fields contribute to a delay in the onset of fragmentation, but point out that this seems to be primarily for the cold, dense gas as well, implying the magnetic fields are dynamically important specifically at the CNM stages, and less so at warmer stages. They find overall fewer clumps form in the magnetized gas, and that these clumps will accrete material parallel to the magnetic field, possibly lending to higher accretion rates overall and explaining the higher masses expected. We note here that the higher masses are a consequence of the magnetic fields, and not the other way around, as observations have shown that the orientation of the magnetic fields does not depend on the mass distributions (Houde et al. 2004).

In the densest regions of the ISM, where clumps form, the typical magnetic field strength is roughly $6\mu G$, though this value has large scatter, as the strength varies greatly and is not solely dependent on density (Banerjee et al. 2009). In fact, while the field strength is higher in clumps than, say, the warm neutral medium, we also tend to see alignment between the velocity and the field lines, especially when this alignment can favour the flow of material into denser areas to form clumps. Overall, the magnetic field will tend to make the formation of clumps and therefore, stars, more efficient on the ISM scale, while also allowing it to support the gas for a longer time before fragmentation occurs to allow more mass the accumulate in the area overall.

2.2.2 Magnetic Fields and star formation

This brings us now to the question of how magnetic fields can affect star formation. Just as they do on the ISM scale, magnetic fields reduce fragmentation on scales of 0.1 pc, especially during the earliest stages of star formation (Commerçon et al. 2012). Additionally, as cores collapse into protostars, the increased pressure produced from the compression of gas during said collapse will produce stronger magnetic fields, increasing the magnitude of the local magnetic field around the core. In fact, stronger fields tend to produce fewer cores that are, on average, more bound and higher mass (Sakre et al. 2021). However, we know that magnetic fields also tend to support gas against collapse, so strong fields around cores should seem to prevent star-formation from taking place as the cores are unable to collapse. The collapse support can be best defined through the mass to flux ratio, M/ϕ, of the cores.

We define the magnetic flux as the surface integral of the magnetic field, such that we have

$$\phi = \int_S \mathbf{B} \cdot d\mathbf{S} \tag{2.7}$$

where $\mathbf{B}$ is the magnetic field and $\mathbf{S}$ the surface area vecto. We can approximate the mean magnetic field to be of the form

$$B_{mean} \approx \frac{\phi}{\pi R^2} \tag{2.8}$$

where ϕ is the magnetic flux and R is the radius of the area, such that we can say $\phi = \mathbf{B} \cdot \pi R^2$. In the simplest form, the mass-to-flux ratio is just this. We divide the mass in an area by the magnetic flux coming into an area to get a measurement. However, this tells us very little about the core in any sort on intuitive way. Instead, we can compare these measurements to a *critical* mass-to-flux ratio. This critical value will be based on the critical mass of an area for collapse to take place, comparable to the Jeans mass. There are two commonly accepted critical mass-to-flux ratios. From a virial analysis of a collapsing, magnetized cloud, Mouschovias and Spitzer (1976) gives a critical ratio defined as

$$\frac{M}{\phi} = \frac{1}{\pi}\left(\frac{5}{9G}\right)^{\frac{1}{2}} \approx 0.13 G^{-\frac{1}{2}} \tag{2.9}$$

On the other hand, from perturbation analysis, Nakano and Nakamura (1978) find a critical ratio of

$$\frac{\sigma_0}{B_0} \approx \frac{M}{\phi} = (4\pi^2 G)^{-\frac{1}{2}} \approx 0.16 G^{-\frac{1}{2}} \tag{2.10}$$

Both critical values give reasonable estimates of critical masses for collapse, and thus neither is preferred over the other in the field. When we compare our measured ratios to the critical values, we can now discuss the criticality of the collapsing core. For a value greater than 1 in the ratio of measured to critical values, we can describe the core as *supercritical*. When a core is supercritical, the magnetic field alone is not enough to support the core and it will collapse. On the other hand, we can have a *subcritical* core, where the ratio is less than 1. In this case, the core is adequately supported by the magnetic field and will not collapse. For a core of $1M_{\odot}$ in gas of mean field strength for the ISM of $5\mu G$ (Draine 2011), the mass to flux ratio is three times lower than critical, meaning the core is greatly supported against collapse. However, we know collapse must take place for cores with these properties, as we know that star formation must happen. But how does a core change its mass to flux ratio?

Within a collapsing cloud core, the forming protostar is surrounded by an accretion disk from which it gains its material, where we know that the magnetic field lines and the velocity direction will align. Where the flow aligns with magnetic fields, it is unimpeded by magnetic pressure, such that it can flow easily from accretion disk to core if the magnetic fields are aligned correctly. When these are not aligned, the accretion rate will be suppressed by the magnetic field, due to pressure impeding the flow perpendicular to field lines. Sufficiently strong magnetic fields can suppress accretion rates by a factor of $\beta^{\frac{1}{2}}/4$, with β the plasma beta comparing magnetic field strength to gravitational strength (Cunningham et al. 2012). Mouschovias and Spitzer (1976) and Nakano and Nakamura (1978) both assumed a frozen magnetic field, conserving the mass to flux ratio of the collapsing core. Instead, we can consider the idea that this magnetic flux is not frozen.

This changing field strength can be attributed to turbulent ambipolar diffusion. In this process, magnetic field lines are coupled to the charged particles in a gas - the electrons, ions and the charged dust grains. Thus, the drift of these charged particles away from the core will also carry magnetic field lines away, lowering the field strength and allowing for collapse (Draine 2011). As accretion takes place, gas is pulled in dragging the magnetic field with it. This will increase the magnetic field gradient and therefore change the mass to flux ratio as the magnetic field near the cluster strengthens. Initial collapse will also pull a lot of material towards the core, strengthening the magnetic field. With sufficiently strong magnetic field, collapse is halted and accretion is suppressed. The lower activity around the core allows for particle drift to occur again, which lowers the magnetic field accordingly. This cycle will repeat until enough collapse has taken place to form a protostar, at which point the mass to flux ratio does not matter as much for star formation. Accordingly, this means that magnetic fields can slow down the star formation process, just as they can slow down the fragmentation process.

2.3 Hydrodynamics & Ramses Code

Ramses (Teyssier 2002) is a combination N-body and hydrodynamical code designed for high resolution studies of astrophysical fluids, primarily on the cosmological scale. The

codes implements N-body solvers similar to those found in the ART code (Kravtsov et al. 1997), coupled with a tree-based method of adaptive mesh refinement (AMR) adopted from Khokhlov (1998b). It also features an adaptive time scale for faster simulations.

2.3.1 Adaptive Mesh and Adaptive Time

The AMR method has been discussed in numerical simulations since the 1970's (see Berger and Oliger 1984). It is a widely used method to produce higher resolution in areas of importance in grid-based simulations. On a grid-based code, the area of simulation is split up into cells, with the first iteration of cell formation being an even division across the simulation's 3D box, creating uniform cell sizes. With time, certain cells will become much denser than others, meeting an outlined set of criteria for refinement usually based on density or temperature gradients. Upon refinement being called, the cell is split into smaller cells, like boxes within a box, see Figure 2.2. Each of the new, smaller cells adopt properties based on interpolation and continuity criteria to link the smaller cells to the larger ones surrounding them.

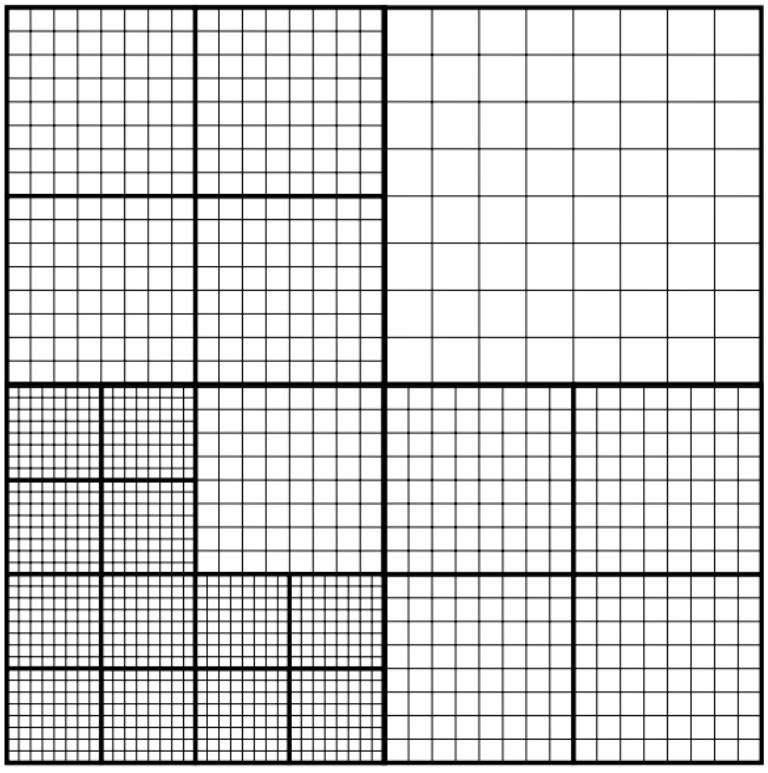

Figure 2.2: Schematic of the process of Adaptive Mesh Refinement. Simulations start with a rough, low resolution grid, as in the top right of the figure, and as needed the code will impart more resolution in the form of greater patch density for those areas which need it, as in the bottom left. Figure taken from Schive, Tsai, and Chiueh (2010).

In Ramses, the AMR method is carried out in a data structure called a "Fully Threaded Tree", adopted from Khokhlov (1998b), in which the elements are no longer single cells. The elements we now look at for refinement are *octs*, a group of 2^{dim} cells. The base grid, called the coarse grid, is the usual Cartesian setup of other grid-based codes and is set to be the zeroth level. Each subsequent level is one of refinement, where cells are refined by being broken up into octs, creating a new level. Each oct is assigned to a level of the mesh, and each points to the previous and next octs in the level's list, as well as their parent cell, the neighbouring parent cells and all the child cells in the next level (set to null in the instance of there being no child cells). This double linked list allows every oct of a given level to be accessed easily at each timestep, thus allowing for dynamic mesh refinement. Refinement criteria are defined by the user, then carried out only if the oct flagged for refinement is surrounded by $3^{dim} - 1$ parent cells. This rule forces a smooth transition between levels in all directions

Further mesh smoothing is carried out by a cubic buffer expanded around the cells marked for refinement, as described in Kravtsov et al. (1997). The key difference between Ramses and ART, in this case, is that Ramses makes use of *buffer cells* (or ghost cells) around their cells in a map, which also helps to smooth the mesh by containing edge information, so the smoothing operator is applied only once by default, as opposed to ART where it is applied twice.

Within this AMR structure is the link to the adaptive time step applied in Ramses. There are two different time steps in the code: the coarse and the fine time steps. A typical time step implementation in hydrodynamics codes is defining an amount of time Δt as a global parameter, thus applying to all levels, then integrating the equations of hydrodynamics from t to $t + \Delta t$. The adaptive time step follows similarly, this time describing a Δt value for each level, determined by a stability condition to determine the largest possible time step without neglecting major changes. Times are then synchronized by having each finer level advance some multiplier of the time steps as the level before, as defined by the user. In this work, a value of 2 is used, such that each fine level advances twice as many as the coarser level above. For example, for one coarse time step at level 0, level 1 is advanced by two of its time steps, level 2 by 4 of its time steps, and so on.

2.3.2 Hydrodynamics

Ramses chooses to solve the Euler equations in their conservative forms, the main advantage of these forms being that the energy equation, minus gravity source terms, will be conservative for the total fluid energy. This means that energy sinks due to numerical affects will not affect or alter the flow dynamics of the gas being simulated. The Euler equations are given as follows:

$$\frac{\partial \rho}{\partial t} + \nabla \cdot (\rho u) = 0 \tag{2.11}$$

$$\frac{\partial}{\partial t}(\rho u) + \nabla \cdot (\rho u \otimes u) + \nabla p = -\rho \nabla \phi \tag{2.12}$$

$$\frac{\partial}{\partial}(\rho e) + \nabla \cdot [\rho u (e + p/\rho)] = -\rho u \cdot \nabla \phi \tag{2.13}$$

where ρ represents mass density, u the fluid velocity, p the thermal pressure, e the specific total energy and ϕ the gravitational potential. These equations are solved on octs, not single cells, at any given level thus needing $3^{dim} - 1$ neighbours to define boundary conditions. With the boundary conditions provided, the code uses a Piecewise Linear Method to solve Euler's equations (as seen in Toro 2009), adapted specifically from the works of Colella and Woodward (1984) and Saltzman (1994). At some time t, second-order, time-centered fluxes are computed at the interfaces of cells with an approximate Riemann solver. This creates the "Godunov states". Then fluxes of the conserved variables are calculated using these states, which are then the fluxes of variables across cell interfaces. The inclusion of ideal and non-ideal magnetic field affects is also an option in RAMSES.

When including magnetic fields, the equations of hydrodynamics necessarily change. Their new Eulerian are derived as

$$\frac{\partial \rho}{\partial t} + \nabla \cdot (\rho u) = 0 \tag{2.14}$$

$$\frac{\partial \rho u}{\partial t} + \nabla \cdot (\rho u \otimes u - B \otimes B + P_{tot} \mathbb{I}) = 0 \tag{2.15}$$

$$\frac{\partial E_{tot}}{\partial t} + \nabla \cdot [u(E_{tot} + P_{tot}) - B(B \cdot u)] = 0 \tag{2.16}$$

where E_{tot} is the fluid's totaly energy per unit of volume and P_{tot} is the total pressure. Even with this form of the hydrodynamic equations, the Godunov scheme can directly apply (Fromang et al. 2006), and the majority of the information of the flow is transcribed through waves. The inclusion of magnetic fields in the flow will bring with it the Alfven wave, as well as two modifications of sound waves: fast and slow magnetosonicwaves (Teyssier 2015). Due to the increased complexity of the flows, a different solver for the equations must be chosen. In RAMSES, the Harten-Lax-van Leer solver with discontinuities (HLLD) is chosen, which is the most popular choice for astronomical MHD codes. There has been some work on including non-ideal MHD effects, such as ambipolar diffusion (see Masson et al. 2012), which will change the total energy in the fluid, but for this thesis work we ignore these additions as they provide negligible effects on this scale.

2.3.3 CLUMPFINDER

A unique aspect of Ramses is the built-in clump finding algorithm, which can be coupled with their sink particle implementation to estimate high density structures that cannot be resolved. I discuss the sink particles in further detail in the following section, and save this section to detail ClumpFinder, as described in Bleuler and Teyssier (2014) and based on the algorithm given by Bleuler et al. (2015).

In an extension of the 'peak-based' method from Federrath et al. (2010a), Ramses uses the ClumpFinder code to identify density peaks. This module can be used alone for tagging clouds or in combination with the sink particle implementation to create sink particles. In peak-based methods, every density peak in a simulation is considered for sink formation. The clump-based method instead requires the peak to meet a threshold of topological prominence. When peaks fail this criteria they are considered noise; however, when they meet the criteria they can be further considered for sink particle implementation. The greatest benefit of this method is a lower amount of sink particle formation, preventing spurious sink formation in a simulation for any single cell that matches the criteria.

The steps to finding clumps for sink formation are straightforward. They can be visualized in Figure 2.3, and I will describe them in slightly more detail here. For greater detail of the algorithm, the reader is encouraged to review Bleuler et al. (2015). First, every cell with a density higher than a user-defined threshold is marked as a potential clump. Each of these cells is assigned to a density peak by grouping cells according to the peak ID of their densest neighbour. This can be seen in subfigure 2 of Figure 2.3.The saddle points between all peaks are identified and the values are put in a matrix. By comparing the ratio between the peaks and their saddles, the code decides whether the peak is significant or if it is noise given a user-defined relevance threshold, in this work set to an integer value of 6. Peaks deemed to be noise are merged to their nearest significant peak with the highest saddle point. Completely isolated insignificant peaks are disregarded. The final list of clumps contains only the most significant peaks and whichever of the insignificant ones merged with another peak ID.

2.3.4 Sink Particles

Using the clumps found by ClumpFinder requires further checks to verify it is a viable site for sink particle formation. First, the code will trim out a volume in the clump equal in size to that needed to form a sink, which will be approximately equal to the accretion radius of the sink, defined as 2 cells at the highest level of refinment. The most common rules of sink particle formation are those used in Federrath et al. (2010a), listed here now:

1. Must be above a set density threshold
2. The simulation must be completely done refining, i.e. the AMR must have hit the highest level of refinement

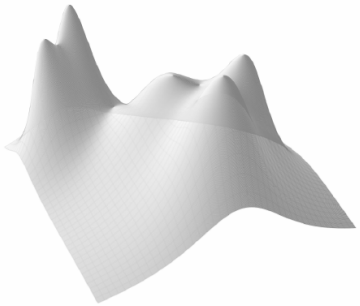

Figure 1.

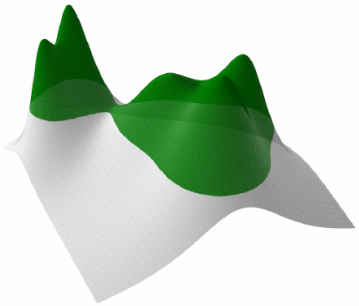

Figure 2.

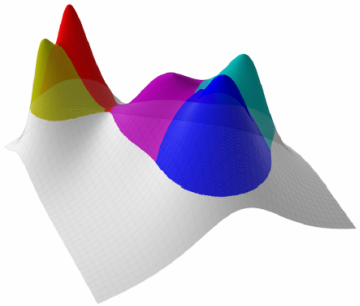

Figure 3.

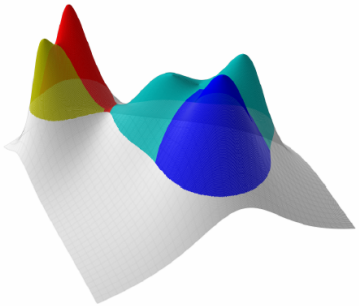

Figure 4.

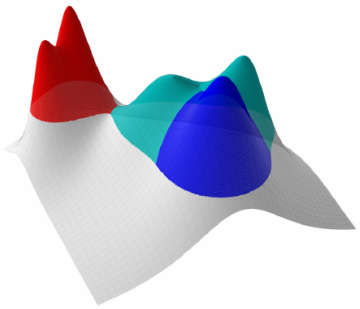

Figure 5.

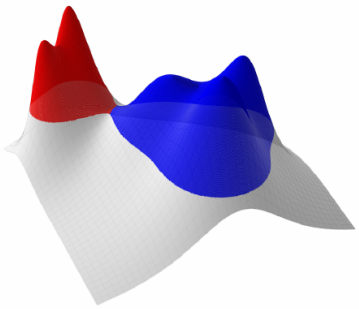

Figure 6.

Figure 2.3: Visual representation of the steps in the clump finding algorithm written into Ramses for the purpose of sink particle creation. From 1-6, areas over the threshold density are identified, then split into individual peaks based on local maxima. Peaks with little difference between them are relabelled as one clump. The process continues until every clump left is sufficiently distinguished from any other nearby clumps, and are then saved as a clump object, with individual masses and radii determined by peak properties. Figure from Bleuler and Teyssier (2014).

3. The region must be located at a (local) gravitational minimum
4. It must be in a region of converging flow, such that more gas is flowing into the region
5. The region must be Jeans unstable, defined by the gravitational energy being greater than twice the thermal energy
6. The region must be gravitationally bound, such that total energy in the volume is negative
7. The region may not be within the accretion area of another particle

Some of these criteria, such as the density threshold and the AMR level, are carried out by virtue of how ClumpFinder runs. Others are completely disregarded in Ramses, with the authors citing either no physical reasoning or a redundancy. The checks which the authors abandon are the bound state check, the Jeans instability check and the potential minimum check. Specific reasoning for each case is outlined in the sink algorithm paper (Bleuler and Teyssier 2014). The checks the authors do choose to keep are the virial (boundedness) check, the collapse (converging flow) check and the proximity check, stating that these are sufficient to define sink particles as sub-grid, collapsing points of interest.

In the virial check, the gas surrounding the density peaks but still contained in the clump is checked for whether it is gravitationally collapsing. The check is performed through a virial theorem analysis on the gas, which will determine the balance between gravitational and internal (such as thermal pressure) support in the gas. This is similar to the derivation found in Chapter 3 of Stahler and Palla (2005). The collapse check verifies that the volume of gas is both accelerating towards the center and contracting along the principal axes. This is done by defining a collapse timescale associated with each axis and determined by the eigenvectors of the second moment of the center of mass frame's scalar moment of inertia, defined as

$$t_i = \frac{\lambda_i}{\left(\frac{d\overline{\overline{I}}_{cm}}{dt}\mathbf{e}_i\right)\cdot\mathbf{e}_i} \tag{2.17}$$

where λ_i is the eigenvalue of the i-th direction, $\mathbf{e}_i$ the eigenvector of the i-th direction and $\overline{\overline{I}}_{cm}$ is given by

$$\overline{\overline{I}}_{cm} = \int_{\Omega_i} \rho \mathbf{r}_{rel} \otimes \mathbf{r}_{rel} dV \tag{2.18}$$

The timescales in all three directions (for a 3D simulation) must be negative to pass the collapse check for sink formation. The final check is the proximity check. Gas that is already accreting onto a sink particle cannot form a sink particle of its own, even if it passes all other checks for sink formation. In Ramses, the gas must be outside of

an accretion radius, defined as a radius of 2 cells around the sink particle at its highest resolution, to be allowed to form a sink. But if a newly formed sink stays very close to another for a time longer than its collapse time, there is a possibility the two sinks will merge with each other.

How sinks merge in Ramses is also handled slightly differently from other implementations of sink particles. Similar to Federrath et al. (2010a), the authors believe sink merging should be an optional feature, turned on or off by the user depending on the physical setup. The reason for this being that always having sink particles merge can cause sinks to merge spuriously, creating artificially high merger counts. To balance the situation between no mergers and always merging, Ramses implements a merging timescale. In short, sinks will merge based on whether or not they have gone through one collapse timescale. This timescale depends on the physical properties of the simulation, but the concept of using this timescale was gotten from the lifetime of the first Larson core in fragmenting molecular clouds, which represents the molecular core (Larson 1969). Using this collapse timescale, mergers are restricted for young sinks (i.e. less than one collapse time). In the event a sink particle is not done collapsing it will only be merged with an old sink if they are separated by less than one accretion radius. The young sink will only be merged with another young sink if they are separated by less than two accretion radii. The merged sink particles then adopt the ID of the older sink particle in the simulation. Their masses will add together, while properties such as velocity and angular momentum will be taken as the mean value between the two. Once sink particles have merged, their accretion radii merge as well, staying at the standard 2 cells around the sink's location.

Finally, the sink particle trajectories are calculated by using both the particle mesh (PM) method developed by Hockney and Eastwood (1981) and direct summation of forces. The PM method is used for computing sink acceleration due to the gas. This is the same method they use for their star and dark matter particles in cosmological simulations. To perform these calculations, the sink particle masses are distributed onto a spherical cloud of equally spaced Ramses cells using the CIC method of Hockney and Eastwood (1981). Through CIC interpolation the gravitational accelerations of each particle are calculated. The sink acceleration is then found by averaging over all the particles that make up one sink. Direct summation is used for sink-sink interactions and sink-gas interactions. This is a simple method, where the mutual attraction between all pairwise combinations is calculated and summed. Softening is applied via a Plummer sphere to prevent sharp gradients, and the softening radius is set to half the accretion radius of the sink. It is important to note that setting the radius to such a value means it is not possible to resolve two sinks orbiting each other within a cell; however, such an event would most likely become a merger event anyways thus only affects the intermediate dynamics between starting to orbit and merging.

Chapter 3

The effects of CNM environment on filament and star formation

3.1 Introduction

Molecular clouds and star clusters lie at intermediate galactic scales (100s of pc) at which traditional studies of larger scale galactic structure and evolution give way to studies of more localized star formation processes. Actually, molecular clouds physically connect the two scales, as seen in observational studies such as *Herschel* which shows the filamentary networks connecting galactic disks down to star clusters (Alves de Oliveira et al. 2014), and PHANGS-ALMA providing evidence for links between molecular cloud properties and their galactic environments across a large array of galaxies (Thilker et al. 2021). Through fragmentation and collapse, molecular clouds host star clusters embedded in their gas. These are the parent structures of most of the stars (70-90 %) that form in GMCs (Lada and Lada 2003) and makes them a natural starting point for studies of star formation. On the large (1 kpc) scale, molecular clouds are connected to their surrounding interstellar medium via their accretion and filamentary structure, making them a key feature to determine properties in simulations of galactic disks.

Recent surveys on galactic scales have given a much better picture of the properties of entire populations of GMCs (Thilker et al. 2021; Sun et al. 2022), although they are not yet sufficient to penetrate scales below the star cluster. As mentioned above, *Herschel* has been a large driver in galactic studies of the interstellar medium, delivering the first observational evidence of filamentary structures creating hubs of star formation which act as birthplaces for young, massive star clusters. PHANGS is a recent addition to the research, but undeniably useful as it provided the largest catalogue (100,000) of individually resolved molecular clouds across multiple galaxies (Lee et al. 2022; Thilker et al. 2021; Sun et al. 2022; Turner et al. 2022; Brunetti and Wilson 2022). These observations have shown that environmental properties matter for molecular cloud properties and in what way. For instance, Sun et al. (2022) shows that molecular cloud properties depend on local environmental properties such as gas surface density and star formation density. On the galactic scale, they find it is primarily galactic shear that affects the final properties of molecular clouds.

Many of these galactic observations have connected strongly with theoretical works as well. As one example, Sun et al. (2022) compares well to the simulations of Jeffreson et al. (2020), both of whom point out that cloud properties depend on some local and some galactic environmental properties. Jeffreson et al. showed that rotation in the galactic disk influenced the geometry and rotation of the molecular clouds which formed within it. Conversely, their work finds that gravo-turbulent and star formation properties of the molecular clouds are disconnected from the overall galactic disk dynamics, supporting an agreement with Sun et al. that the gas and star formation densities are tied to local environment. Additionally, simulations from Grisdale (2021) showed that different global star formation prescriptions produce different local effects, especially along spiral arms in galactic disks, with turbulent star formation prescriptions forming stars in high density pockets located in the arms. These varying prescriptions also affected the final masses, radii and velocity dispersions of the GMCs that form, which did not see affects as strongly from galactic environment properties. Finally, observations from Soler et al. (2022) studied HI filaments towards the Galactic plane finding that the filamentary structure is closely linked to the properties of the Galactic disk, being formed as direct consequences of galactic dynamics.

On the parsec and sub-parsec scales of clusters, the work on embedded star clusters has also been rich and varied. Focusing specifically on those particular candidates for massive star formation, telescopes such as the Chandra X-Ray Observatory, Hubble and ALMA/SMA have allowed us to peer into clouds and their clusters, and investigate star formation within them (Townsley et al. 2014; Massey and Hunter 1998; Galván-Madrid et al. 2013; He et al. 2022). Observations of the embedded R136 cluster led to estimates of birth masses $\geq 250 M_{\odot}$ (Crowther et al. 2010; Brands et al. 2022), which gave evidence against the previously determined possible upper mass limit of star formation discussed in Weidner and Kroupa (2004). Additionally, Crowther et al. discuss the contribution from R136 to the ionizing flux in 30 Doradus, finding that R136a1 (the most massive of the four stars studied in this work) contributes 7% of the total ionizing flux in the entirety of 30 Doradus. These findings supported the importance of radiative feedback effects from massive stars. Han et al. (2022) perform simulations displaying the various roles that radiative feedback can play in the formation of globular star clusters. Momentum transfer from ionizing radiation supports gas in clusters against collapse, also controlling the final masses of the clusters that form. The ionizing radiation from massive stars will also contribute to the heating in the cluster, preventing low-mass stars from forming, and effectively setting the IMF (Klassen et al. 2012). On the other hand, protostellar jets and outflows from massive stars can relieve radiation pressure around the protostar and set final masses, allowing them to have a higher final mass than without outflows (Krumholz et al. 2005; Kuiper and Hosokawa 2018).

The effects of these processes on GMC formation have also been a heavily studied area. For instance, recent work has determined that the tides tearing gravitationally bound clouds apart can come, in part, from massive star-forming regions within the cloud (Ramírez-Galeano et al. 2022). Howard et al. (2018) found that the most massive clusters tend to form in the most massive GMCs that form, while others discuss that radiation

feedback plays an essential role in the lifetime of GMCs (Chevance et al. 2022). Other works have discussed the role of turbulence in GMC formation, finding it essential for filament formation (Federrath et al. 2010b), and support against gravitational collapse. Supernova explosions within clouds have been found to play a less important role in GMC destruction, as the first supernovae explosions seem to go off too late to effect their GMC, rather expanding into the local ISM (Smith et al. 2021). Some recent work, such as the STARFORGE work (Grudić et al. 2022), has combined many of these processes into one simulation starting from GMC and investigating individual stars.

In this paper, we present one part of a larger project investigating all the scales of star formation from galaxy (see Zhao et al. 2022, in prep.) to protostar. In particular, we isolate a 500^3 pc patch of the ISM from its galactic environment to investigate the scaling relations dominated by ISM processes. The CNM is the largest scale at which we can clearly resolve the transition from diffuse, atomic gas to star-forming dense gas, so we start on this scale as a means of both testing the smaller scale processes in our code before implementing them in our galactic zoom-in simulations and to isolate the effects of the ISM on cluster formation. We present the argument for bridging the two scales in the following Sec.3.2. We present our models and the previous works that guided our setup in Sec.3.3. A discussion of each important result from our models follows in Sec.3.4. Finally, we present our conclusions and the future of this problem in Sec.3.5.

3.2 Bridging scales

Computationally, a plethora of different initial conditions for any scale from the 100 kpc-scale galactic disk to the pc-scale clusters have given us ample opportunity to investigate many of the intricacies of cluster formation from different origins (see, for example, Grudić et al. 2022; Howard et al. 2018; Brown and Gnedin 2022; Rieder et al. 2022; Lane et al. 2022; Lue et al. 2021; Kim and Ostriker 2017, for simulations). Yet, even with all this work, there are lingering questions. For instance, at what point can we disconnect the galactic disk and the GMC? How much influence does the disk have on star clusters, or even individual stars? Or, given the scale of protostellar outflows and jets, how many scales does the feedback from massive stars affect? We argue here that many of these questions can not be answered in isolation from the other, but rather that they require us to bridge these two scales together. Due to this, we simulate intermediate scale of the cold, neutral medium (CNM) in order to take a closer look at the dynamics that give rise to filamentary, cluster-forming GMCs.

3.2.1 Filamentary Structures on Many Scales

André et al. (2014) presented the first all encompassing view of the role of filaments on star formation within clouds. In this view, supersonic turbulence creates the filamentary structure in the ISM (Mac Low and Klessen 2004; Larson 1981). The filaments with sufficiently high mass per unit length are gravitationally unstable and fragment into star forming cores (Molinari et al. 2010). The authors make the argument for the

strengthening link between star formation and the structure of the ISM in galactic disks, motivated by this new vision of star formation. More recent reviews, such as Chevance et al. (2022), furthers this view of star formation by exploring the filamentary environments we see surrounding GMCs from both observational and theoretical work. In either case, and among many other groups, there is general agreement that star formation is connected to filamentary structures in the (cold) ISM.

Observational studies strongly support these filamentary structures across multiple scales. In both HI and CO, systems of filaments have been visible in the ISM, with the cold phase in particular being highly filamentary (see McClure-Griffiths et al. 2006; Falgarone et al. 2001; André et al. 2010; Henning et al. 2010; Motte et al. 2010). The cold, neutral phase of the ISM, henceforth the CNM, provides a suitable initial condition for this work in a few ways. The gas in the ISM follows a cycle. Starting with the warm gas, thermal instabilities cause this to cool into the CNM and create giant, dense filaments (Hacar et al. 2022). Out of those cold filaments, molecular gas begins to form (Rathjen et al. 2021), which we can trace observationally using dust extinction due to dust growth being fastest and most abundant in cold gas (Klessen and Glover 2016). The CNM hosts most of the filamentary structures, especially those leading to and within dense molecular clouds (Seifried et al. 2017). The molecular gas forms on dust grains when gas has reached a sufficiently high column density that it can shield itself from UV radiation. In our galaxy, the density required ($\sim 10^{21} cm^{-3}$) for this shielding is also the density at which self gravity becomes important. Through gravitational collapse and instabilities discussed previously, molecular clouds create the bound clusters which host stars. Feedback from the stars heats the surrounding gas, completing the cycle and taking the gas from cold and molecular to its hot or warm phase once again (Girichidis et al. 2016). Furthermore, this filamentary structure appears well before star formation starts (André et al. 2014). These filaments, independent of the observational tracer used, appear to be coherent structures, joining with each other to form dense pockets (referred to as hubs). These hubs are associated with groups of young stellar objects, or young clusters (Myers 2009), showing a physical connection between the cold ISM and the birth environments of massive clusters.

Figure 1 of André et al. (2014) shows that filaments in which individual stars form are long, cohesive structures. These networks are also generally linear, we see no sharp changes in direction, with the bulk of the filaments aligning with the principal axis of their GMCs. In fact, while GMCs are globally filamentary, a property inherited from their local ISM environment, they also seem to host sub-filamentary systems (Arzoumanian et al. 2011). Furthermore, these characteristics can be seen across many clouds from different environments and galaxies. This universality suggests that the filamentary networks we observe come about from large-scale physical processes, such as turbulence in the ISM spanning the scales of the galactic disk and smaller. Overall, filamentary networks seem to be quite regular, with a common organizational scheme forming them. André et al. notes that filaments are split between dense areas of gas and lower density areas. Particularly, the dense filaments show more linear structure and tend to be perpendicular to magnetic field orientation (Soler 2019). On the other hand, lower density

filaments are more scattered in their directions and tend to align parallel with magnetic field orientation. This is also supported in even more recent observational work, such as Kwon et al. (2022).

We can see small-scale, bound, star-forming structures form in the hubs at filament junctions, as well as along the densest filaments from gravitational instabilities. The gravitational instabilities in a fragmenting filament come about from the transition to self-gravitation, and can best be determined through filament line masses. Taking a filament as a cylindrical piece of gas, we can examine the conditions of hydrostatic equilibrium. Using Poisson's equation, we can get the force of self-gravity as the integrated gravitational potential for a cylinder of infinite length and radius R:

$$F_g = \frac{d\Phi}{dr}\bigg|_{r=R} = 2\frac{GM_{line}}{R} \tag{3.1}$$

where $M_{line} = \int_0^R 2\pi r\rho dr$ and represents the mass per unit length of the filament, or the line mass. The pressure force balancing this self-gravity is then derived using the typical pressure-density relation $P \propto \rho^{\gamma_{eff}}$, with $\rho \propto R^{-2}$, so that it scales with radius R:

$$F_p \propto R^{1-2\gamma_{eff}} \tag{3.2}$$

Taking the ratio of these two forces can describe the hydrostatic balance:

$$\frac{F_p}{F_g} \propto R^{2(1-\gamma_{eff})} \tag{3.3}$$

where we note that γ_{eff} is the crucial scaling factor here. If $\gamma_{eff} = 1$, given a small external pressure from the surrounding gas, the filament is in hydrostatic equilibrium, perfectly balanced between gravitational collapse and internal support. This balance is true given the mass of the cylinder is equal to some critical value depending on the sound speed, for which the two forces above can be exactly equal. This we define as our critical line mass. Assuming a Plummer-like profile for the density:

$$\rho(r) = \frac{\rho_c}{\left[1 + (r/R_{flat})^2\right]^{p/2}} \tag{3.4}$$

We know the exponent of the power law for a hydrostatic cylinder is $p = 4$, and we can use this density profile in our M_{line}, defined above and take the upper bound of the integral to infinity. This defines our critical line mass as:

$$M_{crit} = \frac{2c_s^2}{G} \tag{3.5}$$

We now notice that there are two critical values in this discussion of collapse. The first, γ_{eff}, relates to the geometry of the gas, whereas the critical line mass relates to temperature via sound speed. An isothermal cylindrical cloud (or filament) collapsing radially cannot reach an equilibrium if the line mass has exceeded the critical value. In the opposite way, a filament with a line mass below the critical value can never collapse with an increase in external pressure. This is contrary to the idea of isothermal, spherical clouds which can be forced into collapsing if squeezed by its surroundings. Filaments only collapse given they have exceeded the critical line mass, determined by the local thermal properties of the gas.

When in the ISM though, we must also consider the physical affects of mixing and turbulence. It is well known that turbulent energy can support gas against collapse, which is what helps create the filamentary structures we see. In this case, we generalize the critical line mass to include all motions, thermal and non-thermal. Instead of using the sound speed of our gas, we instead consider the total velocity dispersion, which is comprised of both thermal sound speed and non-thermal motions:

$$\sigma_{tot} = \sqrt{c_s^2 + \sigma^2} \tag{3.6}$$

This gives us a virial line mass, as discussed in Fiege and Pudritz (2000), defined as:

$$M_{vir} = \frac{2\sigma_{tot}^2}{G} \tag{3.7}$$

and for magnetized filaments, we add an additional energy correction term $(1 - \mathcal{M}/\mathcal{W})$ (Fiege and Pudritz 2000), where $\mathcal{M}$ and $\mathcal{W}$ are the magnetic and gravitational energies per unit length respectively such that we have

$$M_{mag,vir} = \frac{2\sigma_{tot}^2}{G}(1 - \frac{\mathcal{M}}{\mathcal{W}}) \tag{3.8}$$

As derived, the thermal critical line mass scales with temperature such that $M_{crit} \approx 16 M_\odot pc^{-1} \times \left(\frac{T_{gas}}{10K}\right)$. This gives a general minimum critical line mass, with the value changing depending on turbulent motions within denser molecular gas. This also describes that higher temperature environments need larger filaments before they become bound and collapse. For instance, in the CNM environment, with an average temperature of 80K, we expect the average critical line mass to be $M_{crit,CNM} = 128 M_\odot pc^{-1}$, almost an order of magnitude larger than a cold molecular cloud at 10K. This suggests that larger scale structures more reminiscent of small cluster masses, can be expected to grow unstable within a piece of the CNM that is becoming gravitationally interesting, but not yet condensing into molecular gas. A very turbulent area of the CNM will take even higher line masses in order to have bound filaments. This line mass criteria is

not a constant throughout, but depends greatly on the environment, which explains the variations of structures we see throughout the ISM.

While in theoretical examples, the critical line mass gives us conditions for collapse, it is also supported observationally, making it a universally helpful criterion for structure formation in filaments. Observations of Herschel filaments suggest that supercritical filaments are in virial equipartition and gravitationally bound. The subcritical filaments, on the other hand, are unbound and have transonic or subsonic velocity dispersions (Arzoumanian et al. 2013). In fact, subcritical filaments hold less than one third of the bound prestellar cores found in a molecular cloud, and those cores tend to be less massive and less dense than their counterparts forming in dense filaments (Polychroni et al. 2013). Furthermore, the more massive bound cores found in filaments tend to be closer to intersections of filaments, supporting the idea of hub sections being the preferential site of massive cluster formation.

The hubs funnel the flow of gas, becoming dense and massive, and providing conditions for clustered star formation. These dense clumps will be the preferential sites for massive cluster formation, due to their connection to high rates of gas inflow from multiple filaments and their already dense environments (Myers 2009). Moreover, the *Herschel* Gould Belt Survey found that the deeply embedded protostars (usually those which form massive stars) are found in filaments with column densities higher than $7 \times 10^{21} cm^{-2}$ (André et al. 2014). Even without limiting our view to only massive clusters and cores, we see that the vast majority ($> 70\%$) of *Herschel*-identified prestellar cores are found within filaments as opposed to outside of filamentary structures, suggesting (as seen in Men'shchikov et al. 2010) that cores form along filaments via cloud fragmentation.

In addition to gravitational instabilities giving rise to star-forming cores, the filaments act as conduits for gas flow into smaller scales. Observational works (see Smith et al. 2012) have outlined an accretion flow along filaments onto cores, growing their mass over time. They have also suggested that a main purpose of filaments is to help focus the gas towards embedded cores (Gómez and Vázquez-Semadeni 2014). Dense cores also tend to share certain kinematic properties with their filaments, furthering the argument of gas flows along the structures. On the side of massive cluster formation, Peretto et al. have found it possible that massive protostars accrete the majority of their mass from larger (filamentary) scales as opposed to just from their prestellar core. It is thus clear that filamentary structures in the ISM connect to multiple scales, from the cloud down to the single protostar, and the expected scales of instability in the filaments are approximately four times the scale length.

3.2.2 The transition of the CNM to GMCs

Given the importance of the filamentary network in the ISM, we now must ask what exactly a GMC is. Is there a distinct difference between ISM environment and GMC? Here we argue that the difference is slight, and the transition from being in the cold ISM to being in a GMC is not a sharp one, though it is important. Chevance et al. (2022) argue that GMCs should not be thought of as discrete entities, but rather as an

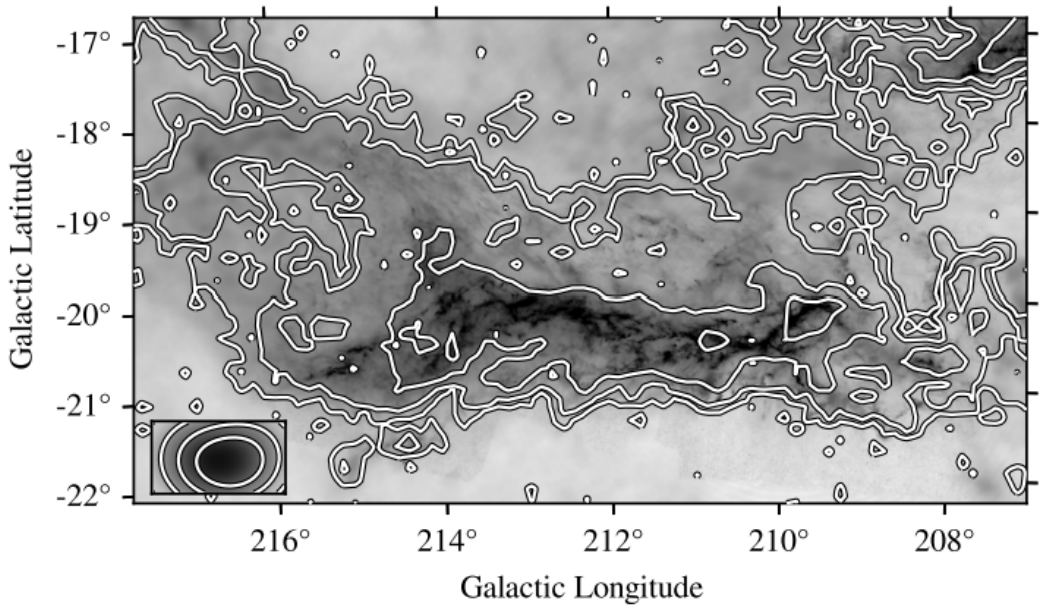

FIGURE 3.1: Image from Chevance et al. (2022). Orion A GMC dust emission map (grayscale) and $^{12}CO(1-0)$ emission (contour lines in position-position space.

observationally defined feature in gas and dust maps. Perhaps the greatest representation of this fuzzy distinction are maps of the Orion A GMC.

In Fig.3.1, Chevance et al. show the dust emission and $^{12}CO(1-0)$ emission of the Orion A cloud together. Both tracers show what we would expect of a GMC: higher aspect ratio (>1), filamentary (or clumpy, in the case of CO contours) structure and overall connection to its environment. The largest distinction is with the resolution between the two maps. While the contour lines depict a specific contour demarcating the GMC, the dust emission shows much better the connection between GMC and environment through filamentary networks. This comparison is further complicated by the fact that, while CO emission certainly guarantees that the region is in a molecular phase of gas, it is not necessarily a tracer of molecular hydrogen in GMCs (Pineda et al. 2008), making the CO emission view of a GMC an estimate of one based on resolution and limitations in the tracer itself. Thus, when looking only at gas emission, it is natural to assume a GMC as a structure which we can isolate from its environments in numerical studies.

Yet, when we look at the dust emission, we see no information about the neutral vs. molecular gas (as we would in CO). Instead, we can see a tracer of the neutral ISM, specifically of column density. Dust maps, being done with higher resolution and at sub-millimetre wavelengths where dust emission is optically thin, often let us see more small-scale structure in our GMCs, revealing the connection between ISM environment and GMC properties. Dust emission can also allow us to map out 3D structure of these clouds in a way that gas tracers cannot (Rezaei Kh. et al. 2020). Thus, dust emission

maps suggest that GMCs are inherently connected to their surrounding environment and, therefore, should not be isolated from their galactic disks to simulate their formation.

Both arguments present valid ways to consider simulations of GMCs. The connection between filamentary networks and star clusters is strong, with ample observational evidence supporting filamentary gas accretion onto hubs. Furthermore, the GMC as a structure in **molecular** hydrogen is certainly a distinct step in the transition from neutral gas to ionized, star-forming gas. As in the view of Chevance et al. (2022), we adopt the idea that a GMC should not be considered as an isolated object we can start with for star formation problems. Instead, we simply make the argument that the CNM is important for the formation and final properties of massive star clusters and vice versa, making the cold ISM the initial condition of our work.

3.3 Numerical Methods

In galactic scale simulations of cluster formation, the cold phase of the ISM gas is crucial in setting realistic cluster mass functions (CMF) on par with the Milky Way (Reina-Campos et al. 2022). Hence, without even considering other physical mechanisms, the CNM is a useful initial condition for simulations of molecular cloud formation as it is the final step before the transition to molecular gas and important for setting up cluster formation.

Ramses is a magneto-hydrodynamics code (Teyssier 2002) popularly used for cosmological simulations (for an example of star formation research, see Calura et al. 2022; Decataldo et al. 2017; Zhao et al. 2022, in prep.). On the smaller ISM scale and below, the code has become increasingly popular to use due to its capability for high resolution and efficient run times, arising from its implementation of an adaptive time step. For example Bellomi et al. (2020), Han et al. (2022), and Ntormousi and Hennebelle (2019) all use Ramses at parsec scales to investigate star formation with high resolution. Given the increasing use of the code on smaller scales, and the link this paper has to our larger galactic simulations done in Ramses, we choose to use it for our ISM scale work, as it sits between the aforementioned scales already tested. In order to achieve its high resolutions, Ramses uses adaptive mesh refinement, an important mechanism that we implement in our work in order to resolve our filamentary structure.

3.3.1 Physical Mechanisms

When investigating the CNM and molecular cloud formation, turbulence plays an important role in creating the structure. As we have already discussed, it is an essential addition to the consideration of critical line masses, influencing the gravitational collapse of filaments and thus pushing the subsequent structures that form to higher masses. Turbulent mixing from supernovae explosions specifically is most crucial in the cold and warm phases of the ISM (Kim and Ostriker 2017), where we see velocity dispersions of 5-12 kms^{-1} in simulation domains of size $0.5 \times 0.5 \times 2$ kpc. Dispersions of this magnitude are often associated with turbulence, as the typical turbulent rms velocity

is $v_{rms} \approx 5\frac{km}{s}$, which become the dominant speed compared to typical sound speeds of $c_s \approx 0.2 - 1.0\frac{km}{s}$. Large-scale turbulent motions have also been found to have significant effects on the structure of the ISM at kpc scales, with the turbulent power spectra of the filaments and molecular clouds containing signatures from an imposed larger-scale power spectrum (Colman et al. 2022).

Generally, magnetic fields are difficult to measure, especially in GMCs, due to the fact that most GMCs sit in or within only a few degrees of the Galactic mid-plane which makes line-of-sight magnetic field observations next to impossible with current technology (Pattle et al. 2022). Yet, despite this fact, we have been able to uncover a substantial amount of information regarding the effects of magnetic fields from theoretical simulations as well as our relatively limited observations. Magnetic fields link gas across multiple physical scales, being most dynamically important around the pc-scale of a molecular cloud. On scales of 10 pc, molecular clouds have highly ordered magnetic fields, with the orientation of their internal structure closely aligning with the orientation of the fields (Pillai et al. 2020; Pattle et al. 2022; Tahani et al. 2022). These highly ordered fields are indications that the field is strong enough to resist distortions due to turbulence. A strongly magnetized cloud will have anisotropic turbulence, which is necessary to create filamentary structure within them. These strong fields will provide support against compressive shocks, as well as general pressure support against collapse, thus delaying the onset of molecular cloud formation by more than 20 Myr (Girichidis et al. 2018). On the other hand, though it will take longer to form molecular clouds, fragmentation in the ISM will happen sooner with strong magnetic fields due to the action of global Parker instability modes, and support long filaments that extend in either radial or azimuthal directions in the disk, as opposed to hydro cases which see predominantly ring-like structures in the filaments (Körtgen et al. 2019).

Cluster formation will also be affected by radiation effects and galactic shear. Radiative feedback and stellar winds from massive stars will control the star formation rate through their influence on local gas properties, thus forcing clusters that form after to be lower mass, and controlling the mass distributions of clusters (Rathjen et al. 2021). Galactic shear, on the other hand, has been found to control the environment more so than clusters themselves. Specifically, galactic shear has a loose correlation with local gas properties around molecular clouds (Sun et al. 2022), while also having a moderately strong effect on the overall rotation of a cloud and, therefore, the angular momentum available to transfer from cloud to cluster (Jeffreson et al. 2020).

While we recognize the importance of both of these effects, we neglect both in this work for simplicity. In a separate study of molecular clouds in a galactic disk, as will be discussed in Zhao et al. (2022, in prep.), we include full galactic environmental effects, including galactic shear, and investigate the role of galactic shear on the clouds. In future work in that paper, we will further resolve the cluster scale and compare to the present work. Radiation effects are neglected in this work primarily due to simplicity and computational resources. In follow-up work, these effects will be added and investigated on their own.

3.3.2 Models

We mimic the cold, neutral medium (henceforth CNM), and set up both a magnetic and non-magnetic case for the purposes of comparison. We start with a 0.5kpc × 0.5kpc × 0.5kpc box, to match the size of the PHANGS-ALMA hexagonal kpc-scale observations (Sun et al. 2022) as well as being on par with similar theoretical works (cf. Bellomi et al. 2020; Colman et al. 2022). This size is chosen such that it can contain entire cloud complexes, with GMCs on the scale of 70 pc, as well as the properties and physical mechanisms acting in the local environment, such as those discussed above. However, we do note that this will not account for the gravitational potential in a galaxy due to its stars and dark matter, instead only allowing a central collapse by assuming no initial distribution in the potential. The origin is set in the center of the box, such that the z-dimension can be imagined as containing 250 pc both above and below the plane, similar to pressure scale heights of CNM gas (Körtgen et al. 2019; Soler et al. 2022). While a larger box size would be possible with a more explicit disk setup in the density profile, and simulations of collimated flows are popular for this very reason (see, for example, the SILCC projects: Girichidis et al. 2016; Girichidis et al. 2018; Rathjen et al. 2021; Seifried et al. 2017), they require additional manual setup in the initial conditions to the velocity and angular momentum. This is something we wished to avoid in our project, as we wanted to have the simplest possible physical setup and control the fewest parameters possible. Due to both the possible vertical extent of gas and the simplicity we aimed for in our initial condition, we keep the extent of our z-direction 0.5 kpc, making it symmetric with the rest of the box.

Observations of ISM filaments have shown typical widths of 0.1 pc, scaling with gas temperature (Arzoumanian et al. 2011; Pineda et al. 2011; Pineda et al. 2010). From these observations, we have produced scaling relations of filament widths and gas temperatures, as derived in André et al. (2014). Given these results, we allow our box to refine up to a highest resolution of 0.475 parsec per cell (or an effective mass resolution of $\delta m =$) in our highest resolution runs, which is achieved consistently throughout our dense filaments, such that we highly resolve our clouds and come close enough to typical filament widths to allow for accurate representation of clusters via sink particles.

The outer edges of our simulation are given outflow boundary conditions such that gas may escape but we have no inflow of new gas, and our simulation is not connected to the larger galactic disk environment. While the true, physical ISM would have a flow of gas both in and out of a region, we give only outflow boundaries because we do not include galactic shear. This allows us to pinpoint the view of the CNM, and its role in cloud and cluster formation, without adding in external angular momentum factors. We choose to study the local angular momentum that comes about from turbulent mixing and shocks moving through the medium. We find these conditions to be suitable in our experiments as a negligible amount of gas is lost (7.7%), and this loss is consistent with the dispersal of CNM gas via strong shocks. Furthermore, though periodic boundary conditions are commonly used to mimic the constant flow of gas in and out of the area, Ramses does not allow for periodic boundaries and sink particles together as errors in

Run	Density(H/cm^3)	Box Size (kpc)	Initial Temperature (K)	Δx_{start} (pc)	Δx_{end} (pc)	$\sigma_{turb,initial}$ (km/s)	$\sigma_{turb,10}$ (km/s)	B field (μG)	$\lambda_{J,thermal}$ (pc)	$\lambda_{J,kinetic}$ (pc)
disp5	30.0	(0.5,0.5,0.5)	58.8	1.95	0.48	2.72	4.99	0.0	17.44	48.23
disp8	30.0	(0.5,0.5,0.5)	58.8	1.95	0.48	6.96	8.45	0.0	17.44	123.3
disp10	30.0	(0.5,0.5,0.5)	58.8	1.95	0.48	10.5	11.5	0.0	17.44	186.2
disp5MHD	30.0	(0.5,0.5,0.5)	58.8	1.95	0.48	2.72	5.23	7.0	12.16	48.23
disp8MHD	30.0	(0.5,0.5,0.5)	58.8	1.95	0.48	6.96	8.31	7.0	12.16	123.3
disp10MHD	30.0	(0.5,0.5,0.5)	58.8	1.95	0.48	10.5	11.3	7.0	12.16	186.2
disp5LRes	30.0	(0.5,0.5,0.5)	58.8	1.95	0.97	2.72	4.99	0.0	17.44	48.23
disp8LRes	30.0	(0.5,0.5,0.5)	58.8	1.95	0.97	6.96	8.45	0.0	17.44	123.3
disp10LRes	30.0	(0.5,0.5,0.5)	58.8	1.95	0.97	10.5	11.5	0.0	17.44	186.2

Table 3.1: Parameters for all models computed. The first three models represent our fiducial models with no magnetic fields and maximum resolution of 0.48 pc. We set our magnetic field runs to have a field strength of 7 μG, in accordance with average values of ISM magnetic field strengths. The final three runs are set with lower maximum resolution (0.97 pc) in order to investigate sink particle evolution until 15 Myr. $\sigma_{turb,initial}$ and $\sigma_{turb,10}$ represent the velocity dispersion in the simulations on initialization and once 10% of the initial global crossing time has gone by, respectively. $\lambda_{J,thermal}$ and $\lambda_{J,kinetic}$ give the initial Jeans lengths of each simulation calculated using the average temperature and the velocity dispersion, respectively.

the dynamics of the sinks are much more likely in these conditions.

Table 3.1 outlines the initial conditions we use in each of our models, and we now explain some choices here. In order to mimic the magnetized CNM we initialize a constant magnetic field of magnitude $7\mu G$ in only the y direction, allowing it to evolve with the gas over time. This setup is reasonable because large scale ordered magnetic fields in galaxies are toroidal in the plane, for which a small patch will look approximately constant and oriented in one direction. The gas is initially isothermal and set at a density of 30 cm^{-3} and a temperature of roughly 58 K, comparable to median values for the CNM, as outlined in Table 1 of Klessen and Glover (2016). These values give surface densities of $320 M_{\odot} pc^{-2}$, which are not dissimilar to surface densities of $\sim 201 M_{\odot} pc^{-2}$ within the central 4.0 kpc of our Milky Way, otherwise known as the molecular zone, (Sarkar and Jog 2018). Through the chemistry code Grackle (Smith et al. 2017), we include a 9-species chemistry network, including molecular hydrogen with collisionally induced heating and cooling. We add dust chemistry for additional dust and metal line cooling throughout our box, and neglect any additional heating terms. Finally, we allow for H_2 formation on dust as well.

Since we do not include shear or any effects of galactic rotation in this box, we use a mixture of solenoidal and compressive turbulence to simulate general motions and mixing in a patch of the ISM and allow for filament formation within our box. The turbulence is initialized with a 1/3 compressive fraction. We allow our turbulence only to decay, and keep driving forces turned off such that the turbulence is never driven, as motivated by previous work such as Howard et al. (2018). Finally, the power spectrum follows a Burger's power-law shape as supported by previous studies of supersonic turbulence in the ISM and GMCs (Federrath et al. 2010b; Kitsionas et al. 2009), given by the following, where k represents the wavenumber of the spectrum, which is inversely proportional to

physical scale.

$$P(k) \propto k^{-2} \tag{3.9}$$

At any time during the simulation run time, the gas can form both clumps and sink particles. We define our clumps with a minimum density of $100 cm^{-3}$ and a minimum mass of $100 M_{\odot}$, such that they represent molecular gas clumps and GMCs (with enough mass gained over time). These are formed through the clumpfinder algorithm in Ramses, outlined in Bleuler et al. (2015). As a brief overview, this algorithm works by identifying density peaks in a data set using a peak-based approach. Peaks with significant height compared to their valleys, defined as topological relevance, are identified and labelled, while nearby peaks with lower relevance are merged into the same clump as the larger, given a certain saddle ratio between them. This algorithm allows us to identify and label larger, extended structures that cannot be accurately represented by a particle, and keep track of their properties. In our simulations, this translates well to tracking the clouds in the complex we form from our CNM, allowing for a matching between the clusters that form and which clouds they form within.

The clusters form via sink particles, initialized to take $20 M_{\odot}$ of gas from the control volume following sink criteria and are allowed to accrete more surrounding gas using a Bondi-Hoyle-Lyttleton accretion scheme (Bondi 1952; Hoyle and Lyttleton 1939). Sink particles are a useful catch-all particle that can easily represent any point-like density peak, given the appropriate sub-grid physics is applied, so we have ample freedom in our code to allow them to represent clusters. In general, the agreed upon rules for sink formation are those outlined in Federrath et al. (2010a). These rules outline conditions for density thresholds, refinement, boundedness checks, gravitational potential minima, stability, and location. Ramses adopts the same general conditions of sink particles, but simplifies the rules. Sink particles are formed from the clumps found in clumpfinder, which takes care of the density threshold formation rule, though we set our sink formation density threshold to $8000 cm^{-3}$ (higher than for our clumps), to ensure we are only picking cluster candidates out of the star-forming gas density peaks within a clump. Once sink candidates are identified, they undergo 3 checks. The first is the virial check, in which the code checks if the gas contained in the sink is gravitationally collapsing. Second, the collapse check verifies that the gradient of the velocity is negative, ensuring that not only is the gas collapsing, but it is contracting. The final check is the proximity check, which ensures that gas which is being accreted by a sink particle cannot form its own sink particle. Contrary to the outline of Federrath et al. (2010a), Ramses does not carry out separate tests for boundedness, Jeans instability or gravitational potential minima. While we refer the reader to the original methods paper for sink particles in Ramses for more detailed explanations (Bleuler and Teyssier 2014), we will point out that discarding these tests is defended by the implementation of the existing tests being more general. For example, while virial checks give valuable information on gas collapse, the authors point out it is possible for gas to exist in virial equilibrium but not be collapsing. They

then argue that their virial check approaches both collapse and boundedness by being implemented more generally.

We split our simulation runs into three groups: high resolution, high resolution with magnetic fields, and low resolution. While high resolution runs reach scales of 0.48 pc, the low resolution reach resolutions of 0.97 pc. The low resolution is chosen purely due to computational limitations to allow the simulations to run to an endpoint of 15 Myr in order to investigate sink particle properties. Within the groups of runs, we further split it into three runs with different turbulent velocity dispersions. The dispersions are set via the turbulent auto-correlation time (Federrath et al. 2010b) and the rms acceleration (Schmidt et al. 2009), defined as $f_{RMS} = 3v^2/L$. These represent the parameters through which one can set an initial turbulent velocity. The auto-correlation time sets the amount of time needed for one wave or shock to cross half the length of the box, such that it is half of the crossing time. The rms acceleration, on the other hand, sets the amplitude of the turbulence by setting the acceleration of the material. Due to their dependence on the rms velocity, the two must be set to determine the velocity within the simulation at startup. We set these to correspond to speeds approximately double the desired dispersions, found through trial and error for all other parameters of our box already set. Actual dispersions achieved at initialization ($\sigma_{turb,initial}$) and at 10% of the crossing time ($\sigma_{turb,10}$) are given in Table 3.1. In the following results we compare pertinent runs against each other, but neglect to compare all three groups against one another due to the low resolution being functionally the same as our high resolution runs with no magnetic fields.

3.4 Results

Figure 3.2 shows the column density plots in both the x and z plane for each of our hydrodynamic runs at 4.4 Myr, when cluster formation should be well underway and slowing down significantly (Li et al. 2017). While the plots of the 8 km/s and 10 km/s runs give very similar structure, the properties of the structure are different. With a dispersion of 8 km/s, the structure is sharper, due to the self-gravity of the filaments being strong enough to pull them together, yet not so strong as to dominate completely and collapse all the gas. In our 10 km/s run, the structure becomes more diffuse looking. In our 8 km/s models, the ratio of kinetic to gravitational energy is 0.01, indicating turbulent motions play a dynamic role in the formation of the structure. On the other hand, as this global ratio reaches 0.03 for our 10 km/s models, we see turbulence overcome gravity on scales of $\sim 100pc$, creating more transient structures. This higher proportion of turbulent energy to gravitational potential energy contributes too much mixing throughout the box, creating structure that cannot be pulled together by gravity as much as in the 8 km/s case. A dispersion of 5 km/s, on the other hand, displays the opposite. In this case, the gravity is far stronger than the turbulence can be, not allowing it to create nearly as much structure. The gravitational potential dominates the gas, causing a global collapse towards the centre of the box, still creating structure, though with far

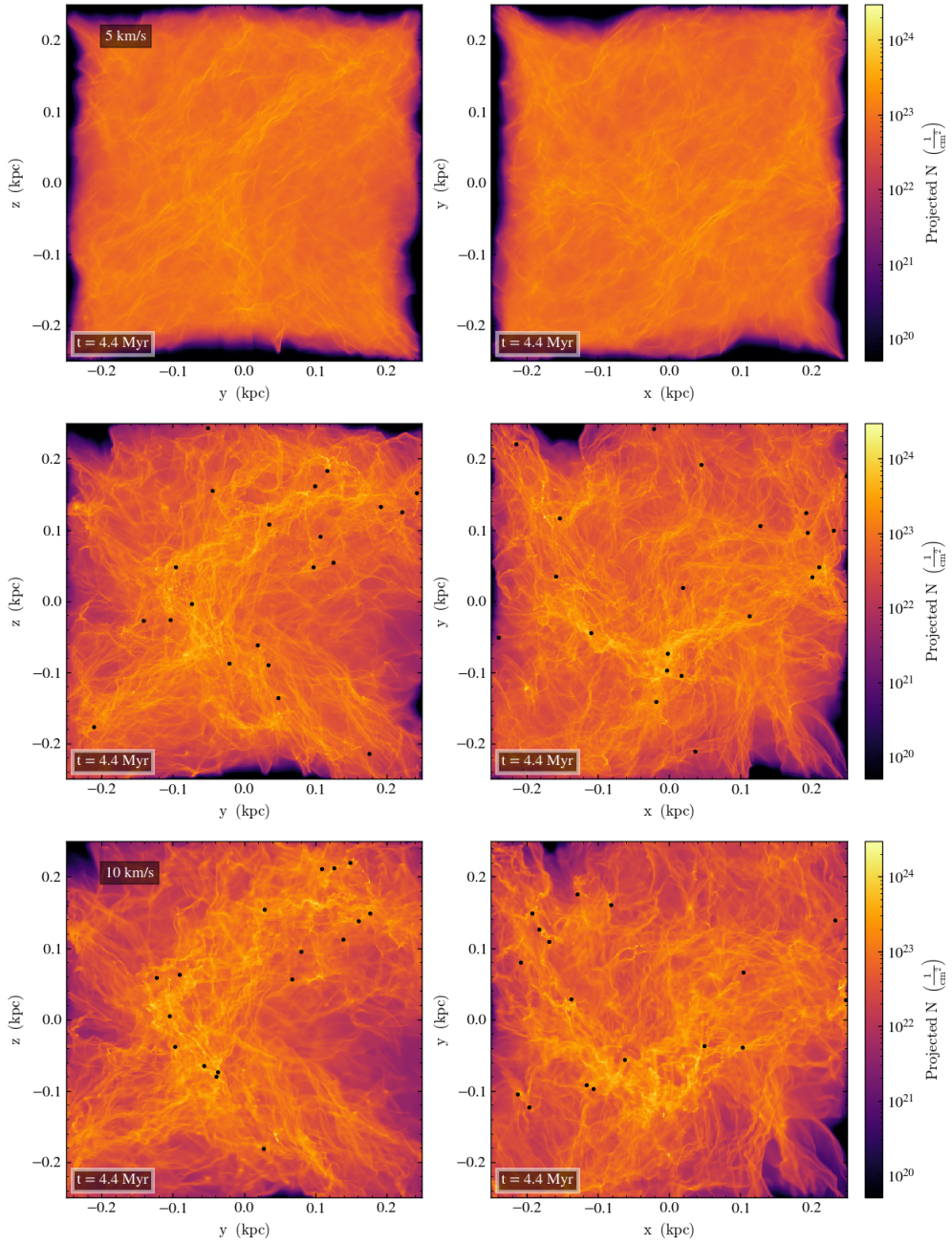

FIGURE 3.2: Column density projections of our high resolution hydrodynamical bottoms at 4.4 Myr. *Top:* Model for our 5 km/s dispersion case. Projections in both the x and z plane are shown, with the center of our box centred at (0,0). *Middle:* Same as above, but for the 8 km/s dispersion case. Black filled circles show sink particle locations at any plane depth. *Bottom:* Projections for our 10 km/s dispersion case. As before, black filled circles represent sink particle positions at any plane depth.

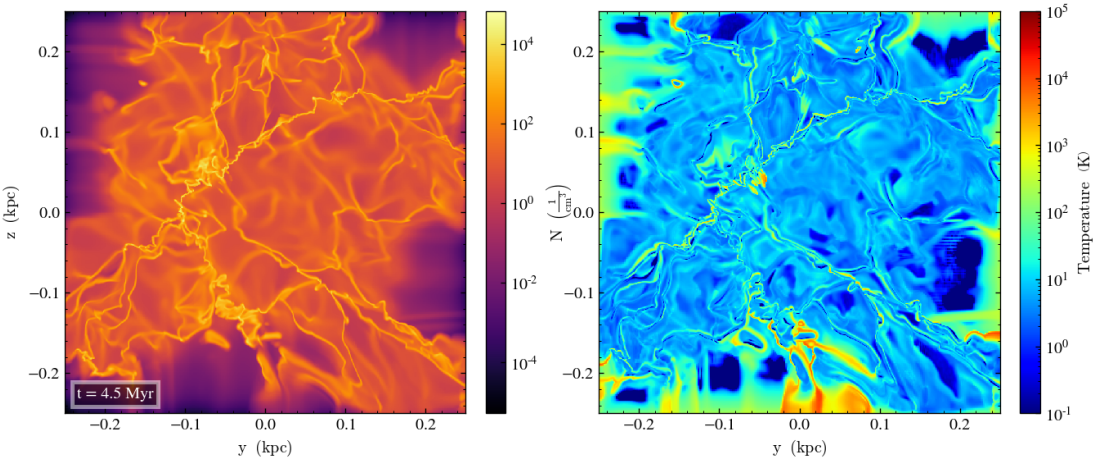

FIGURE 3.3: Slices through the center of the box of our disp8 model with density (left) and temperature (right) plotted at a time of 4.5 Myr. Sharp filamentary features are seen in the density, which is mirrored in the black contours in the temperature, tracing the highest density gas ($\sim 10^3 cm^{-3}$ and above).

shallower density fluctuations than our more turbulent setups. Based on structure alone, it is clear that a dispersion of 8 km/s can create a well balanced and realistic ISM slice.

If one compares each of these cases to Figure 3.1, it can also be seen that the 8 km/s case creates structure much more akin to observations of Orion A, specifically the structure visible in the $250\mu m$ dust emission. Figure 3.3 shows densities and temperatures in a slice of the 8 km/s model, in which we can see the densest filaments rest in temperatures $\sim 10K$. We see higher temperatures ($\leq 40K$) at the boundaries of the filaments, from shock waves creating higher temperature shock fronts. This compares well with observations of the Orion A GMC, which has temperature ranges of $\sim 10-30K$ (Lombardi et al. 2014); however, we note an abundance of very low temperature ($\sim 0.1K$) gas. This ultra-cold gas is due to a lack of additional heating present in the simulations, and point to the necessity of adding background heating to this model and, thus, the multiphase model of the ISM being crucial. Additionally, in Fig. 3.2, we notice a large structure just below the center on the 8 km/s density projections. The size and components of gas present in this structure are similar to Orion A, which is 90 pc in length and has approximately 45% of its gas sitting at high column densities (Großschedl et al. 2018). We further discuss comparisons between our models and observations of Orion A in Sec. 3.4.2.

3.4.1 When do massive clusters form?

Timescales of formation

One can also consider the timescale of cluster formation, as well as how many clusters form. In Figure 3.4, we show the time of formation for the first ten sink particles to

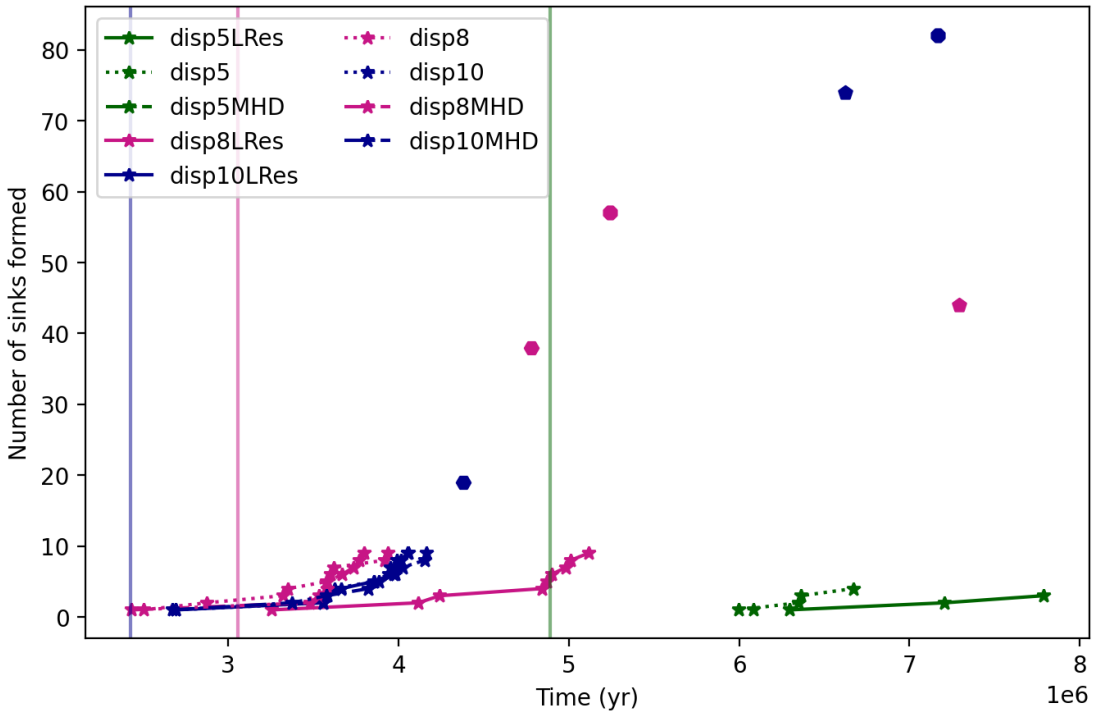

Figure 3.4: Sink formation over time for each of the three models and their three dispersions. We show the formation of the first ten sinks to form in each model, denoted by the coloured stars along the lines. Final number of sinks for the low resolution, hydro and MHD models are depicted as coloured pentagons, hexagons and octagons respectively. Coloured vertical lines show the point in time at which each group of velocity dispersions hit 10% of the initial global crossing time. This corresponds to one crossing time in a 100 pc patch, the scale of a molecular cloud.

form in each simulation, as well as the final sink particle to form, displayed via their sink number (i.e. the first sink particle to form becomes sink 1, the second sink 2, and so on). From this, we can see that sink formation tends to happen in a large burst early on in the simulation. By the 3 Myr mark, most sink formation is well underway, with the exception of our 5 km/s case shown in purple. With lower dispersion, we find overall a longer time before sink particle formation begins, indicating overall longer timescales needed to reach star-forming gas densities.

In our low resolution simulations, we see different outcomes. While the hydro and MHD runs of 8 km/s dispersions both show the earliest onset of sink formation, creating their first ten sink particles around 0.25 Myr earlier than the 10 km/s dispersion case, the lower resolution does not mimic this formation. In fact, the low resolution run of our 8 km/s case does not begin forming sink particles until after 3 Myr has passed. Additionally, there is a longer amount of time spent between the first and second sink

particle forming compared to the other 8 km/s cases, showing that the gas takes a long time to build up a clump even after reaching star-forming densities.

In our higher resolution runs, both the 8 and 10 km/s simulations show rapid sink formation before reaching 4 Myr and have similarly rapid continued sink formation. Their largest bursts in star formation both occur around 3.2 Myr and endure for a maximum 1 Myr, consistent with findings from Li et al. (2017). Additionally, between first and final sink forming, most cases show a difference of less than 4 Myr. Disregarding the 5 km/s cases, the shortest time for sink formation is 1.7 Myr, from the disp10 model. The longest time for any run to stop forming sink particles is 4.5 Myr, seen in the disp10MHD model.

The low resolution formation shows a shallower curve than the higher resolution counterparts, indicating sink formation throughout the run is slower. This difference suggests a resolution dependence on the structure and, therefore, densities we form, though the lack of evidence for this dependence from either the 5 or 10 km/s case suggests more studies to be done. In all cases, the random seed for turbulence is the same, such that the only difference should be those explicitly set in our simulations and this difference cannot be described via random differences in the velocity field of the gas. Since the only difference then is numerical, arising purely from the difference in resolution, we conclude that the results have not yet converged, and even higher resolutions are needed.

For our 5 km/s models, sink formation occurs significantly later and many fewer sink particles form. In the case of disp5MHD, we see only one sink form at 6.08 Myr, while the simulation time ends at 6.1 Myr. In the hydro case, our disp5 model forms only four sink particles in 0.5 Myr, producing an almost flat formation curve. With sink particle formation beginning so late in the run, and the formation rate being significantly slower than either the 8 or 10 km/s cases, the cloud is close to the end of its lifetime before forming any massive clusters. Additionally, though the gas is self-gravitating, the density fluctuations formed via shock waves in the medium are not strong enough to create the extra compression needed for strong filaments or massive clusters. Because of these reasons, we conclude that a velocity dispersion of 5 km/s is too low to create the structure observed in the CNM.

We conclude that high dispersions are necessary for accurate cluster formation timescales, with a dispersion of 8 km/s being ideal for both cluster formation onset and duration. We see no noticeable delay in the onset of cluster formation for the inclusion of magnetic fields, but we do see an increase in total time to complete sink formation. We go from a sink formation timescale of 2.28 Myr in the hydro model to 2.81 Myr in the MHD model. The models with dispersions of 10 km/s also produce suitable cluster formation, with similar results to the 8 km/s case. While we still see no noticeable delays in sink formation onset, we see a significant increase in the time scale of sink formation, going from 1.69 Myr in the hydro model to 4.41 Myr with the inclusion of magnetic fields. Considering the short cut off time of our 10 km/s hydro model though, we also compare to the lower resolution run, where we see the timescales go from 3.38 Myr to

4.41 Myr instead. The longer formation times are still larger than the lower dispersion cases, which one can associate with the comparatively higher turbulent energy and lower dynamic importance from the magnetic fields.

Cluster accretion

Another important factor that governs the time scale for cluster formation is the accretion rate onto the region. In Fig.3.5, the accretion rates of each individual sink particle in our disp8LRes model is plotted in multicoloured lines. We can see that when sinks first form, their accretion rates reach values up to $10^{-3} M_{\odot}/yr$, indicating good amounts of accretion in the early lifetimes of our protoclusters. However, many of the accretion rates quickly drop, lowering the overall average accretion rate as well, and many settle at $10^{-7} M_{\odot}/yr$, which is far too low to significantly grow the masses of our protoclusters. The average accretion is bolstered by the constant formation of new sink particles, whose initially high accretion rates will balance the low accretion rates of those already formed. In this way, the average accretion is roughly constant throughout the run. This is something we would expect to happen until such time as the clusters become fully formed and detach from their environment, at which point we would see average accretion drop. However, our average accretion value is also overall too low, sitting around $10^{-4} M_{\odot}/yr$. This value, while not a negligible growth, is not high enough for the rapid growth and high accretion one would expect in the formation stages of a cluster. Simulations of cluster formation show accretion rates of at least $10^{-4} M_{\odot}/yr$ and up to $10^{2} M_{\odot}/yr$ (see, for example, Reina-Campos et al. 2022; Bieri et al. 2022; Howard et al. 2018). Furthermore, the average mass of a cloud in our simulations is a few $10^{4} M_{\odot}$, comparable to the $7.5 \times 10^{4} M_{\odot}$ of Orion A, but lower than average cloud masses from galactic simulations of GMC formation (Grisdale 2021). Given that our clouds are lower mass, it is guaranteed that massive clusters would never be seen in the time frame we run our simulations for, but we would still see significant growth towards high masses.

These low accretion rates are indeed also reflected in the final masses of the sink particles, with greater than 90% of them remaining at the initial $20 M_{\odot}$ they form with and the highest mass achieved being only $21.8 M_{\odot}$. We also do not notice any mergers between sink particles to grow their mass though the early phases of a cluster's growth will be dominated by mergers. Furthermore, they will still not have negligible accretion during said time (Guszejnov et al. 2022).

A possible reason for these low accretion rates is related to the choice of accretion scheme in our simulations. In older versions of Ramses, one is given the choice of Bondi-Hoyle accretion or no accretion for sink particles, where we have chosen the former for our simulations. Though Bondi-Hoyle (BH) accretion is generally well-accepted as a simple and robust accretion scheme in large scale cosmological simulations, it is not always the most accurate physical picture. BH accretion will average over a sphere around a sink particle, with radius equal to the accretion radius, to determine the amount of mass to be accreted onto the sink. This spherical accretion ignores the filamentary nature of the structure surrounding the sink particles, making it applicable to most scenarios.

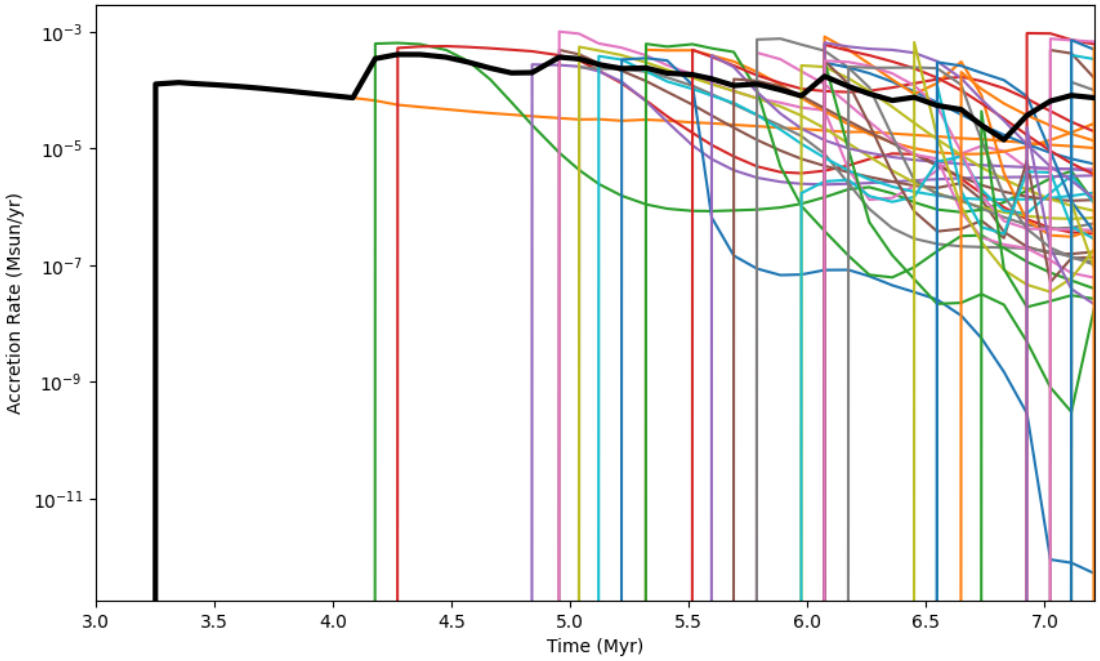

Figure 3.5: Accretion rates of sink particles for the disp8LRes model. Multicoloured lines show individual sink particles' accretion rates, with their formation corresponding to the vertical portion of the line. Thick black line shows the mean accretion rate across all sink particles over time. Limits on the x axis have been adjusted to start just before first sink forms.

Model	$M_{g,100}$	$\%_i, \%_f$	$M_{g,1000}$	$\%_i, \%_f$	$M_{g,10000}$	$\%_i, \%_f$
disp8	6.43×10^7	69, 75	2.57×10^7	28, 30	3.33×10^6	3.6, 3.9
disp8MHD	6.14×10^7	66, 72	3.02×10^7	33, 35	5.6×10^6	6.1, 6.6

Table 3.2: Masses and percentages of different gas cuts for both disp8 and disp8MHD models. From left to right: total gas mass above 100 cm^{-3} in solar masses, percentage of initial and final gas mass, same for cuts of 1000 and 10000 cm^{-3}.

While spherical accretion may be reasonable for poorly resolved structures, our results show that it is inadequate for a highly structured filamentary medium. A threshold accretion scheme, similar to that used in Flash (Fryxell et al. 2000; Federrath et al. 2010a) and the work of Howard et al. (2018), that instead considers only the filamentary feeding should give more accurate accretion rates and, therefore, higher accretion rates in the case of our models. Threshold accretion has been implemented in the most recent versions of Ramses and we will adopt it in future work but is out of the scope of this paper.

3.4.2 Molecular gas and cloud morphology

In our models we define our molecular gas at densities of 100 cm^{-3} or higher in order to best compare to dust emission maps of molecular clouds, which contain no chemical information about the molecular gas. Considering only our 8 km/s models, we can consider the percentages of gas at 100, 1000 and 10000 cm^{-3} to determine amount of molecular and star forming gas in our model. Table 3.2 shows these percentages. Comparing to just initial gas mass present in the box, 75% of the gas is converted into molecular by the 5 Myr mark, signifying a considerable amount of gas to form molecular cloud complexes. This is well supported in Figure 3.6, where we see a large amount of gas present in a cut of only molecular gas densities and higher.

We also note a large complex of molecular clouds just below the center of the box, extending roughly 100 pc in length and a maximum of 30 pc in breadth. We find this size is comparable to that of the Orion A GMC in Fig. 3.1. The similarities between the two also extend into the contours tracing molecular gas. In both figures we see the majority of the molecular cloud complex outlined by one contour, with the resolution of the contours unable to depict any of the fine filamentary structure creating the complex. Additionally, this is where we see many of the sink particles form, indicating it is the primary area of star-forming gas, again similar to the Orion A GMC complex. Overall, this shows that the interaction of turbulent ISM gas may be necessary to create the structure observed in nearby GMCs, and a consideration of the local environment around GMCs can produce more accurate structures.

We provide a zoomed in look at the molecular cloud complex noted above in Fig. 3.7. While the contours break up into smaller clumps, they still closely trace the filamentary

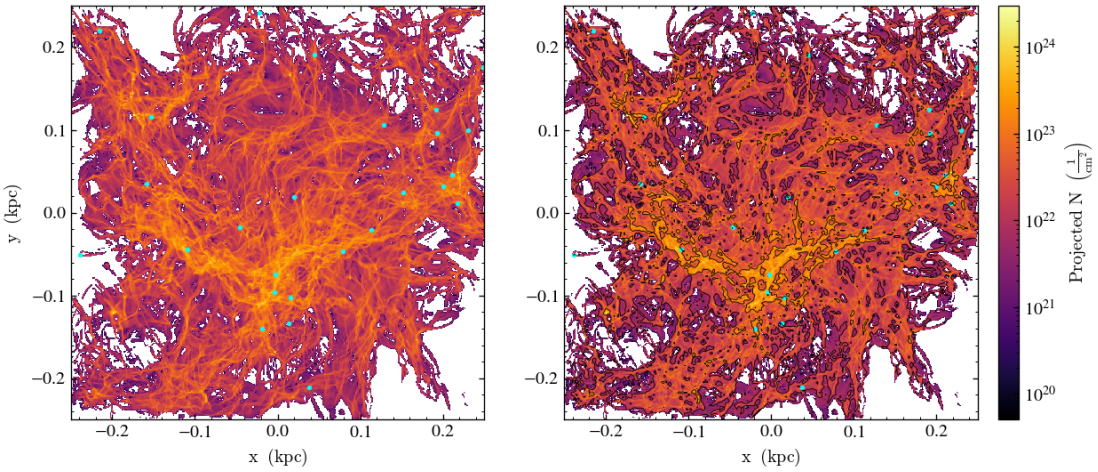

FIGURE 3.6: Side-by-side comparison of the molecular gas structure for the disp8 model. *Left:* Z-plane projection of gas, cut to contain only that above $10^{-21} g \cdot cm^{-3}$. Sink particles are represented by filled aqua circles. Maximum resolution is 0.2 pc, chosen to approach typical filament widths of 0.1 pc. *Right:* Same, with added contours to simulate observations of molecular gas structures. Contours are drawn from $10^{20} cm^{-3}$ to $10^{23} cm^{-3}$ to mimic resolution range of Lombardi et al. (2014).

structure and outline cloud sized clumps of molecular gas. For the purposes of comparison, the Orion A GMC complex is $\sim 75700 M_{\odot}$ (Lombardi et al. 2011), whereas the mass of the molecular gas contained in this cut out is $\sim 84300 M_{\odot}$. The two values are closer when considering the slightly large area contained in our cut out (150 pc x 150 pc, projected along entire z axis) compared to the size of Orion A, which is $\sim$ 90 pc (Großschedl et al. 2018). Additionally, we find we have a lower percentage of high density gas (30%, compared to 45% in Orion A according to Großschedl et al. (2018)), which can also be attributed to the outskirts of the area containing more diffuse gas. Our average velocity in the area is 16 km/s, higher than the assumed 10 km/s from Wilson et al. (1970), though not entirely outside an acceptable range. The velocity dispersion in this region is 5.36 km/s, approximately double the estimates of $\sim$ 2.5 km/s (Theissen et al. 2022). Overall, this molecular cloud candidate can be compared to observations of molecular clouds, and we find our simulations produces clouds similar to observed molecular cloud structure and properties. We hasten to add that a more detailed comparison requires a statistical sample of simulated clouds, which is beyond our computational capability in this paper.

Fig. 3.8 shows the density PDF of all of our models. While each one has slight differences, all generally follow a log-normal trend, with a power-law tail beginning to form at densities of $10^4 cm^{-3}$, similar to results from Kainulainen et al. (2014). In low density gas, our magnetic simulations tend to have the most significantly different trends. A strong peak stands out at $\sim 1 cm^{-3}$, followed by a plateau until $10^3 cm^{-3}$. This describes an overabundance of low density gas, thus indicating that our magnetic simulations

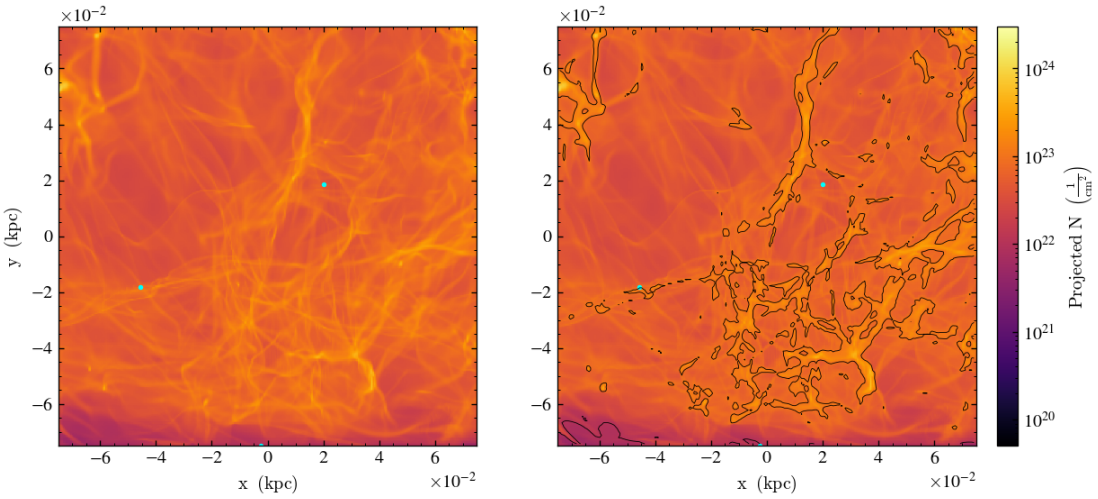

FIGURE 3.7: Zoom-in of contoured region in Fig. 3.6. Density projection and contours are the same, though plotting has been recentered on the center of the location and the domain plotted is 150 pc. Sink particles are represented by filled aqua circles.

under-produce molecular gas. However, once reaching star-forming gas densities, the abundance is higher than in our disp8 model, showing that though the magnetic runs are slower at producing molecular gas, they are very efficient at converting molecular gas to star-forming gas. We also find that our low resolution runs hold more star-forming gas than the high resolution counterparts. Of course, the resolution limit is the main factor at play in that case, where high density cells do not have an opportunity to refine and more accurately measure the density in the area. So, the overabundance is an artificial one produced by the averaging of densities in our highest density cells. Finally, we can see some change towards a power-law tail at high densities, though any that is present is slight.

3.4.3 Hydro vs. magnetic fields

To begin our analysis of the magnetic field, we first look at its effects on the structure created in different scenarios of turbulent strength. In Figures 3.9 and 3.10 we can see the directions and magnitudes of the magnetic fields in each model, respectively. The directions align as one would expect, with our densest areas containing fields mostly perpendicular to the long axis of the filamentary structure. However, we also see that the structure is highly complicated, especially so in our higher dispersions. While the 5 km/s shows long field lines that can go uninterrupted for some distance, we see considerably more loops and bends throughout the 8 and 10 km/s models. Especially when considering the projection on the x plane, the structure becomes choppy and turbulent, mimicking what we see happen in the density structures of these models. In fact, the magnetic field lines and the density structures are linked, as can be seen in the magnetic field

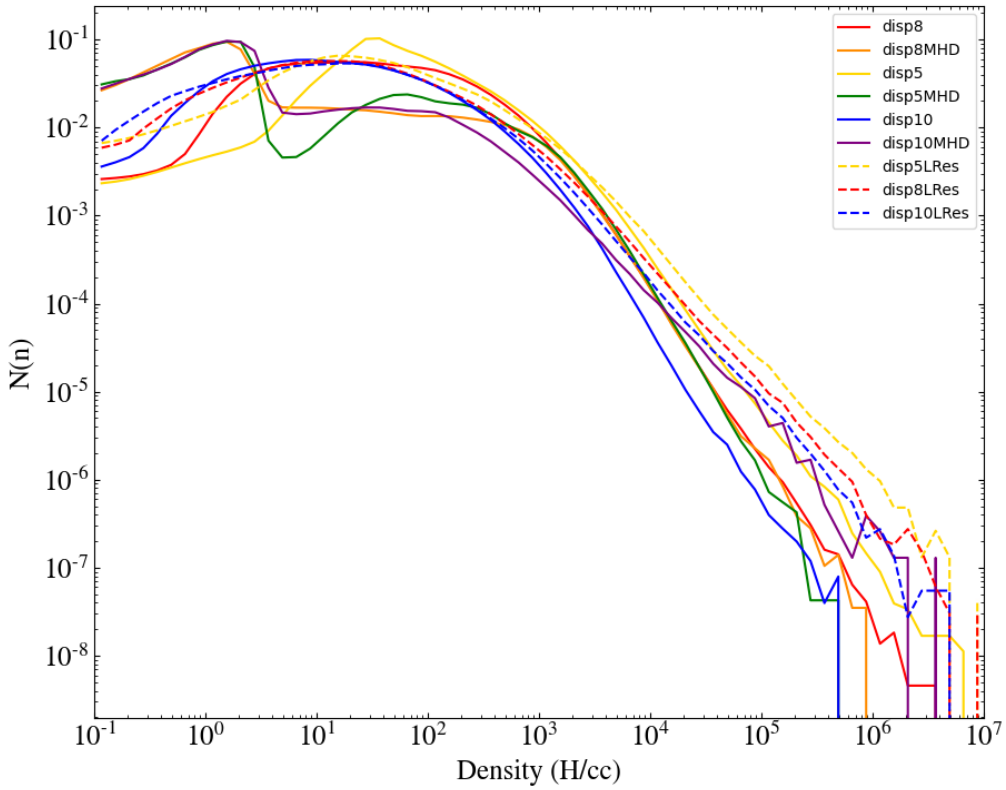

Figure 3.8: Density PDF for all 9 models at their final time. Minimum density is truncated to 0.1 cm^{-3}, maximum density is not truncated. Low resolution models are represented by dashed lines, while all 6 high resolution models are represented by solid lines.

magnitude. Through the visualization of the magnitude of the fields, we can see strong magnetic field lines carving out the filaments we see in density. In the z and y plane projections especially, we see a striated structure to the field, showcasing the field flow onto these filaments in order to create these high magnitudes in the field lines along the filaments. Finally, the majority of sink particles in the 8 km/s models form along a ridge line in the magnetic field magnitude, showing that the flow of gas along the magnetic field will funnel into high densities that will eventually become clusters and cores.

Magnetic fields can also be responsible for the delay of structure formation (Banerjee et al. 2009). In our simulations, we can see some ties between magnetic field strength, turbulent velocity dispersion and the onset of structure formation. We define the formation point of structure as the point at which structure has become "sharp", that is to say the highest resolution has been reached inside the filament. For the disp8 model, we see sharp structure forming by 2.1 Myr, becoming increasingly sharp up to the point of sink formation (see Fig. 3.11). In our magnetic models, we instead see a slight delay in forming equally sharp structure, taking 2.4 Myr. While this is a delay, it is only slight and does not seem to significantly affect when we see clusters form, as discussed in Sec. 3.4.1.

From Table 3.2, we also note that the presence of magnetic fields changes the gas composition by the end of the simulation. For gas at densities of 100 cm^{-3}, the presence of magnetic fields lowers the percentage of this gas compared to the initial(final) gas mass from 69% (75%) to 66% (72%), which is not a significant change. Though we have more of the higher density, star-forming gas. Cuts of $10^4 cm^{-3}$ show that the addition of magnetic fields almost doubles the amount of star-forming gas from 3.9% (3.6%) to 6.6% (6.1%). This shows that sufficiently strong magnetic fields can lower the total amount of molecular gas, but increase the total amount of star-forming gas. Additionally, while our disp8 model produces $770 M_\odot$ in sink particles, the disp8MHD model produces only $578 M_\odot$, yet this still leaves the magnetic case with significantly more star-forming density gas. We conclude that strong magnetic fields are thus more efficient at converting gas to star-forming densities, probably as a consequence of directing the flow of diffuse gas onto dense filaments. However, they do not create more cluster candidates, signifying they do not enhance collapse in the gas.

Finally, Fig. 3.12 plots the pressure-density profiles of the 8 km/s models as 1D line plots for total pressure and, in the bottom panel, the magnetic pressure of our disp8MHD model. Especially in molecular to star forming density ranges, we see a notable increase in pressure in our disp8MHD model when compared to our disp8 model. This increase may be due to the added magnetic pressure, which one can see in the bottom panel of the figure. However, pressure from magnetic fields at these densities sits at $\sim 10^2 K cm^{-3}$, not high enough to contribute to the change in pressure. Instead, a possible cause to this bump is due to the increased amount of star-forming density gas that has not triggered sink particle formation.

Comparing the mass-weighted pressure-density relations in Figures 3.13 & 3.14, we note the changes in slope of the relation for the highest masses. In particular, we

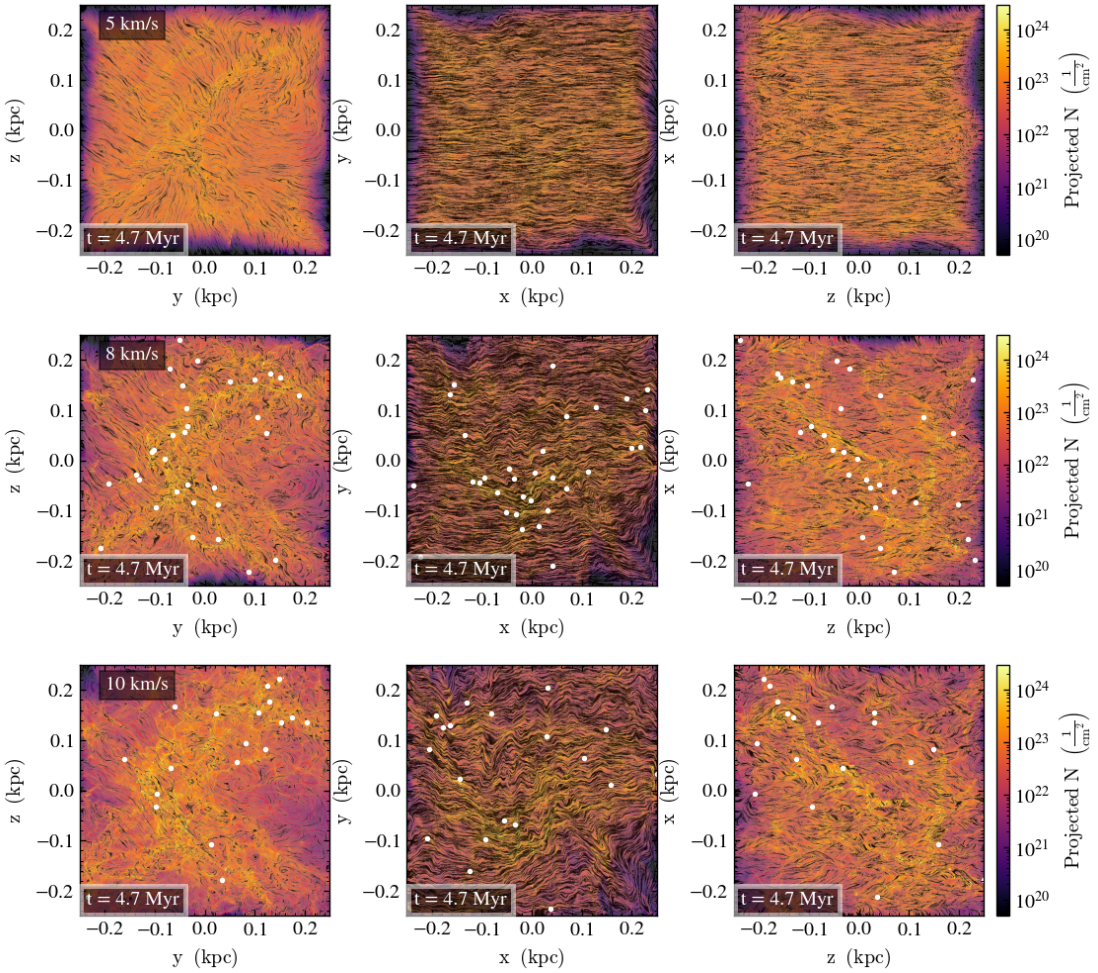

Figure 3.9: Line integral convolution of magnetic field structure overlaid on density projections for each of our MHD models. From left to right: x, z and y projections of column density. Black lines show the magnetic field lines, while sink particles are represented by filled white circles. Magnetic field is initialized as a constant in the y-direction, such that z is perpendicular to the field.

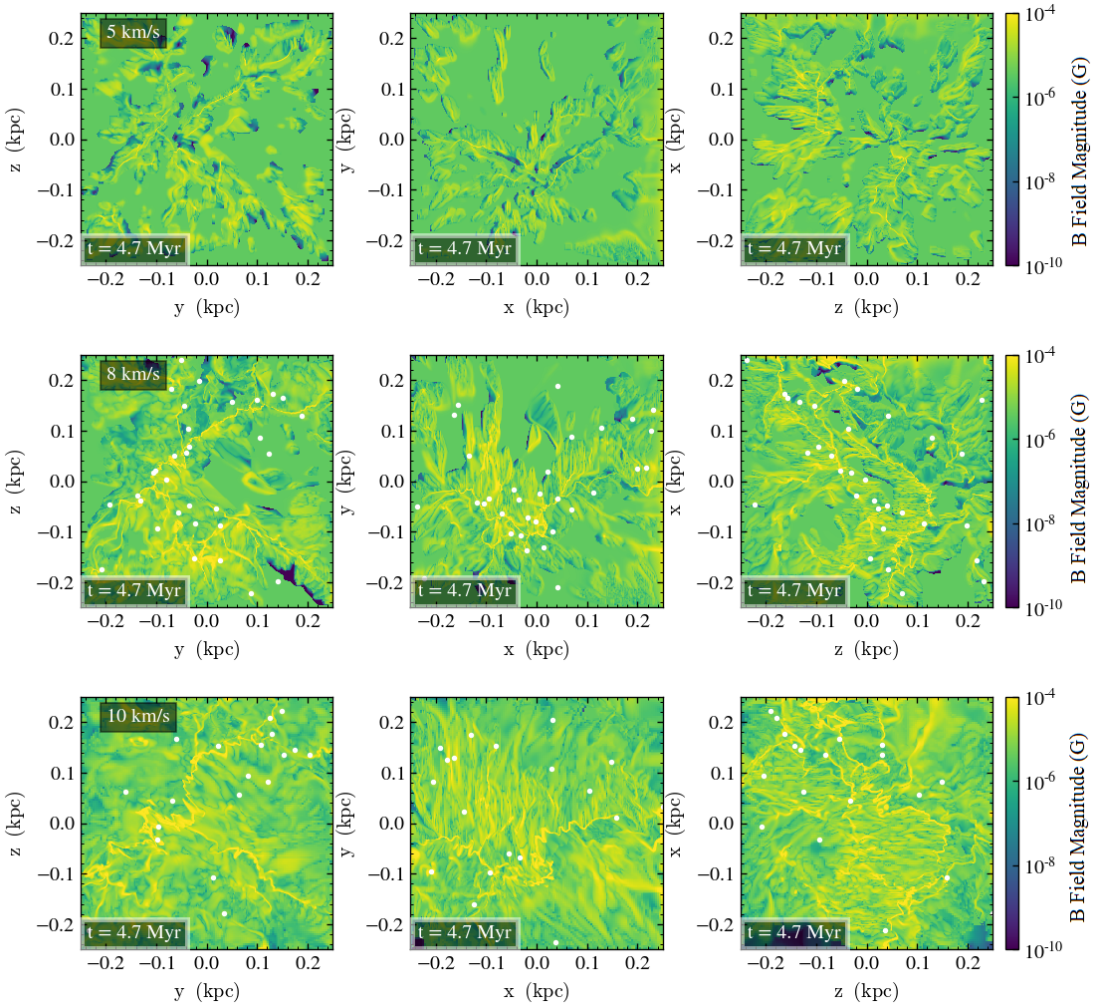

Figure 3.10: Magnetic field magnitude maps for each of our MHD models. From left to right: x, z and y plane slices through the center. Sink particles are represented by white filled circles.

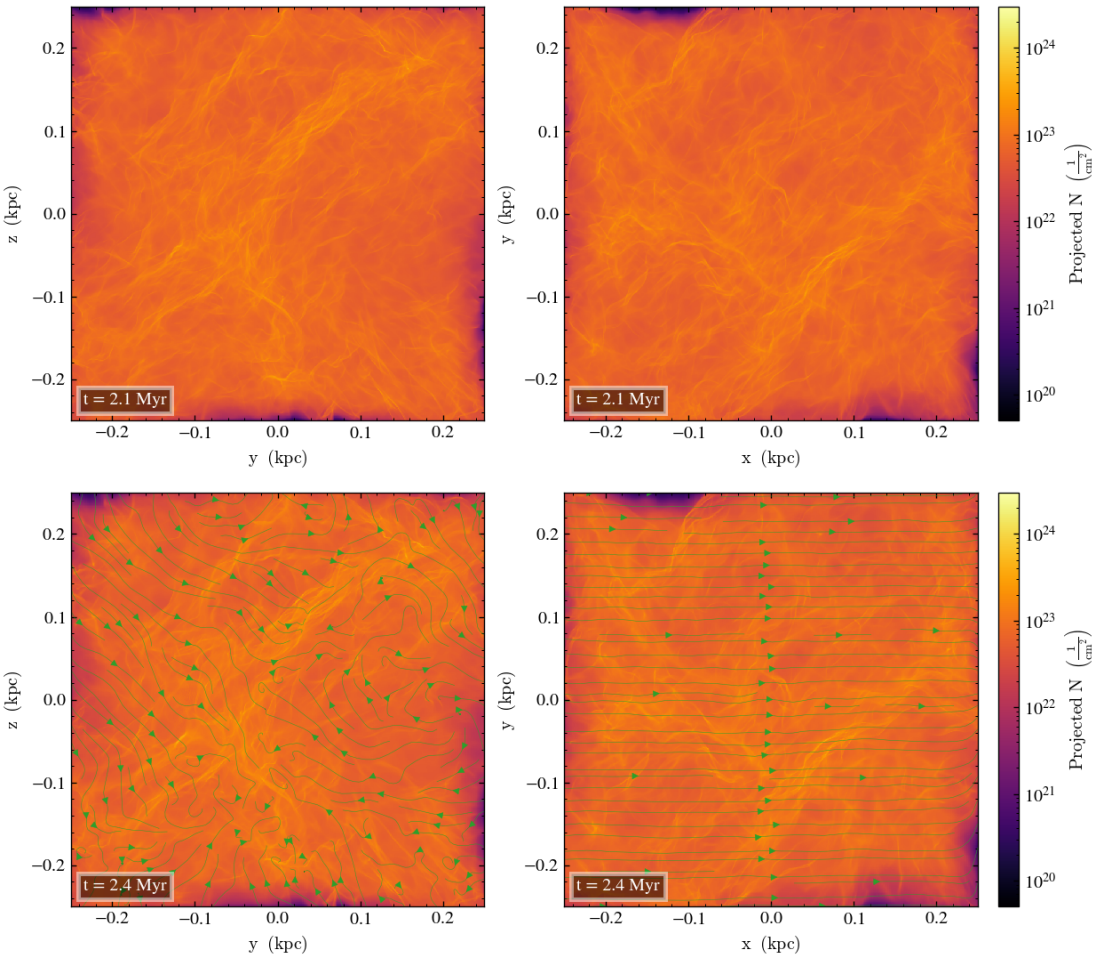

FIGURE 3.11: Density projections of the disp8 (top) and disp8MHD (bottom) models, at times with significantly sharp structure forming. Magnetic field lines are depicted by green streamlines, and both frames show simulation time in the bottom left.

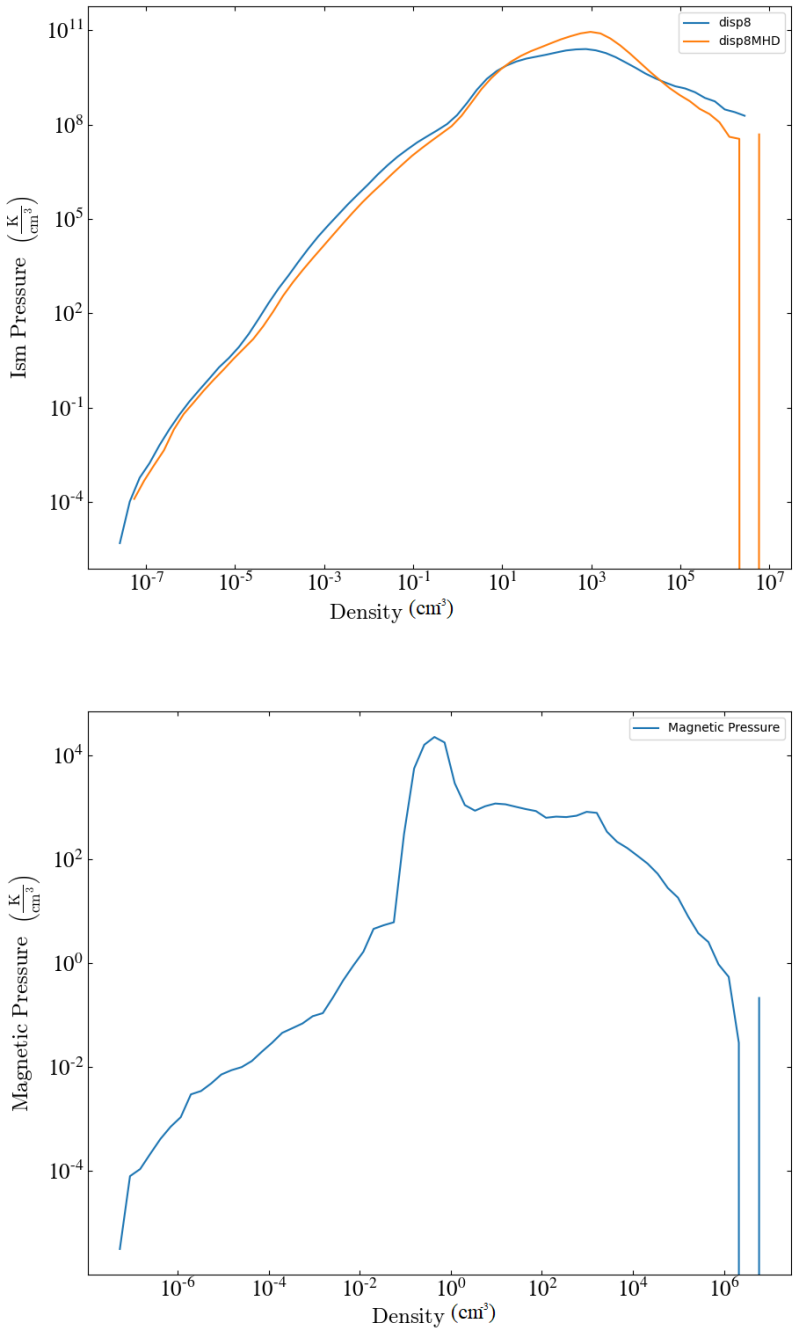

FIGURE 3.12: *Top:* Pressure-density profiles of disp8 (blue line) and disp8MHD (orange line) models. *Bottom:* pressure-density profile of only the magnetic pressure of the gas in our disp8MHD model. Note the difference in scales, with magnetic pressure making up a small amount of the total pressure (maximum $10^4 Kcm^{-3}$.

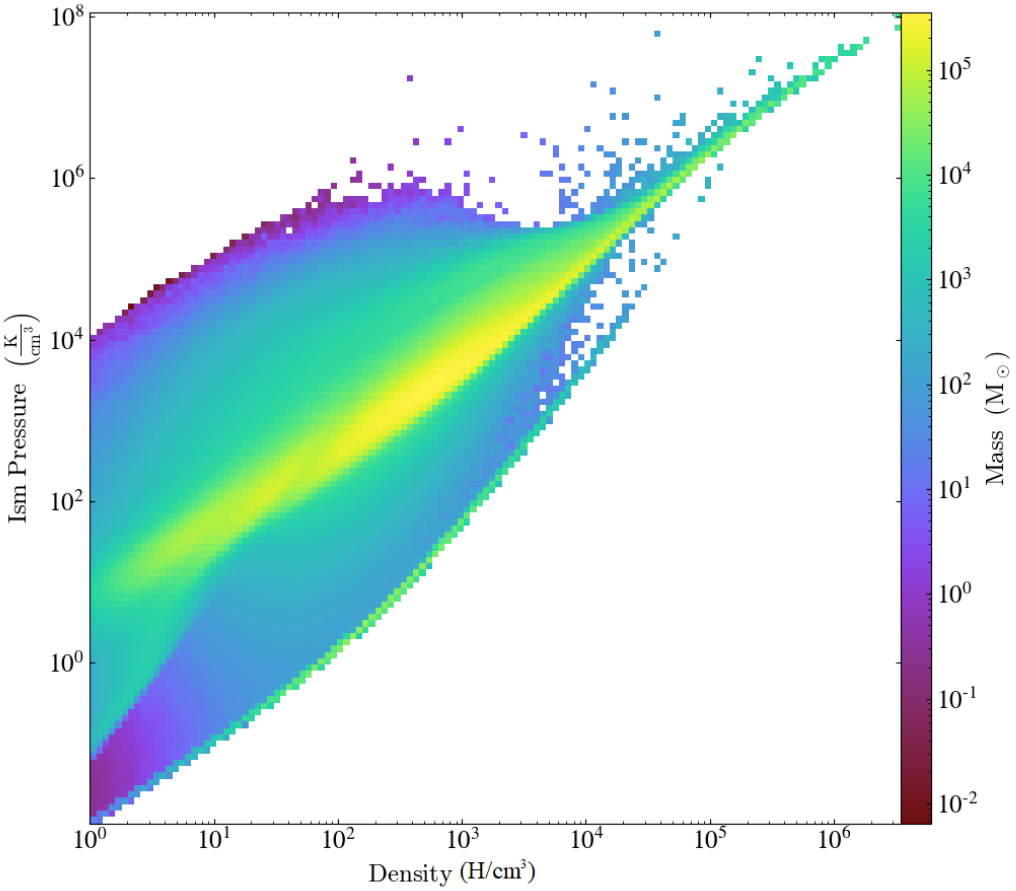

FIGURE 3.13: Mass-weighted pressure-density phase plot of the disp8 model. The majority of the mass is found in median pressure, molecular to star-forming gas.

notice the hydro case contains a majority of its mass in molecular gas at pressures of $\sim 10^3 Kcm^{-3}$, up to a maximum of $\sim 10^4 Kcm^{-3}$. In the MHD models, on the other hand, the gas sits in higher pressures by about an order of magnitude, with most sitting at pressures of $\sim 10^4 - 10^5 Kcm^{-3}$. Thus, even considering what pressure at which the majority of the gas measures, the magnetic fields contribute to overall higher pressure, a result which has also been found in previous works such as Fiege and Pudritz (2000).

3.4.4 Angular Momentum and Filament Stability

The local angular momentum distribution inside our simulations is a consequence of both the initial conditions - the power injected in solenoidal modes - as well as the subsequent interaction of oblique shocks. In Fig. 3.15, we show each individual component of angular momentum, as well as the total magnitude, as a function of radius from the center of the box. Most notably, different directions of the angular momentum are more dominant

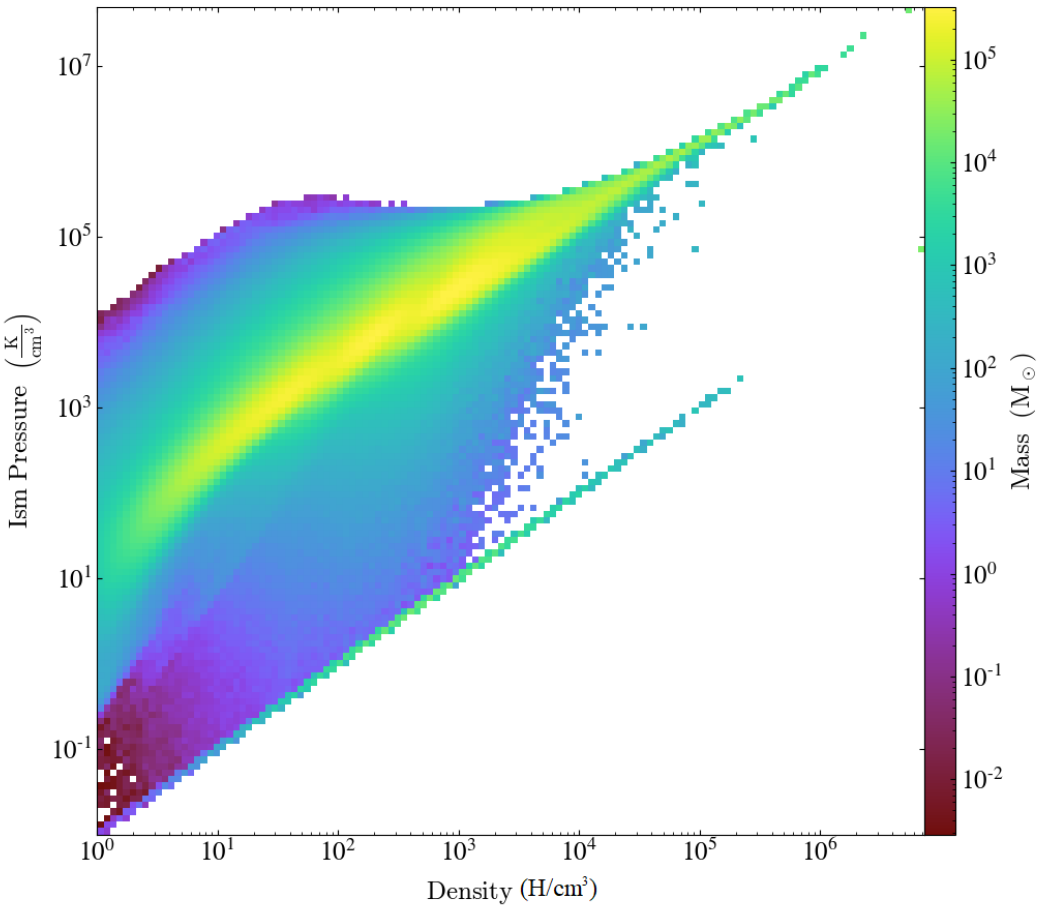

FIGURE 3.14: Same as Fig. 3.13, but for our disp8MHD model.

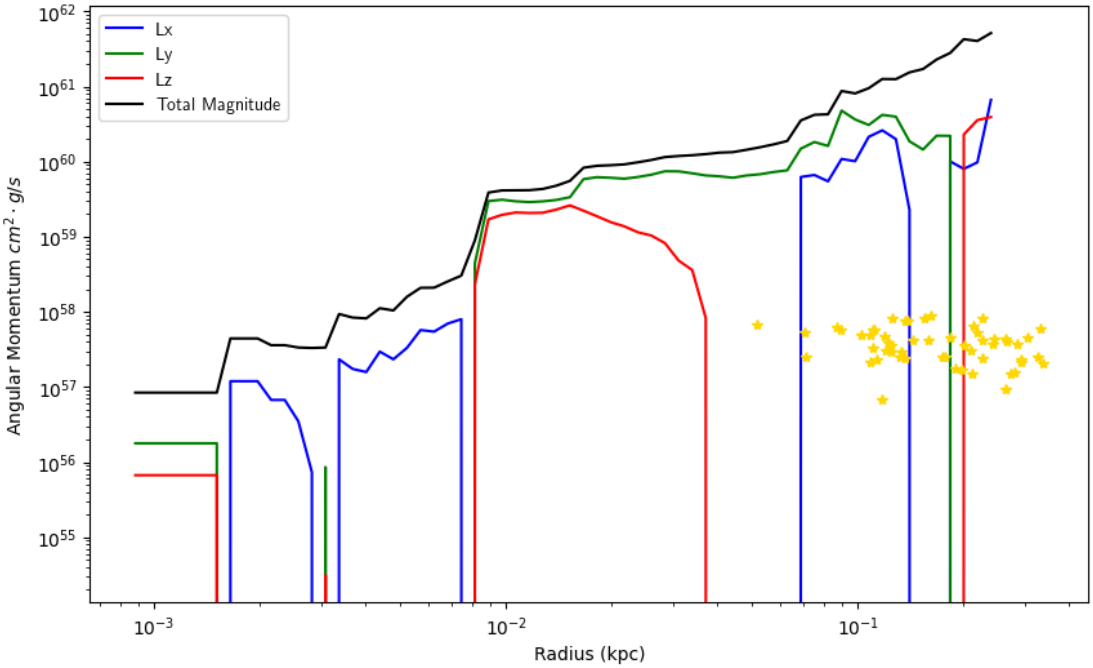

Figure 3.15: Angular momentum profile of gas throughout the box, moving radially outwards from the center, for our disp8MHD model. Both the individual components and total magnitude of the gas's angular momentum are plotted. Gold stars show the angular momentum magnitude of the sink particles and their radius from the center of the box.

in different areas. In the center of our box we see an almost even balance between the y and z component of the angular momentum, with no contribution from the x component. When our x component increases, the y and z both drop though there is an overall increase in the magnitude of the angular momentum. Though we see a switch of the dominant components throughout the box, the total angular momentum steadily increases, with the highest values on the outer edges of our box. These correspond to areas where kinetic energy is higher from turbulence and gravitational collapse stirring the gas. The positive trend outwards shows that there is no significant rotation in the box. Without adding any rotation to our initial conditions, turbulence offers no net rotation to the gas and we do not develop any at this scale, although local fluctuations due to the presence of local turbulent solenoidal modes will be present.

We also note that there seems to be no correlation between the total angular momentum at any point in the box and the angular momentum of the sink particles formed. In Fig. 3.15, we show sink particles as gold stars. Despite the different locations they form in throughout the box, the sink particles gain similar amounts of angular momentum from their formation and the gas from which they feed. We note that the total angular momentum of the sink particles seems to have no dependence on the distance they are from the center, nor on the value of the angular momentum throughout the

gas. Though they do all seem to form at radii with high angular momentum values, this can also be adequately explained by the fact none of our high-density structure is in the exact center of our box, and so the preferential points for any clusters to form are not located in the center either. The non-central locations of our structures coincide with the conclusion that we see random motion overall, and no ordered, large-scale rotation of both turbulent solenoidal modes as well as by shock interaction will be present.

Now considering the stability of the structures we create, we show the lower bound on line mass ratios by measuring each cell throughout the box in Fig. 3.16. Both the hydrodynamical and MHD models are mostly stable, with very subcritical line masses. Yet, we can see there is a difference in where and how much of the structure is supercritical between the two models. In the top panel of Fig. 3.16, we show a line mass map of a slice of our disp8 model. The background gas that is not part of the structure is very subcritical, whereas that gas making up the structure of our ISM approaches criticality. While the majority of our CNM density gas is just under critical value at 0.1, we can see our densest filaments very quickly jump to supercritical values. Especially in the densest filaments, there is a considerable number of unstable filaments, with very supercritical clumps forming in some junctions. Additionally, the filaments are surrounded by thin areas of subcritical gas, indicating a jump between filaments and more diffuse gas. This band of subcritical gas can also act as a support against external gas while the filament approaches supercritical values and fragments.

In our disp8MHD model, in the bottom panel, we see much less gas is approaching supercritical line masses, as we would expect since magnetic fields can reduce the densities generated by shocks. The more diffuse CNM gas is considerably more stable throughout the box, and we see more diffuse filaments in this map. The filaments themselves are also generally lower line masses, pushing them more subcritical. The densest, sharpest filaments can be seen to have perpendicular magnetic fields, and also correspond to line masses closer to the critical value, while those filaments with parallel fields do not approach criticality as closely. Within the filaments, we notice that only the densest filaments have any amount of supercritical gas in them. What little supercritical segments there are are also much smaller in size, while almost no clumps form at filament junctions. The magnetic fields evidently provide more support to the gas on the whole, and suppress fragmentation of the filaments. They also lower the amount of gas that does fragment when it finally reaches supercritical values. In comparison to our disp8 models, one can see that the clumps that exist are much smaller in area, and are not surrounded by lower line mass but still supercritical gas. Instead, these clumps are surrounded by gas near or below the critical point, such that when they collapse other gas around them will not follow suit immediately. Given that most of the barely subcritical gas will be roughly molecular densities, we can see the lower percentages of molecular gas in our magnetic field models. We can also see that, while the magnetic runs may be more efficient at producing star-forming gas, they do not produce clumps as quickly implying they will not have noticeably higher star formation rates early on, mirroring what we can see in Fig. 3.4.

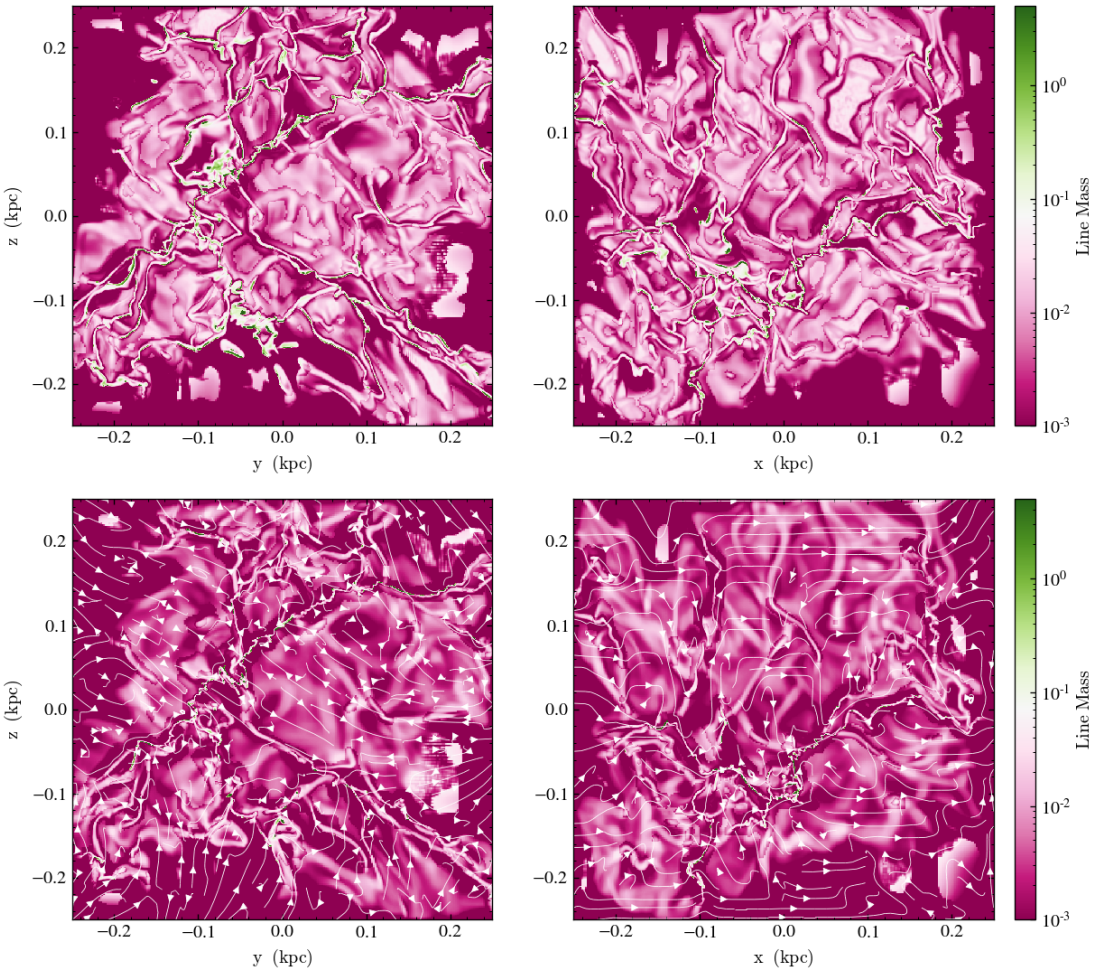

FIGURE 3.16: Line mass ratio maps for a slice of *top:* our disp8 model and *bottom:* our disp8MHD model. White streamlines in the bottom panel show the flow of the magnetic field. Slices are taken for the x and z plane, as they showcase the most structure. Critical line mass is calculated as $M_{crit} = 2c_s^2/G$. Line mass is taken as cell mass/cell width and sampled for each cell, therefore providing a lower bound.

3.4.5 Magnetic Criticality of protoclusters

Figure 3.17 shows mass to flux ratios of the first 10 sink particles to form in the disp8MHD and disp10MHD models. We calculate the flux in a radius of three cells around the sink particle from a fixed resolution buffer (actual radius of 1.8 pc), such that we contain double the accretion radius of each sink. We use the projection of the magnetic field on the normal vector of the sink particle's angular momentum. For a dispersion of 8 km/s, we can see the ratios are not constant. The majority of the sinks to form are subcritical, with ratios much less than 1, indicating most of these clusters are well supported by the magnetic field and will not collapse. One can also note that the ratios increase and decrease over time, instead of staying constant. This change in criticality of the clusters indicates that they will go through phases of support and collapse throughout their formation. For example, the first sink particles that form (represented by the purple and green lines in the top of Fig. 3.17) form to be supercritical almost instantaneously. However, these clusters also quickly drop to subcritical values, halting their contraction. On the other hand, later sinks to form are initially subcritical, with some climbing slowly to supercritical ranges.

In the higher dispersion models, we see different results. All but one sink particle remain magnetically subcritical, and that which becomes supercritical is inconsistent and drops quickly down to subcritical values again. Overall, the sink particles in the disp10MHD model show low ratios but less consistency in their values. In this model all of our sink particles are well supported by the magnetic field, having no collapse when they first form and also not trending towards supercritical value near the end of the run either. This is generally due to the clusters in the 10 km/s case staying at low mass, accreting practically nothing over their lifetime, whereas the 8 km/s case is able to grow small amounts of mass through mergers between clusters. Additionally, dispersions of 10 km/s make filaments which are more transient, spreading out the mass such that an equal area around the sink will be less dense than in the 8 km/s models. It is clear that dispersions of 8 km/s produce more stable and reliable mass to flux ratios in the areas around our clusters, as well as creating better structure overall.

Given that Bondi-Hoyle accretion is likely to highly underestimate the accretion rate onto our sinks, it is perhaps not surprising that the sink particles themselves have subcritical magnetic fields. Low accretion rates will not distort the magnetic field as much, keeping the field gradient rather low as well, thus creating subcritical fields. With higher accretion rates, more gas is pulled into the cluster and the field lines coupled to this gas are pulled in as well. This would cause a steeper magnetic field gradient, and create supercritical fields, promoting further collapse.

3.5 Conclusion

In this paper we have presented simulations of the effects of the CNM environment on molecular cloud and star cluster formation. We used MHD simulations to present three

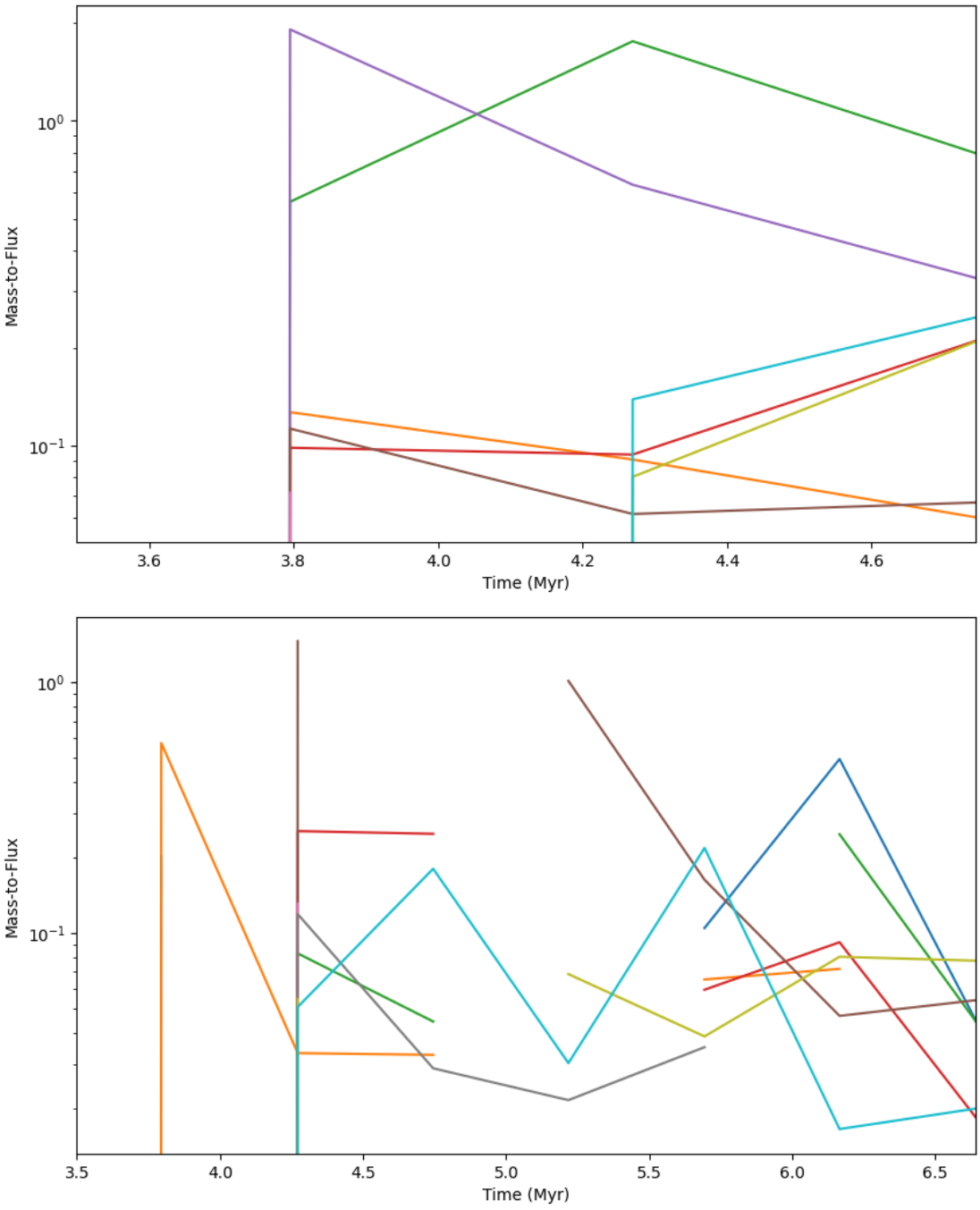

Figure 3.17: Normalized mass to flux ratio over time for the first ten sink particles to form in the disp8MHD (top) and disp10MHD (bottom) models. Mass to flux ratios are normalized against the critical ratio from Mouschovias and Spitzer (1976) which states $M/\phi_{crit} = (5/9G\pi^2)^{-1/2}$.

models of three different 3D velocity dispersions and analyzed the structure formed in the best case. We have found

- Velocity dispersion in the ISM plays a significant role in structure formation. A dispersion of 5 km/s in a 0.5 kpc cube is dominated by its self-gravity, and its weak turbulence, combined with thermal pressure, can barely support it. Dispersions of 8 and 10 km/s (initial energy ratios of 0.01 and 0.03 respectively) both allow for enough turbulence to create filamentary structure, though 8 km/s is able to reproduce features that resemble observations of the Orion A GMC and allows for high star formation rates, such that all of our sink particles form within 4 Myr, matching results from Li et al. (2017).
- The inclusion of magnetic fields in our simulations do not significantly delay the onset of sink particle formation, but do slightly increase the time spent forming sink particles. Our disp8 and disp8MHD models take 2.28 and 2.81 Myr, respectively, to finish forming 770 and 578 $M_{\odot}$, respectively.
- 75% of the total final gas mass is converted to molecular gas of densities 100 cm^{-3} or higher by the end of our simulations, and just 3.6% reaches star-forming densities of $10^4 cm^{-3}$ and higher, with $770 M_{\odot}$ in sink particles. These fractions are significantly affected by the inclusion of magnetic fields, where molecular gas fraction lowers to 72% while star-forming gas nearly doubles to 6.6%, and $578 M_{\odot}$ in sink particles, showing that sufficiently strong magnetic fields are efficient at funnelling diffuse gas to higher density filaments where clusters would form, but less likely to allow collapse to happen for cluster formation to begin.
- Magnetic field lines trace the densest filaments in both direction and magnitude, where field strengths of up to $100 \mu G$ correspond to star-forming densities of $10^4 cm^{-3}$, showing a clear link between gas density and magnetic field density. The filamentary structure of the ISM can be seen in the magnetic field strength, displaying ridges of high magnetic field along the filaments, and the structure shows perpendicular field lines funnelling these filaments to their high densities. We also see, in our 8 km/s models, the majority of cluster formation happening along the highest density filament and, thus, in highly magnetized environments.
- Magnetic fields also significantly change the pressure of the ISM, contributing magnetic pressure to increase total pressure by an order of magnitude for molecular and star-forming density gas. The inclusion of magnetic fields also changes the pressure the majority of the gas sits at by 1-2 orders of magnitude, creating an overall higher pressure environment for cluster formation to take place.
- Turbulence produces no net, global rotation throughout the box, such that rotation and shear in the ISM are likely created mostly via galactic dynamics. We see a radial increase in angular momentum as we move outwards, not indicative of rotation in the gas. We also see no noticeable correlation between local angular momentum and the angular momentum contained in our clusters.

- Filaments contain a larger percentage of supercritical gas in the absence of magnetic fields, and CNM gas overall is largely closely to critical line masses in the non-magnetic cases. Additionally, the magnetic fields suppress the amount of gas that can collapse to form clusters, such that even though fields increase efficiency of conversion to star-forming gas, they are slower to accumulate that gas into clusters.
- Mass to flux ratios of the local gas around our clusters has a dependence on velocity dispersion via the relation between dispersion and the structure we see form. Dispersions of 8 km/s can produce stable mass to flux ratios that are still capable of changing appreciably over time, allowing for clusters to go through phases of support and collapse. However, mass to flux ratios depend on accurate prescriptions of accretion.

Chapter 4

Summary & Future Work

In this chapter, we will summarize key results from the work presented in this thesis and discuss the conclusions we have made about them. We will also discuss the future work continuing on this scale and larger scales.

4.1 Key results

The work of this thesis has culminated in a number of significant results on the key processes in the CNM that lead to filament and cluster formation form kpc to pc scales.

We modelled the interstellar medium's cold, neutral phase in order to investigate structure formation within it. We found that the CNM requires a delicate balance between gravity, turbulence and cooling in order to create and maintain the filamentary structure within. While the interplay of turbulence and gravity can create filaments (see Appendix A), the two alone were found lacking in the ability to hold the structure together and maintain filaments long enough for star formation to occur. We found that cooling processes in the ISM are crucial for this maintenance of the filaments, especially dust and metal line cooling which occur primarily with the molecular gas which comprises our filaments.

Beyond this delicate balance, we have found that the structure that does form in the ISM depends on the velocity dispersion and the presence of magnetic fields. While a dispersion of 5 km/s was found inadequate to support the gas in our simulation, dispersions of 8 km/s showed differences between non-magnetic and magnetic runs, though these speeds will depend on the setup. With the inclusion of magnetic fields we found suppressed fragmentation, slower cluster formation and more efficient conversion from molecular to star-forming gas. These together illustrate that magnetic fields act to slow down star formation over time, but are very efficient at funnelling gas into filaments. We find the magnetic field structure closely traces the density throughout the box, with perpendicular field lines and high field strengths tracing the densest filaments.

The filaments themselves have largely subcritical line masses, but present visible clumping and fragmentation through supercritical pockets within filaments. However, this measurement is resolution dependent and only gives a lower bound to the critical

line mass. The percentage of supercritical gas is higher in cases with no magnetic fields, as tracks from the previous result, and the gas on the whole sits closer to critical line masses in a non-magnetized box. The mass to flux ratios of the environments around the sink show similar conclusions. The majority of sink particles start out subcritical and climb very gradually to more critical ratios in order to further collapse. Here we find yet another dependence on the velocity dispersion in the box, where a dispersion of 8 km/s allows the mass to flux ratios to remain more stable over time, and change slowly. On the other hand, dispersions of 10 km/s showcased rapid changes in mass to flux ratios and sink particles in this simulation were more likely to undergo significant changes in their mass to flux ratio over the course of the simulation.

These results all work together to describe the formation of molecular clouds and star clusters in the ISM. This scale has previously seen very little research on it, with the isothermal, spherical cloud still dominating many cloud collapse and star cluster formation works. We have presented here a reasonable and easy way to recreate molecular cloud complexes which match with observations reasonably well both in dynamics and morphology. We recreate cloud complexes similar to observations of the Orion A GMC, and produce many areas of cluster formation to study all in one simulation domain. However, the current accretion scheme in Ramses seems to be inadequate in producing accurate cluster accretion at the scale we are working, owing to the Bondi-Hoyle spherical assumptions. This aspect of the work needs to be corrected before accurate results on the cluster formation can be obtained. While further work is necessary to push this to even more realistic points, this work presents a valuable stepping stone in the goal of linking star formation across scales.

4.2 Future work on the cluster scale

In future work on this scale, we intend to add two major modifications: radiation effects and different accretion methods for the sink particles. Beginning with the latter, the goal of future work is increase sink accretion rates to appropriate cluster growth levels, at least $10^{-4} M_{\odot}/yr$. Sink particles in Ramses are given only two options for accretion. They either can have no accretion whatsoever, or use Bondi-Hoyle accretion. The BH accretion method is a spherical accretion scheme, which assumes an object (in this case, the sink particle) is accreting equally from all directions around it.

While BH accretion is a generally suitable option for accretion, it can break down in cases where the object has sharply defined structure around it. For instance, at the scale of a galaxy simulation, the individual cluster scale will not be resolved, and therefore much of the filamentary structure is also not resolved. This low resolution means that the area around a sink particle representing a cluster is already an average estimate of the density, and the filament widths are not so resolved that the cluster does not sit comfortably within the bounds of the filaments. In these cases, spherical accretion models will notice no diminution in the rates they calculate, since the particle is likely to be surrounded on all sides by roughly equal density gas. However, in cases where the

structure is highly resolved, the object is no longer surrounded by equal density gas on every side.

In our work, this is likely what we see happening. The resolution of our simulation allows us to highly resolve the filaments in the medium, such that sink particles are not accreting from a uniform medium. Instead, the accretion radius will contain low density gas from outside the filament and high density gas from the filament such that the density is no longer constant in the sphere. In a filament, the high flow rates will dominate the accretion, and very little gas from outside the filament (if any at all) is accreted onto the cluster. In the BH accretion method, there is no weighting of the material, so that denser areas are considered more in accretion rate calculations than the lower density areas. Every direction is treated equally, and thus we can see an artificially low accretion rate due to the average taken over the entire sphere.

Past work, such as Howard et al. (2018), use accretion methods other than BH accretion. For example, the flash code (Fryxell et al. 2000), uses a method referred to as threshold accretion. In this scheme, the sphere around the sink is used only to find the highest density areas and calculate the flow onto the sink particle from those high density flows. This is similar to the physical situation of filamentary feeding, and thus will not break down for highly resolved structure. This method has also been tested for the methods paper for sinks in Ramses (Bleuler and Teyssier 2014), and is the sort of accretion described by the sink particle implementation described in Federrath et al. (2010a). In our future work, we will test an implementation of this on the current sink particle algorithm in Ramses, in order to remedy the BH accretion problem.

In addition to this, we will further expand on the cluster scale by adding radiation effects to our simulations. Radiation plays a significant role in star formation, especially in the consideration of massive stars and the environments they create. From a single massive star, jets, photo-ionizing flux and heat from radiation can extend out past the cluster scale (1 pc) and affect the cloud environment. Because of this, it is important to consider radiation effects in our box before increasing the scale we investigate.

Radiation will critically affect molecular gas abundance and overall temperatures in the ISM. Many past works have investigated feedback and radiation effects on star formation. Through works such as Klassen et al. (2012), we know that the added heating from radiation can suppress low mass star formation in cluster environments, and thus suppress the overall mass of clusters. Additionally, this work found that the HII regions surrounding massive stars can rapidly change in size and shape on the order of 500 years, indicating that the role of HII regions can change very quickly, thus their effects are crucial to resolve. Furthermore, we know that while protostellar outflows will not limit mass growth and accretion on scales greater than approximately 0.1 pc (Kuiper and Hosokawa 2018), radiation and massive star winds can disrupt their natal cloud once star formation efficiencies reach 8% or higher (Grudić et al. 2022).

While many simulations include supernovae, it has been found that the first supernovae in a cloud simulation will go off at roughly 8 Myr, too late for it to have a significant

influence on the star formation (Grudić et al. 2022), though this also depends on the mass and structure of the cloud, with some clouds experiencing positive feedback effects triggering more star formation. Star formation rates are affected more by radiation and winds, especially at the cluster scale. In ISM-scale simulations, such as Rathjen et al. (2021), it has been found that the addition of radiative feedback can suppress starbursts early on in the evolution of the gas. Overall, the heating from radiation can suppress the fragmentation of the gas significantly, causing structure to take longer to form (Cunningham et al. 2011). Specifically, clouds of low surface densities are influenced by outflows and radiation earlier than their higher density counterparts, suppressing low-mass cloud formation.

On the protostellar scale (AU scales), the radiative feedback effects predominantly limit low mass star formation. For example, while Kuiper and Hosokawa (2018) find that protostellar outflows can limit protostellar mass growth, they found that very massive stars controlled their mass via their own radiation pressure and heating, not via their outflows. Furthermore, Grudić et al. (2022) found that low-mass and high-mass stars experience different growth timescales. While low-mass protostars finished their mass growth on timescales of 400 kyr, the higher mass counterparts took $\geq$ 1 Myr to finish their growth. This left massive stars as the last stars in a cluster to accrete gas before the cluster became unbound from its natal cloud.

All of these effects contribute to large changes possible in our simulations. Through the addition of radiation hydrodynamics in Ramses, we intend to add radiation effects and investigate the changes they make to our simulations. We will start with simple radiative feedback and heating, including photo-ionization from UV rays, to investigate the suppression of fragmentation and cluster formation. Carrying on from there, we will add radiative effects to our sink particles, to mimic the protostellar feedback and radiation coming from massive stars within clusters. At this stage, we will expect to see the dispersal of molecular gas, and our clusters becoming unbound. This will naturally require we run our simulations for longer times, approximately double the length we have run them for this work, and thus will be a much computationally intensive simulation to run. With these investigations carried out, we will then be prepared to continue on larger scales.

4.3 Future work on galactic scales

Throughout this thesis, we have emphasized the importance of scales in star formation problems. Indeed, while we have found a large dependence on the ISM when considering star formation, the next natural question to ask is the role of the galaxy. As a galaxy evolves, forming its spiral arms, it begins to set the initial density profile of the ISM gas that will eventually form clusters. The field has many lingering questions to answer, one of which is the effect the initial distributions can have on the final outcomes of star and star cluster formation. Furthermore, the effects of the galaxy and its dynamics have an effect on the molecular cloud (as we have seen from Grisdale 2021; Sun et al. 2022; Jeffreson et al. 2020; Soler et al. 2022), highlighting that there may be similar effects on

clusters as well. For instance, we know that feedback from massive stars can control the star formation rate, in some cases even shutting it down when strong enough (Klassen et al. 2012), but the strength needed, and when exactly it occurs, is yet unknown. Furthermore, while massive stars in a cluster may also disperse the gas of their natal GMC (Chevance et al. 2022; Ramírez-Galeano et al. 2022; Smith et al. 2021), the effect of that dispersal on nearby cluster formation is not entirely understood.

Galactic scale research on star cluster formation has seen a recent surge in work. Li et al. (2017) investigated a new mode of cluster formation in simulations of a galactic disk to recover better information on the cluster scale. They showed cluster formation happens in quick succession, with one of their simulations taking only 0.5 Myr to form all its clusters. Furthermore, the cluster formation history can be linked to bursts in star formation history, showing that especially high mass clusters preferentially form during large bursts in star formation rate (typically bursts due to major merger events), which is further supported observationally by Adamo et al. (2020). In a follow-up to their work, Li et al. (2018) extended the simulations to include supernova feedback. While cluster formation is affected by the efficiency per free-fall time especially on small scales, the intensity of the momentum feedback from supernovae affected clusters on large scales throughout the galaxy. Thus, even though local gas properties fluctuate throughout the galactic disk, it is possible to constrain certain local properties of star formation through global properties of the galaxy, bringing us ever closer to understanding massive star formation.

More recent works have also supported this idea of galaxies affecting their clusters. The E-MOSAICS suite of simulations (Pfeffer et al. 2019) has been especially active in this area. While star cluster formation is a continuous process in a galaxy, as evidenced by metallicity spreads between stars, young clusters and globular clusters shown in Pfeffer et al. (2019), there are a few conditions. Reina-Campos et al. (2019) found that cluster formation happens in specific orders. For instance, metal-poor clusters form before metal-rich ones, contributing metals to the environment through the stellar evolution they host. Additionally, the massive globular clusters will form before any others, trapping a considerable amount of the galaxy's mass in their structures. In considering the effects from galaxy formation, we also see a clearly defined epoch of globular cluster formation in the cluster formation histories of the galaxies simulated. The addition of environmental effects will suppress overall cluster formation, limiting the starting time, while globular cluster formation will naturally end when considering the feedback occurring during galaxy formation which will suppress massive structures forming further on in the disk's evolution.

Continuing with the investigation of galactic environment and cluster formation, Reina-Campos et al. (2022) found a relation between temperatures in the galactic disk and the cluster formation that occurs. By including a cold phase in their gas, they create a galaxy with a multiphase ISM. As we have discussed, these cold phases are crucial for the creation of molecular gas and the formation of molecular clouds. By including this phase in galactic simulations, the authors were able to reproduce observational results

of old star clusters in the Milky Way-type galaxies. When discussing the cluster mass function (CMF), the authors find that the presence of cold gas also adjusts the shape of the CMF. The presence of tidal shocks arising from the addition of cold gas means lower mass structures are more likely to be disrupted, thereby suppressing the low mass end of the CMF. Overall, the consideration of the CNM gas in galactic simulations can be crucial to understanding cluster formation.

Building on the experience gained from this thesis, and previous work outlined in Zhao et al. (2022, in prep.), future work will combine the current scale of this work with the galaxy to perform a zoom-in simulation from the galactic disk down to the scale of a singular star. We plan to push the resolution from our current value of 0.3 pc in the galactic simulation down to the 10-100 AU scales necessary to resolve the jets around a forming massive star system. This simulation will vastly expand on the current work of this project, as well as the works mentioned above. We will include radiative transfer to effectively simulate feedback and ionization from massive stars to accurately track the effects they have on the local environment, while also maintaining the entire galactic disk at a low resolution to account for galactic effects on the clusters and vice versa. Our plan is to continue with Ramses and push the refinement scheme to its limits to achieve the scales we want.

As this project will have enormous computational requirements, this will need to be carried out in multiple steps. As such, we continue first with our current ISM-scale simulations, as described in the previous section, to prepare appropriate hypotheses for the galactic scale and to break down the computational work into manageable chunks. The second step will work on investigating this scale in the galactic disk, comparing and contrasting the results of this thesis and the results from the inclusion of radiation effects to what we find when including galactic environmental effects. Finally, we will work on the refinement scheme to push it to even higher scales, investigating the prestellar cores in the galactic disk.

4.4 Summary

We have presented models of the cold, neutral medium and investigated how structure within it forms. Our models tested the effects of resolution, magnetic fields and velocity dispersion in the creation of filamentary networks, from which star clusters will form. We have shown that whether or not filaments capable of forming clusters depends on the velocity dispersion in the gas, specifically in the way this balances the gravitational potential energy. We have also found that the onset of this structure formation and the general speed with which it takes place can also be affected. Clusters form soon after sharp filamentary structure has appeared, and they form in rapid succession of one another. This, again, depends on velocity dispersion and magnetic field, just as the filaments they are born from. While clusters in our simulations do not accrete enough to grow significantly, we intend to continue testing this through different methods of prescribing sink particle accretion in future PhD work to investigate cluster formation further.

Overall, we have found that the formation of star forming filamentary structure in the CNM involves a surprisingly sensitive balance, with many factors playing roles in the creation of filaments. The CNM also presents a valuable starting point for star formation research, allowing for more accurate molecular clouds in their dynamics and morphology. By building structure out of the large scale ISM, one can form entire molecular cloud complexes at similar resolutions to singular molecular clouds and also be able to create strong filamentary structure, from which we know star formation takes place. This work has provided the next step in star formation simulations, showing that a limited number of assumptions need to be made about a molecular cloud at all in order to form and investigate clusters, or even single stars.

Appendix A

Supplemental work

A1 The Dispatch code

The original goal of this thesis work was mainly focused on using the recent development of Dispatch (Nordlund et al. 2018) to use zoom-in simulations to take the next step beyond the isolated cloud studies of Howard et al. (2018). From the work of my undergraduate thesis project, to the first 6 months of my Master's project, we worked to develop the state of Dispatch to handle high-resolution, multi-scale cloud collapse problems.

Dispatch (Nordlund et al. 2018) is an open source high performance hydrodynamics code framework which can be used for a variety of problems, among which was our own problem of giant molecular cloud collapse. Dispatch allows for semi-independent, task-based solutions which manifest as updates to a set of "patches" in space. It is the organization of these tasks which gives Dispatch its speed and efficiency, as well unlimited scaling. The tasks within Dispatch are organized into a hierarchy, with each one calling on the task above them in order to get the information it needs. This code structure allows for ten-fold increases to speed through a reduction of overhead bulk when completing tasks. Its hydrodynamics solver is based on the Fully Threaded Tree structure (Khokhlov 1998a) established in Ramses, giving it a well-supported and tested starting point.

Furthermore, Dispatch organizes in what order modules update during run time. It utilizes a call hierarchy, which simply organizes how the simulation will run. In essence, the call hierarchy dictates that, on startup, MPI and OpenMP must be initialized first, followed by the patches and initial task list, then allowing the code to call the job along with performance counters to track wall-clock time and general code efficiency. During the simulation, the call hierarchy dictates which objects update first and where they pass information, as well as dictating when snapshots are made. Finally, at the end of a simulation it is this call hierarchy which summarizes the performance and closes any open files. The call hierarchy, therefore, acts as a manager for all the moving parts in Dispatch, and is responsible for the bulk of the code's efficiency.

In our work with Dispatch, we collaborated with Dr. Jon Ramsey to create the first test of molecular cloud collapse in the code, the Truelove collapse (Truelove et al. 1997).

Run	Density (cm^{-3})	Crossing Time (Myr)	RMS Acceleration (cm/s^2)
d20c20	20	20	5.81×10^{-9}
d20c30	20	30	2.58×10^{-9}
d20c40	20	40	1.45×10^{-9}
d30c20	30	20	5.81×10^{-9}
d30c30	30	30	2.58×10^{-9}
d30c40	30	40	1.45×10^{-9}
d30c50	30	50	9.29×10^{-10}
d40c20	40	20	5.81×10^{-9}
d50c20	50	20	5.81×10^{-9}
d50c30	50	30	2.58×10^{-9}

TABLE A1.1: Relevant parameters set for dispersal testing in a 1 kpc^3 box on CNM gas.

In this setup, we would be able to develop the implementation of self gravity, test the turbulence setup in the code, and test the limits of resolution in Dispatch, which would give us realistic limits for our future work (the work ultimately presented in this thesis, but with a different code).

Ultimately, we could not continue with the development of this experiment, as problems in the structure of the code and limitations in the amount of people working together on it meant changes needed to get it working were unfeasible for this project. Primarily, structural issues within the hierarchy of the code created problems in the self-gravity module meaning that a collapsing cloud could not be modelled accurately. We instead switched to RAMSES to present the results of this thesis work. The switch to RAMSES was an easy one to make, as the hydrodynamics solver in Dispatch came from this, and we knew the basics of our experiment could be performed with it rather easily.

A2 The effects of box size

In preliminary runs of our simulations in RAMSES, we had initially chosen a larger box size for our simulation. As opposed to the 0.5 kpc cube, we were working with a 1 kpc cube, double the size. This setup produces an order of magnitude more mass (From $9 \times 10^7 M_\odot$ in our current setup to $9 \times 10^8 M_\odot$ in our 1 kpc box), producing a shorter freefall time, as the mass alone causes collapse to speed up.

Setting up our various parameters, namely the turbulence parameters, with this box size brought us towards testing the balance between turbulence and gravity. With no added chemistry network or cooling, we ran 10 different simulations, varying density and crossing time in the initial conditions. The conditions for each simulation is tabulated in Table A1.1.

The goal of these simulations was to find an ideal balance between self-gravity and turbulence to create the filamentary structure of the ISM that is capable of forming star

clusters. The results of this are shown in Figure A1.1, where each simulation is coordinated between either complete dispersal (i.e. strong turbulence) and complete collapse (strong gravity). From this figure, it is clear that though we could have performed more simulations, something more needed to be added. Particularly, those cases where gravity and turbulence should be close enough to balanced to create a stable, filamentary structure still had filaments that were too wide and not dense enough. In these cases, we had no cluster formation occur, and structure did not remain long enough for filaments to sharpen to the desired sub-parsec width to form clusters. Time evolution of a dispersing box is shown in A1.2. One can clearly see the lack of strong filaments throughout the evolution of the box. In comparison to our results from Chapter 3 especially, the gas in this setup never maintains its initial structure nor does it ever contract. The change from this setup to those of our results are the responsibility of additional cooling physics. Through Grackle (described in Chap 3), we can add metal line cooling and dust cooling, the latter being a crucial cooling mechanism for the ISM. From these tests, we were able to discover that the delicate interplay of gravity and pressure in the ISM relies heavily on cooling.

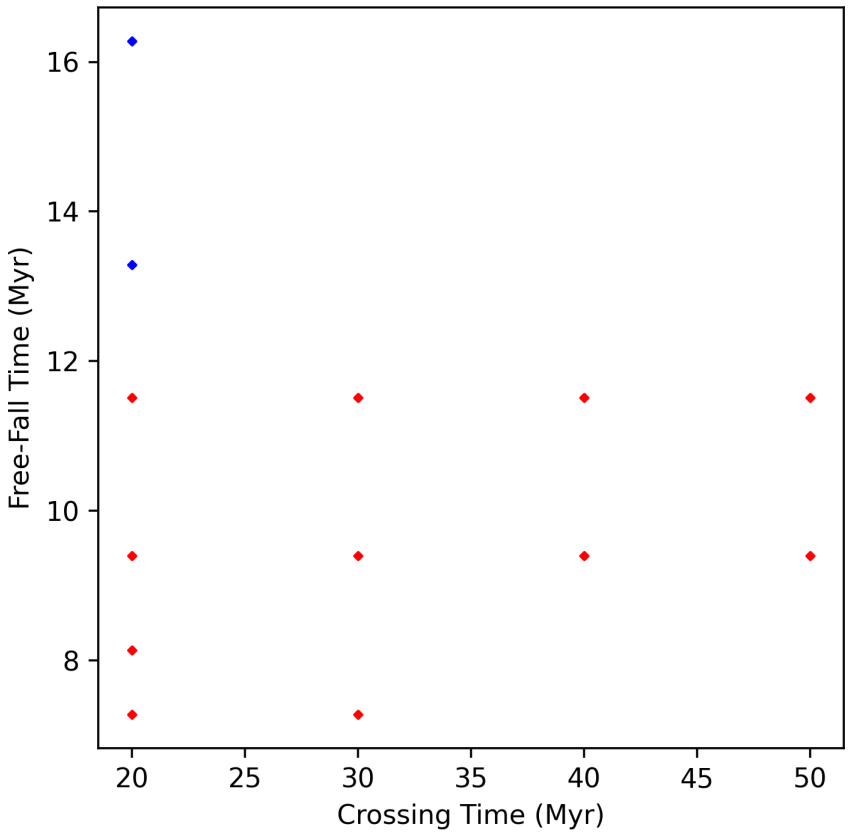

Figure A1.1: Free-fall vs. crossing time for all dispersal test models. Red diamonds indicate those which dispersed their gas quickly and out of the box, blue diamonds indicate the tests which had collapsed to the center of the box.

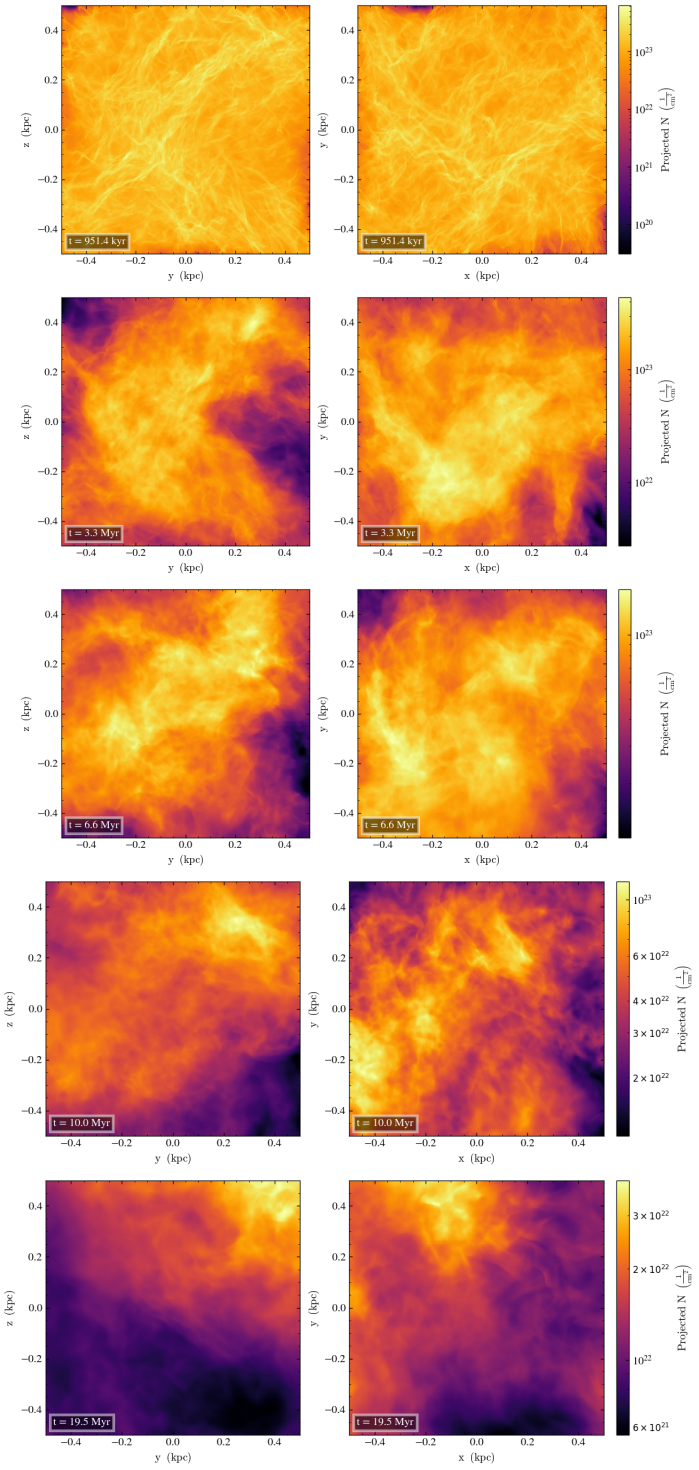

FIGURE A1.2: Time evolution of CNM gas set at a density of $50 cm^{-3}$ and a crossing time of 20 Myr. No clusters form at any point in the evolution of the structure. All high density gas flows out of the box.

Bibliography

Adamo, A., Hollyhead, K., Messa, M., Ryon, J. E., Bajaj, V., Runnholm, A., Aalto, S., Calzetti, D., Gallagher, J. S., Hayes, M. J., Kruijssen, J. M. D., König, S., Larsen, S. S., Melinder, J., Sabbi, E., Smith, L. J., and Östlin, G. (Dec. 2020). Star cluster formation in the most extreme environments: insights from the HiPEEC survey. *Monthly Notices of the Royal Astronomical Society* 499(3), 3267–3294.

Alves de Oliveira, C., Schneider, N., Merín, B., Prusti, T., Ribas, Á., Cox, N. L. J., Vavrek, R., Könyves, V., Arzoumanian, D., Puga, E., Pilbratt, G. L., Kóspál, Á., André, P., Didelon, P., Men'shchikov, A., Royer, P., Waelkens, C., Bontemps, S., Winston, E., and Spezzi, L. (Aug. 2014). Herschel view of the large-scale structure in the Chamaeleon dark clouds. *Astronomy & Astrophysics* 568 A98, A98.

André, P., Di Francesco, J., Ward-Thompson, D., Inutsuka, S. .-., Pudritz, R. E., and Pineda, J. E. (Jan. 2014). From Filamentary Networks to Dense Cores in Molecular Clouds: Toward a New Paradigm for Star Formation. In: *Protostars and Planets VI*. Ed. by H. Beuther, R. S. Klessen, C. P. Dullemond, and T. Henning, 27.

André, P., Men'shchikov, A., Bontemps, S., Könyves, V., Motte, F., Schneider, N., Didelon, P., Minier, V., Saraceno, P., Ward-Thompson, D., di Francesco, J., White, G., Molinari, S., Testi, L., Abergel, A., Griffin, M., Henning, T., Royer, P., Merín, B., Vavrek, R., Attard, M., Arzoumanian, D., Wilson, C. D., Ade, P., Aussel, H., Baluteau, J. .-., Benedettini, M., Bernard, J. .-., Blommaert, J. A. D. L., Cambrésy, L., Cox, P., di Giorgio, A., Hargrave, P., Hennemann, M., Huang, M., Kirk, J., Krause, O., Launhardt, R., Leeks, S., Le Pennec, J., Li, J. Z., Martin, P. G., Maury, A., Olofsson, G., Omont, A., Peretto, N., Pezzuto, S., Prusti, T., Roussel, H., Russeil, D., Sauvage, M., Sibthorpe, B., Sicilia-Aguilar, A., Spinoglio, L., Waelkens, C., Woodcraft, A., and Zavagno, A. (July 2010). From filamentary clouds to prestellar cores to the stellar IMF: Initial highlights from the Herschel Gould Belt Survey. *Astronomy & Astrophysics* 518 L102, L102.

Arzoumanian, D., André, P., Didelon, P., Könyves, V., Schneider, N., Men'shchikov, A., Sousbie, T., Zavagno, A., Bontemps, S., di Francesco, J., Griffin, M., Hennemann, M., Hill, T., Kirk, J., Martin, P., Minier, V., Molinari, S., Motte, F., Peretto, N., Pezzuto, S., Spinoglio, L., Ward-Thompson, D., White, G., and Wilson, C. D. (May 2011). Characterizing interstellar filaments with Herschel in IC 5146. *Astronomy & Astrophysics* 529 L6, L6.

Arzoumanian, D., André, P., Peretto, N., and Könyves, V. (May 2013). Formation and evolution of interstellar filaments. Hints from velocity dispersion measurements. *Astronomy & Astrophysics* 553 A119, A119.

Banerjee, R., Vázquez-Semadeni, E., Hennebelle, P., and Klessen, R. S. (Sept. 2009). Clump morphology and evolution in MHD simulations of molecular cloud formation. *Monthly Notices of the Royal Astronomical Society* 398(3), 1082–1092.

Banerjee, S. and Kroupa, P. (Feb. 2013). Did the Infant R136 and NGC 3603 Clusters Undergo Residual Gas Expulsion? *The Astrophysical Journal* 764(1) 29, 29.

Bellomi, E., Godard, B., Hennebelle, P., Valdivia, V., Pineau des Forêts, G., Lesaffre, P., and Pérault, M. (Nov. 2020). 3D chemical structure of diffuse turbulent ISM. I. Statistics of the HI-to-H_2 transition. *Astronomy and Astrophysics* 643 A36, A36.

Berger, M. J. and Oliger, J. (Mar. 1984). Adaptive Mesh Refinement for Hyperbolic Partial Differential Equations. *Journal of Computational Physics* 53(3), 484–512.

Bertoldi, F. and McKee, C. F. (Aug. 1992). Pressure-confined Clumps in Magnetized Molecular Clouds. *The Astrophysical Journal* 395, 140.

Bieri, R., Naab, T., Geen, S., Coles, J. P., Pakmor, R., and Walch, S. (Sept. 2022). The SATIN project I: Turbulent multi-phase ISM in Milky Way simulations with SNe feedback from stellar clusters. *arXiv e-prints* arXiv:2209.06842, arXiv:2209.06842.

Bleuler, A. and Teyssier, R. (Nov. 2014). Towards a more realistic sink particle algorithm for the ramses code. *Monthly Notices of the Royal Astronomical Society* 445(4), 4015–4036. ISSN: 0035-8711.

Bleuler, A., Teyssier, R., Carassou, S., and Martizzi, D. (June 2015). PHEW: a parallel segmentation algorithm for three-dimensional AMR datasets. Application to structure detection in self-gravitating flows. *Computational Astrophysics and Cosmology* 2 5, 5.

Bondi, H. (Jan. 1952). On spherically symmetrical accretion. *Monthly Notices of the Royal Astronomical Society* 112, 195.

Bonnor, W. B. (Jan. 1956). Boyle's Law and gravitational instability. *Monthly Notices of the Royal Astronomical Society* 116, 351.

Brands, S. A., de Koter, A., Bestenlehner, J. M., Crowther, P. A., Sundqvist, J. O., Puls, J., Caballero-Nieves, S. M., Abdul-Masih, M., Driessen, F. A., García, M., Geen, S., Gräfener, G., Hawcroft, C., Kaper, L., Keszthelyi, Z., Langer, N., Sana, H., Schneider, F. R. N., Shenar, T., and Vink, J. S. (July 2022). The R136 star cluster dissected with Hubble Space Telescope/STIS. III. The most massive stars and their clumped winds. *Astronomy and Astrophysics* 663 A36, A36.

Brown, G. and Gnedin, O. Y. (July 2022). Testing feedback from star clusters in simulations of the Milky Way formation. *Monthly Notices of the Royal Astronomical Society* 514(1), 280–301.

Brunetti, N. and Wilson, C. D. (Sept. 2022). Extreme giant molecular clouds in the luminous infrared galaxy NGC 3256. *Monthly Notices of the Royal Astronomical Society* 515(2), 2928–2950.

Calura, F., Lupi, A., Rosdahl, J., Vanzella, E., Meneghetti, M., Rosati, P., Vesperini, E., Lacchin, E., Pascale, R., and Gilli, R. (Nov. 2022). Sub-parsec resolution cosmological simulations of star-forming clumps at high redshift with feedback of individual stars. *Monthly Notices of the Royal Astronomical Society* 516(4), 5914–5934.

Cesaroni, R., Beuther, H., Ahmadi, A., Beltrán, M. T., Csengeri, T., Galván-Madrid, R., Gieser, C., Henning, T., Johnston, K. G., Klaassen, P. D., Kuiper, R., Leurini, S.,

Linz, H., Longmore, S., Lumsden, S. L., Maud, L. T., Moscadelli, L., Mottram, J. C., Palau, A., Peters, T., Pudritz, R. E., Sánchez-Monge, Á., Schilke, P., Semenov, D., Suri, S., Urquhart, J. S., Winters, J. M., Zhang, Q., and Zinnecker, H. (2019). IRAS 23385+6053: An embedded massive cluster in the making. *Astronomy & Astrophysics* 627.

Chevance, M., Krumholz, M. R., McLeod, A. F., Ostriker, E. C., Rosolowsky, E. W., and Sternberg, A. (Mar. 2022). The Life and Times of Giant Molecular Clouds. *arXiv e-prints* arXiv:2203.09570, arXiv:2203.09570.

Colella, P. and Woodward, P. R. (1984). The piecewise parabolic method (PPM) for gas-dynamical simulations. *Journal of computational physics* 54(1), 174–201.

Colman, T., Robitaille, J.-F., Hennebelle, P., Miville-Deschênes, M.-A., Brucy, N., Klessen, R. S., Glover, S. C. O., Soler, J. D., Elia, D., Traficante, A., Molinari, S., and Testi, L. (Aug. 2022). The signature of large-scale turbulence driving on the structure of the interstellar medium. *Monthly Notices of the Royal Astronomical Society* 514(3), 3670–3684.

Combes, F. (2017). AGN Feedback and Its Quenching Efficiency. *Frontiers in Astronomy and Space Sciences* 4, 10. ISSN: 2296-987X.

Commerçon, B., Hennebelle, P., Audit, E., Chabrier, G., Teyssier, R., and Henning, T. (July 2012). Combined Feedbacks of Magnetic Field and Radiative Transfer on Dense Core Collapse. In: *Advances in Computational Astrophysics: Methods, Tools, and Outcome*. Ed. by R. Capuzzo-Dolcetta, M. Limongi, and A. Tornambè. Vol. 453. Astronomical Society of the Pacific Conference Series, 13.

Crowther, P. A., Schnurr, O., Hirschi, R., Yusof, N., Parker, R. J., Goodwind, S. P., and Abu Kassim, H. (2010). The R136 star cluster hosts several stars whose inidividual masses greatly exceed the accepted 150 $M_\odot$ stellar mass limit. *Monthly Notice of the Royal Astronomical Society* 408, 731–751.

Crutcher, R. M. and Kemball, A. J. (Oct. 2019). Review of Zeeman Effect Observations of Regions of Star Formation K Zeeman Effect, Magnetic Fields, Star formation, Masers, Molecular clouds. *Frontiers in Astronomy and Space Sciences* 6 66, 66.

Cunningham, A. J., Klein, R. I., Krumholz, M. R., and McKee, C. F. (Oct. 2011). Radiation-hydrodynamic Simulations of Massive Star Formation with Protostellar Outflows. *The Astrophysical Journal* 740(2) 107, 107.

Cunningham, A. J., McKee, C. F., Klein, R. I., Krumholz, M. R., and Teyssier, R. (Jan. 2012). Radiatively Efficient Magnetized Bondi Accretion. *The Astrophysical Journal* 744(2) 185, 185.

Decataldo, D., Ferrara, A., Pallottini, A., Gallerani, S., and Vallini, L. (Nov. 2017). Molecular clumps photoevaporation in ionized regions. *Monthly Notices of the Royal Astronomical Society* 471(4), 4476–4487.

Draine, B. T. (2011). *Physics of the Interstellar and Intergalactic Medium*.

Falgarone, E., Pety, J., and Phillips, T. G. (July 2001). Filamentary Structure and Helical Magnetic Fields in the Environment of a Starless Dense Core. *The Astrophysical Journal* 555(1), 178–190.

Federrath, C., Banerjee, R., Clark, P. C., and Klessen, R. S. (2010a). Modeling collapse and accretion in turbulent gas clouds: implementation and comparison of sink particles in AMR and SPH. *The Astrophysical Journal* 713, 269–290.

Federrath, C., Roman-Duval, J., Klessen, R. S., Schmidt, W., and Mac Low, M. M. (2010b). Comparing the statistics of interstellar turbulence in simulations and observations: Solenoidal versus compressive turbulence forcing. *Astronomy & Astrophysics* 512.

Fiege, J. D. and Pudritz, R. E. (Jan. 2000). Helical fields and filamentary molecular clouds - I. *Monthly Notices of the Royal Astronomical Society* 311(1), 85–104.

Fromang, S., Hennebelle, P., and Teyssier, R. (Oct. 2006). A high order Godunov scheme with constrained transport and adaptive mesh refinement for astrophysical magnetohydrodynamics. *Astronomy and Astrophysics* 457(2), 371–384.

Fryxell, B., Olson, K., Ricker, P., Timmes, F. X., Zingale, M., Lamb, D. Q., and MacNeice, P. (2000). Flash: An adaptive mesh hydrodynamics code for modeling astrophysical thermonuclear flashes. *Astrophysical Journal Sumpplement Series* 131, 273–334.

Galván-Madrid, R., Liu, H. B., Zhang, Z. .-., Pineda, J. E., Peng, T. .-., Zhang, Q., Keto, E. R., Ho, P. T. P., Rodríguez, L. F., Zapata, L., Peters, T., and De Pree, C. G. (Dec. 2013). MUSCLE W49: A Multi-Scale Continuum and Line Exploration of the Most Luminous Star Formation Region in the Milky Way. I. Data and the Mass Structure of the Giant Molecular Cloud. *The Astrophysical Journal* 779(2) 121, 121.

Girichidis, P., Seifried, D., Naab, T., Peters, T., Walch, S., Wünsch, R., Glover, S. C. O., and Klessen, R. S. (Nov. 2018). The SILCC project - V. The impact of magnetic fields on the chemistry and the formation of molecular clouds. *Monthly Notices of the Royal Astronomical Society* 480(3), 3511–3540.

Girichidis, P., Walch, S., Naab, T., Gatto, A., Wünsch, R., Glover, S. C. O., Klessen, R. S., Clark, P. C., Peters, T., Derigs, D., and Baczynski, C. (Mar. 2016). The SILCC (SImulating the LifeCycle of molecular Clouds) project - II. Dynamical evolution of the supernova-driven ISM and the launching of outflows. *Monthly Notices of the Royal Astronomical Society* 456(4), 3432–3455.

Gómez, G. C. and Vázquez-Semadeni, E. (Aug. 2014). Filaments in Simulations of Molecular Cloud Formation. *The Astrophysical Journal* 791(2) 124, 124.

Grisdale, K. (Jan. 2021). Physical properties and scaling relations of molecular clouds: the impact of star formation. *Monthly Notices of the Royal Astronomical Society* 500(3), 3552–3568.

Großschedl, J. E., Alves, J., Meingast, S., Ackerl, C., Ascenso, J., Bouy, H., Burkert, A., Forbrich, J., Fürnkranz, V., Goodman, A., Hacar, Á., Herbst-Kiss, G., Lada, C. J., Larreina, I., Leschinski, K., Lombardi, M., Moitinho, A., Mortimer, D., and Zari, E. (Nov. 2018). 3D shape of Orion A from Gaia DR2. *Astronomy and Astrophysics* 619 A106, A106.

Grudić, M. Y., Guszejnov, D., Offner, S. S. R., Rosen, A. L., Raju, A. N., Faucher-Giguère, C.-A., and Hopkins, P. F. (May 2022). The dynamics and outcome of star formation with jets, radiation, winds, and supernovae in concert. *Monthly Notices of the Royal Astronomical Society* 512(1), 216–232.

Guszejnov, D., Markey, C., Offner, S. S. R., Grudić, M. Y., Faucher-Giguère, C.-A., Rosen, A. L., and Hopkins, P. F. (Sept. 2022). Cluster assembly and the origin of mass segregation in the STARFORGE simulations. *Monthly Notices of the Royal Astronomical Society* 515(1), 167–184.

Hacar, A., Clark, S., Heitsch, F., Kainulainen, J., Panopoulou, G., Seifried, D., and Smith, R. (Mar. 2022). Initial Conditions for Star Formation: A Physical Description of the Filamentary ISM. *arXiv e-prints* arXiv:2203.09562, arXiv:2203.09562.

Haffner, L. M., Reynolds, R. J., Tufte, S. L., Madsen, G. J., Jaehnig, K. P., and Percival, J. W. (Dec. 2003). The Wisconsin Hα Mapper Northern Sky Survey. *The Astrophysical Journal Supplement Series* 149(2), 405–422. ISSN: 1538-4365.

Han, D., Kimm, T., Katz, H., Devriendt, J., and Slyz, A. (July 2022). Impact of Radiation Feedback on the Formation of Globular Cluster Candidates during Cloud-Cloud Collisions. *arXiv e-prints* arXiv:2207.05745, arXiv:2207.05745.

He, H., Wilson, C., Brunetti, N., Finn, M., Bemis, A., and Johnson, K. (Mar. 2022). Embedded Young Massive Star Clusters in the Antennae Merger. *The Astrophysical Journal* 928(1) 57, 57.

Hennemann, M., Motte, F., Bontemps, S., Schneider, N., Csengeri, T., Balog, Z., di Francesco, J., Zavagno, A., André, P., Men'shchikov, A., Abergel, A., Ali, B., Baluteau, J. P., Bernard, J. P., Cox, P., Didelon, P., di Giorgio, A. M., Griffin, M., Hargrave, P., Hill, T., Horeau, B., Huang, M., Kirk, J., Leeks, S., Li, J. Z., Marston, A., Martin, P., Molinari, S., Nguyen Luong, Q., Olofsson, G., Persi, P., Pezzuto, S., Russeil, D., Saraceno, P., Sauvage, M., Sibthorpe, B., Spinoglio, L., Testi, L., Ward-Thompson, D., White, G., Wilson, C., and Woodcraft, A. (July 2010). Herschel observations of embedded protostellar clusters in the Rosette molecular cloud. *Astronomy and Astrophysics* 518 L84, L84.

Henning, T., Linz, H., Krause, O., Ragan, S., Beuther, H., Launhardt, R., Nielbock, M., and Vasyunina, T. (July 2010). The seeds of star formation in the filamentary infrared-dark cloud G011.11-0.12. *Astronomy & Astrophysics* 518 L95, L95.

Hockney, R. W. and Eastwood, J. W. (1981). *Computer Simulation Using Particles*.

Houde, M., Dowell, C. D., Hildebrand, R. H., Dotson, J. L., Vaillancourt, J. E., Phillips, T. G., Peng, R., and Bastien, P. (Apr. 2004). Tracing the Magnetic Field in Orion A. *The Astrophysical Journal* 604(2), 717–740.

Howard, C. S., Pudritz, R. E., and Harris, W. E. (2018). A universal route for the formation of massive star clusters in giant molecular clouds. *Nature Astronomy* 2, 725–730.

Hoyle, F. and Lyttleton, R. A. (Jan. 1939). The effect of interstellar matter on climatic variation. *Proceedings of the Cambridge Philosophical Society* 35(3), 405.

Jeffreson, S., Kruijssen, J., Keller, B., Chévance, M., and C.O., G. S. (2020). The role of galactic dynamics in shaping the physical properties of giant molecular clouds in Milky Way-like galaxies. *Monthly Notices of the Royal Astronomical Society* 498, 385*429.

Johnstone, D., Di Francesco, J., and Kirk, H. (Aug. 2004). An Extinction Threshold for Protostellar Cores in Ophiuchus. *The Astrophysical Journal* 611(1), L45–L48.

Kainulainen, J., Federrath, C., and Henning, T. (Apr. 2014). Unfolding the Laws of Star Formation: The Density Distribution of Molecular Clouds. *Science* 344(6180), 183–185.

Khokhlov, A. (1998a). Fully threaded tree algorithms for adaptive mesh refinement fluid dynamics simulations. *Journal of Computational Physics* 143, 519–543.

Khokhlov, A. (July 1998b). Fully Threaded Tree Algorithms for Adaptive Refinement Fluid Dynamics Simulations. *Journal of Computational Physics* 143(2), 519–543.

Kim, C.-G. and Ostriker, E. C. (Sept. 2017). Three-phase Interstellar Medium in Galaxies Resolving Evolution with Star Formation and Supernova Feedback (TIGRESS): Algorithms, Fiducial Model, and Convergence. *The Astrophysical Journal* 846(2) 133, 133.

King, P. K., Chen, C.-Y., Fissel, L. M., and Li, Z.-Y. (Dec. 2019). Effects of grain alignment efficiency on synthetic dust polarization observations of molecular clouds. *Monthly Notices of the Royal Astronomical Society* 490(2), 2760–2778.

Kitsionas, S., Federrath, C., Klessen, R. S., Schmidt, W., Price, D. J., Dursi, L. J., Gritschneder, M., Walch, S., Piontek, R., Kim, J., and al., et (2009). Algorithmic comparisons of decaying, isothermal, supersonic turbulence. *Astronomy & Astrophysics* 508, 541–560.

Klassen, M., Pudritz, R. E., and Peters, T. (2012). Simulating protostellar evolution and radiative feedback in the cluster environment. *Monthly Notices of the Royal Astronomical Society* 421, 2861–2871.

Klessen, R. S. and Glover, S. C. O. (Jan. 2016). Physical Processes in the Interstellar Medium. *Saas-Fee Advanced Course* 43, 85.

Körtgen, B., Banerjee, R., Pudritz, R. E., and Schmidt, W. (Nov. 2019). Global dynamics of the interstellar medium in magnetized disc galaxies. *Monthly Notices of the Royal Astronomical Society* 489(4), 5004–5021.

Kravtsov, A. V., Klypin, A. A., and Khokhlov, A. M. (July 1997). Adaptive Refinement Tree: A New High-Resolution N-Body Code for Cosmological Simulations. *The Astrophysical Journal Supplements* 111(1), 73–94.

Krumholz, M. R., McKee, C. F., and Bland-Hawthorn, J. (Aug. 2019). Star Clusters Across Cosmic Time. *Annual Review of Astronomy and Astrophysics* 57, 227–303.

Krumholz, M. R., McKee, C. F., and Klein, R. I. (Jan. 2005). How Protostellar Outflows Help Massive Stars Form. *The Astrophysical Journal Letters* 618(1), L33–L36.

Kuiper, R. and Hosokawa, T. (Aug. 2018). First hydrodynamics simulations of radiation forces and photoionization feedback in massive star formation. *Astronomy and Astrophysics* 616 A101, A101.

Kumar, M. S. N., Arzoumanian, D., Men'shchikov, A., Palmeirim, P., Matsumura, M., and Inutsuka, S. (Feb. 2022). Filament coalescence and hub structure in Mon R2. Implications for massive star and cluster formation. *Astronomy & Astrophysics* 658 A114, A114.

Kumar, M. S. N., Palmeirim, P., Arzoumanian, D., and Inutsuka, S. I. (Oct. 2020). Unifying low- and high-mass star formation through density-amplified hubs of filaments. The highest mass stars (>100 $M_\odot$) form only in hubs. *Astronomy & Astrophysics* 642 A87, A87.

Kwon, W. et al. (Feb. 2022). B-fields in Star-forming Region Observations (BISTRO): Magnetic Fields in the Filamentary Structures of Serpens Main. *The Astrophysical Journal* 926(2) 163, 163.

Lada, C. J. (Oct. 1976). Detailed observations of the M17 molecular cloud complex. *The Astrophysical Journal Supplement* 32, 603–629.

Lada, C. J. and Lada, E. A. (2003). Embedded Clusters in Molecular Clouds. *Annual Review of Astronomy & Astrophysics* 41, 51–115.

Lane, H. B., Grudić, M. Y., Guszejnov, D., Offner, S. S. R., Faucher-Giguère, C.-A., and Rosen, A. L. (Mar. 2022). Less wrong: a more realistic initial condition for simulations of turbulent molecular clouds. *Monthly Notices of the Royal Astronomical Society* 510(4), 4767–4778.

Larson, R. B. (Mar. 1981). Turbulence and star formation in molecular clouds. *Monthly Notices of the Royal Astronomical Society* 194, 809–826.

Larson, R. B. (Jan. 1969). Numerical calculations of the dynamics of collapsing proto-star. *Monthly Notices of the Royal Astronomical Society* 145, 271.

Lee, J. C., Whitmore, B. C., Thilker, D. A., Deger, S., Larson, K. L., Ubeda, L., Anand, G. S., Boquien, M., Chandar, R., Dale, D. A., Emsellem, E., Leroy, A. K., Rosolowsky, E., Schinnerer, E., Schmidt, J., Lilly, J., Turner, J., Van Dyk, S., White, R. L., Barnes, A. T., Belfiore, F., Bigiel, F., Blanc, G. A., Cao, Y., Chevance, M., Congiu, E., Egorov, O. V., Glover, S. C. O., Grasha, K., Groves, B., Henshaw, J. D., Hughes, A., Klessen, R. S., Koch, E., Kreckel, K., Kruijssen, J. M. D., Liu, D., Lopez, L. A., Mayker, N., Meidt, S. E., Murphy, E. J., Pan, H.-A., Pety, J., Querejeta, M., Razza, A., Saito, T., Sánchez-Blázquez, P., Santoro, F., Sardone, A., Scheuermann, F., Schruba, A., Sun, J., Usero, A., Watkins, E., and Williams, T. G. (Jan. 2022). The PHANGS-HST Survey: Physics at High Angular Resolution in Nearby Galaxies with the Hubble Space Telescope. *The Astrophysical Journal Supplement Series* 258(1) 10, 10.

Li, H., Gnedin, O. Y., and Gnedin, N. Y. (July 2018). Star Cluster Formation in Cosmological Simulations. II. Effects of Star Formation Efficiency and Stellar Feedback. *The Astrophysical Journal* 861(2) 107, 107.

Li, H., Gnedin, O. Y., Gnedin, N. Y., Meng, X., Semenov, V. A., and Kravtsov, A. V. (Jan. 2017). Star Cluster Formation in Cosmological Simulations. I. Properties of Young Clusters. *The Astrophysical Journal* 834(1) 69, 69.

Lombardi, M., Alves, J., and Lada, C. J. (Aug. 2006). 2MASS wide field extinction maps. I. The Pipe nebula. *Astronomy & Astrophysics* 454(3), 781–796.

Lombardi, M., Alves, J., and Lada, C. J. (Nov. 2011). 2MASS wide field extinction maps. IV. The Orion, Monoceros R2, Rosette, and Canis Major star forming regions. *Astronomy and Astrophysics* 535 A16, A16.

Lombardi, M., Bouy, H., Alves, J., and Lada, C. J. (June 2014). Herschel-Planck dust optical-depth and column-density maps. I. Method description and results for Orion. *Astronomy and Astrophysics* 566 A45, A45.

Lopez, L. A., Krumholz, M. R., Bolatto, A. D., Prochaska, J. X., and Ramirez-Ruiz, E. (Apr. 2011). What Drives the Expansion of Giant H II Regions?: A Study of Stellar Feedback in 30 Doradus. *The Astrophysical Journal* 731(2) 91, 91.

Lucas, W. E., Bonnell, I. A., and Dale, J. E. (Apr. 2020). Supernova feedback and the energy deposition in molecular clouds. *Monthly Notices of the Royal Astronomical Society* 493(4), 4700–4710.

Lue, A., Guszejnov, D., Offner, S. S. R., and Grudić, M. Y. (Oct. 2021). Evolution of the Gas Density in a Simulated Star-forming Cloud with Stellar Feedback. *Research Notes of the American Astronomical Society* 5(10) 225, 225.

Mac Low, M.-M. and Klessen, R. S. (Jan. 2004). Control of star formation by supersonic turbulence. *Reviews of Modern Physics* 76(1), 125–194.

Massey, P. and Hunter, D. A. (Jan. 1998). Star Formation in R136: A Cluster of O3 Stars Revealed by Hubble Space Telescope Spectroscopy. *The Astrophysical Journal* 493(1), 180–194.

Masson, J., Teyssier, R., Mulet-Marquis, C., Hennebelle, P., and Chabrier, G. (Aug. 2012). Incorporating Ambipolar and Ohmic Diffusion in the AMR MHD Code RAMSES. *The Astrophysical Journal Supplement Series* 201(2) 24, 24.

McClure-Griffiths, N. M., Dickey, J. M., Gaensler, B. M., Green, A. J., and Haverkorn, M. (Dec. 2006). Magnetically Dominated Strands of Cold Hydrogen in the Riegel-Crutcher Cloud. *The Astrophysical Journal* 652(2), 1339–1347.

McKee, C. F. and Ostriker, E. C. (Sept. 2007). Theory of Star Formation. *Annual Review of Astronomy and Astrophysics* 45(1), 565–687.

Men'shchikov, A., André, P., Didelon, P., Könyves, V., Schneider, N., Motte, F., Bontemps, S., Arzoumanian, D., Attard, M., Abergel, A., Baluteau, J. .-., Bernard, J. .-., Cambrésy, L., Cox, P., di Francesco, J., di Giorgio, A. M., Griffin, M., Hargrave, P., Huang, M., Kirk, J., Li, J. Z., Martin, P., Minier, V., Miville-Deschênes, M. .-., Molinari, S., Olofsson, G., Pezzuto, S., Roussel, H., Russeil, D., Saraceno, P., Sauvage, M., Sibthorpe, B., Spinoglio, L., Testi, L., Ward-Thompson, D., White, G., Wilson, C. D., Woodcraft, A., and Zavagno, A. (July 2010). Filamentary structures and compact objects in the Aquila and Polaris clouds observed by Herschel. *Astronomy & Astrophysics* 518 L103, L103.

Molinari, S. et al. (July 2010). Clouds, filaments, and protostars: The Herschel Hi-GAL Milky Way. *Astronomy & Astrophysics* 518 L100, L100.

Motte, F., Zavagno, A., Bontemps, S., Schneider, N., Hennemann, M., di Francesco, J., André, P., Saraceno, P., Griffin, M., Marston, A., Ward-Thompson, D., White, G., Minier, V., Men'shchikov, A., Hill, T., Abergel, A., Anderson, L. D., Aussel, H., Balog, Z., Baluteau, J. P., Bernard, J. P., Cox, P., Csengeri, T., Deharveng, L., Didelon, P., di Giorgio, A. M., Hargrave, P., Huang, M., Kirk, J., Leeks, S., Li, J. Z., Martin, P., Molinari, S., Nguyen-Luong, Q., Olofsson, G., Persi, P., Peretto, N., Pezzuto, S., Roussel, H., Russeil, D., Sadavoy, S., Sauvage, M., Sibthorpe, B., Spinoglio, L., Testi, L., Teyssier, D., Vavrek, R., Wilson, C. D., and Woodcraft, A. (July 2010). Initial highlights of the HOBYS key program, the Herschel imaging survey of OB young stellar objects. *Astronomy & Astrophysics* 518 L77, L77.

Motte, F., Bontemps, S., and Louvet, F. (Sept. 2018). High-Mass Star and Massive Cluster Formation in the Milky Way. *Annual Review of Astronomy & Astrophysics* 56, 41–82.

Mouschovias, T. C. and Spitzer L., J. (Dec. 1976). Note on the collapse of magnetic interstellar clouds. *The Astrophysical Journal* 210, 326.

Myers, P. C. (Aug. 2009). Filamentary Structure of Star-forming Complexes. *The Astrophysical Journal* 700(2), 1609–1625.

Nakano, T. and Nakamura, T. (Jan. 1978). Gravitational Instability of Magnetized Gaseous Disks 6. *Publications of the Astronomical Society of Japan* 30, 671–680.

Nordlund, A., Ramsey, J. P., Popovas, A., and Küffmeier, M. (2018). DISPATCH: A numerical simulation framework for the exa-scale era. I. Fundamentals. *Monthly Notices of the Royal Astronomical Society* 477, 624–638.

Ntormousi, E. and Hennebelle, P. (May 2019). Core and stellar mass functions in massive collapsing filaments. *Astronomy and Astrophysics* 625 A82, A82.

Padoan, P., Pan, L., Haugbølle, T., and Nordlund, Å. (May 2016). Supernova Driving. I. The Origin of Molecular Cloud Turbulence. *The Astrophysical Journal* 822(1) 11, 11.

Pattle, K., Fissel, L., Tahani, M., Liu, T., and Ntormousi, E. (Mar. 2022). Magnetic fields in star formation: from clouds to cores. *arXiv e-prints* arXiv:2203.11179, arXiv:2203.11179.

Peretto, N., Fuller, G. A., Duarte-Cabral, A., Avison, A., Hennebelle, P., Pineda, J. E., André, P., Bontemps, S., Motte, F., Schneider, N., and Molinari, S. (July 2013). Global collapse of molecular clouds as a formation mechanism for the most massive stars. *Astronomy & Astrophysics* 555 A112, A112.

Pfeffer, J., Bastian, N., Kruijssen, J. M. D., Reina-Campos, M., Crain, R. A., and Usher, C. (Dec. 2019). Young star cluster populations in the E-MOSAICS simulations. *Monthly Notices of the Royal Astronomical Society* 490(2), 1714–1733.

Pillai, T. G. S., Clemens, D. P., Reissl, S., Myers, P. C., Kauffmann, J., Lopez-Rodriguez, E., Alves, F. O., Franco, G. A. P., Henshaw, J., Menten, K. M., Nakamura, F., Seifried, D., Sugitani, K., and Wiesemeyer, H. (Jan. 2020). Magnetized filamentary gas flows feeding the young embedded cluster in Serpens South. *Nature Astronomy* 4, 1195–1201.

Pineda, J. E., Arzoumanian, D., André, P., Friesen, R. K., Zavagno, A., Clarke, S. D., Inoue, T., Chen, C.-Y., Lee, Y.-N., Soler, J. D., and Kuffmeier, M. (May 2022). From Bubbles and Filaments to Cores and Disks: Gas Gathering and Growth of Structure Leading to the Formation of Stellar Systems. *arXiv e-prints* arXiv:2205.03935, arXiv:2205.03935.

Pineda, J. E., Caselli, P., and Goodman, A. A. (May 2008). CO Isotopologues in the Perseus Molecular Cloud Complex: the X-factor and Regional Variations. *The Astrophysical Journal* 679(1), 481–496.

Pineda, J. E., Goodman, A. A., Arce, H. G., Caselli, P., Foster, J. B., Myers, P. C., and Rosolowsky, E. W. (Mar. 2010). Direct Observation of a Sharp Transition to Coherence in Dense Cores. *The Astrophysical Journal* 712(1), L116–L121.

Pineda, J. E., Goodman, A. A., Arce, H. G., Caselli, P., Longmore, S., and Corder, S. (Sept. 2011). Expanded Very Large Array Observations of the Barnard 5 Star-forming Core: Embedded Filaments Revealed. *The Astrophysical Journal* 739(1) L2, L2.

Polychroni, D., Schisano, E., Elia, D., Roy, A., Molinari, S., Martin, P., André, P., Turrini, D., Rygl, K. L. J., Di Francesco, J., Benedettini, M., Busquet, G., di Giorgio, A. M., Pestalozzi, M., Pezzuto, S., Arzoumanian, D., Bontemps, S., Hennemann, M.,

Hill, T., Könyves, V., Men'shchikov, A., Motte, F., Nguyen-Luong, Q., Peretto, N., Schneider, N., and White, G. (Nov. 2013). Two Mass Distributions in the L 1641 Molecular Clouds: The Herschel Connection of Dense Cores and Filaments in Orion A. *The Astrophysical Journal Letters* 777(2) L33, L33.

Ramírez-Galeano, L., Ballesteros-Paredes, J., Smith, R. J., Camacho, V., and Zamora-Avilés, M. (Sept. 2022). Why most molecular clouds are gravitationally dominated. *Monthly Notices of the Royal Astronomical Society* 515(2), 2822–2836.

Rathjen, T.-E., Naab, T., Girichidis, P., Walch, S., Wünsch, R., Dinnbier, F., Seifried, D., Klessen, R. S., and Glover, S. C. O. (June 2021). SILCC VI - Multiphase ISM structure, stellar clustering, and outflows with supernovae, stellar winds, ionizing radiation, and cosmic rays. *Monthly Notices of the Royal Astronomical Society* 504(1), 1039–1061.

Reina-Campos, M., Keller, B. W., Kruijssen, J. M. D., Gensior, J., Trujillo-Gomez, S., Jeffreson, S. M. R., Pfeffer, J. L., and Sills, A. (July 2022). Introducing EMP-Pathfinder: modelling the simultaneous formation and evolution of stellar clusters in their host galaxies. *Monthly Notices of the Royal Astronomical Society*.

Reina-Campos, M., Kruijssen, J. M. D., Pfeffer, J. L., Bastian, N., and Crain, R. A. (July 2019). Formation histories of stars, clusters, and globular clusters in the E-MOSAICS simulations. *Monthly Notices of the Royal Astronomical Society* 486(4), 5838–5852.

Rezaei Kh., S., Bailer-Jones, C. A. L., Soler, J. D., and Zari, E. (Nov. 2020). Detailed 3D structure of Orion A in dust with Gaia DR2. *Astronomy & Astrophysics* 643 A151, A151.

Rieder, S., Dobbs, C., Bending, T., Liow, K. Y., and Wurster, J. (Feb. 2022). The formation and early evolution of embedded star clusters in spiral galaxies. *Monthly Notices of the Royal Astronomical Society* 509(4), 6155–6168.

Sakre, N., Habe, A., Pettitt, A. R., and Okamoto, T. (Jan. 2021). Massive core/star formation triggered by cloud-cloud collision: Effect of magnetic field. *Publications of the Astronomical Society of Japan* 73, S385–S404.

Saltzman, J. (1994). An Unsplit 3D Upwind Method for Hyperbolic Conservation Laws. *Journal of Computational Physics* 115(1), 153–168. ISSN: 0021-9991.

Sarkar, S. and Jog, C. J. (Oct. 2018). The constraining effect of gas and the dark matter halo on the vertical stellar distribution of the Milky Way. *Astronomy and Astrophysics* 617 A142, A142.

Schive, H.-Y., Tsai, Y.-C., and Chiueh, T. (2010). Gamer: A graphic processing unit accelerated adaptive mesh refinement code for astrophysics. *The Astrophysical Journal Supplement Series* 186, 457–484.

Schmidt, W., Federrath, C., Hupp, M., Kern, S., and Niemeyer, J. C. (Jan. 2009). Numerical simulations of compressively driven interstellar turbulence. I. Isothermal gas. *Astronomy and Astrophysics* 494(1), 127–145.

Schneider, N., Csengeri, T., Hennemann, M., Motte, F., Didelon, P., Federrath, C., Bontemps, S., Di Francesco, J., Arzoumanian, D., Minier, V., André, P., Hill, T., Zavagno, A., Nguyen-Luong, Q., Attard, M., Bernard, J. .-., Elia, D., Fallscheer, C., Griffin, M., Kirk, J., Klessen, R., Könyves, V., Martin, P., Men'shchikov, A., Palmeirim, P., Peretto, N., Pestalozzi, M., Russeil, D., Sadavoy, S., Sousbie, T.,

Testi, L., Tremblin, P., Ward-Thompson, D., and White, G. (Apr. 2012). Cluster-formation in the Rosette molecular cloud at the junctions of filaments. *Astronomy & Astrophysics* 540 L11, L11.

Seifried, D., Walch, S., Girichidis, P., Naab, T., Wünsch, R., Klessen, R. S., Glover, S. C. O., Peters, T., and Clark, P. (Dec. 2017). SILCC-Zoom: the dynamic and chemical evolution of molecular clouds. *Monthly Notices of the Royal Astronomical Society* 472(4), 4797–4818.

Smith, B. D., Bryan, G. L., Glover, S. C. O., Goldbaum, N. J., Turk, M. J., Regan, J., Wise, J. H., Schive, H.-Y., Abel, T., Emerick, A., O'Shea, B. W., Anninos, P., Hummels, C. B., and Khochfar, S. (Apr. 2017). GRACKLE: a chemistry and cooling library for astrophysics. *Monthly Notices of the Royal Astronomical Society* 466(2), 2217–2234.

Smith, M. C., Bryan, G. L., Somerville, R. S., Hu, C.-Y., Teyssier, R., Burkhart, B., and Hernquist, L. (Sept. 2021). Efficient early stellar feedback can suppress galactic outflows by reducing supernova clustering. *Monthly Notices of the Royal Astronomical Society* 506(3), 3882–3915.

Smith, R. J., Shetty, R., Stutz, A. M., and Klessen, R. S. (May 2012). Line Profiles of Cores within Clusters. I. The Anatomy of a Filament. *The Astrophysical Journal* 750(1) 64, 64.

Soler, J. D., Miville-Deschênes, M. .-., Molinari, S., Klessen, R. S., Hennebelle, P., Testi, L., McClure-Griffiths, N. M., Beuther, H., Elia, D., Schisano, E., Traficante, A., Girichidis, P., Glover, S. C. O., Smith, R. J., Sormani, M., and Treß, R. (June 2022). The Galactic dynamics revealed by the filamentary structure in atomic hydrogen emission. *Astronomy and Astrophysics* 662 A96, A96.

Soler, J. D. (Sept. 2019). Using Herschel and Planck observations to delineate the role of magnetic fields in molecular cloud structure. *Astronomy & Astrophysics* 629 A96, A96.

Stahler, S. and Palla, F. (Jan. 2005). The Formation of Stars. *The Formation of Stars, by Steven W. Stahler, Francesco Palla, pp. 865. ISBN 3-527-40559-3. Wiley-VCH , January 2005.*

Sullivan, C. H., Fissel, L. M., King, P. K., Chen, C. .-., Li, Z. .-., and Soler, J. D. (May 2021). Characterizing the magnetic fields of nearby molecular clouds using submillimeter polarization observations. *Monthly Notices of the Royal Astronomical Society* 503(4), 5006–5024.

Sun, J., Leroy, A. K., Rosolowsky, E., Hughes, A., Schinnerer, E., Schruba, A., Koch, E. W., Blanc, G. A., Chiang, I.-D., Groves, B., Liu, D., Meidt, S., Pan, H.-A., Pety, J., Querejeta, M., Saito, T., Sandstrom, K., Sardone, A., Usero, A., Utomo, D., Williams, T. G., Barnes, A. T., Benincasa, S. M., Bigiel, F., Bolatto, A. D., Boquien, M., Chevance, M., Dale, D. A., Deger, S., Emsellem, E., Glover, S. C. O., Grasha, K., Henshaw, J. D., Klessen, R. S., Kreckel, K., Kruijssen, J. M. D., Ostriker, E. C., and Thilker, D. A. (June 2022). Molecular Cloud Populations in the Context of Their Host Galaxy Environments: A Multiwavelength Perspective. *arXiv e-prints* arXiv:2206.07055, arXiv:2206.07055.

Tahani, M., Glover, J., Lupypciw, W., West, J. L., Kothes, R., Plume, R., Inutsuka, S., Lee, M. .-., Grenier, I. A., Knee, L. B. G., Brown, J. C., Doi, Y., Robishaw, T., and Haverkorn, M. (Apr. 2022). Orion A's complete 3D magnetic field morphology. *Astronomy & Astrophysics* 660 L7, L7.

Tahani, M., Plume, R., Brown, J. C., and Kainulainen, J. (June 2018). Helical magnetic fields in molecular clouds?. A new method to determine the line-of-sight magnetic field structure in molecular clouds. *Astronomy and Astrophysics* 614 A100, A100.

Tahani, M., Plume, R., Brown, J. C., Soler, J. D., and Kainulainen, J. (Dec. 2019). Could bow-shaped magnetic morphologies surround filamentary molecular clouds?. The 3D magnetic field structure of Orion-A. *Astronomy and Astrophysics* 632 A68, A68.

Teyssier, R. (2002). Cosmological Hydrodynamics with Adaptive Mesh Refinement. *Astronomy and Astrophysics* 385, 337–364.

Teyssier, R. (Aug. 2015). Grid-Based Hydrodynamics in Astrophysical Fluid Flows. *Annual Review of Astronomy and Astrophysics* 53, 325–364.

Theissen, C. A., Konopacky, Q. M., Lu, J. R., Kim, D., Zhang, S. Y., Hsu, C.-C., Chu, L., and Wei, L. (Feb. 2022). The 3D Kinematics of the Orion Nebula Cluster: NIRSPEC-AO Radial Velocities of the Core Population. *The Astrophysical Journal* 926(2) 141, 141.

Thilker, D. A., Whitmore, B. C., Lee, J. C., Deger, S., Chandar, R., Larson, K. L., Hannon, S., Ubeda, L., Dale, D. A., Glover, S. C. O., Grasha, K., Klessen, R., Kruijssen, J. M. D., Rosolowsky, E., Schruba, A., White, R. L., and Williams, T. G. (June 2021). PHANGS-HST: New Methods for Star Cluster Identification in Nearby Galaxies. *arXiv e-prints* 1 arXiv:2106.13366, arXiv:2106.13366.

Toro, E. (Jan. 2009). Riemann Solvers and Numerical Methods for Fluid Dynamics: A Practical Introduction. In:

Townsley, L. K., Broos, P. S., Garmire, G. P., Bouwman, J., Povich, M. S., Feigelson, E. D., Getman, K. V., and Kuhn, M. A. (July 2014). The Massive Star-Forming Regions Omnibus X-Ray Catalog. *The Astrophysical Journal Supplement* 213(1) 1, 1.

Truelove, J. K., Klein, R. I., McKee, C. F., Holliman, J. H., Howell, L. H., and Greenough, J. A. (1997). The Jeans condition: a new constraint on spatial resolution in simulations of isothermal self-gravitational hydrodynamics. *The Astrophysical Journal* 489, 179–183.

Turner, J. A., Dale, D. A., Lilly, J., Boquien, M., Deger, S., Lee, J. C., Whitmore, B. C., Anand, G. S., Benincasa, S. M., Bigiel, F., Blanc, G. A., Chevance, M., Emsellem, E., Faesi, C. M., Glover, S. C. O., Grasha, K., Hughes, A., Klessen, R. S., Kreckel, K., Kruijssen, J. M. D., Leroy, A. K., Pan, H.-A., Rosolowsky, E., Schruba, A., and Williams, T. G. (Nov. 2022). PHANGS: constraining star formation time-scales using the spatial correlations of star clusters and giant molecular clouds. *Monthly Notices of the Royal Astronomical Society* 516(3), 4612–4626.

Vázquez-Semadeni, E., Gómez, G. C., Jappsen, A. .-., Ballesteros-Paredes, J., and Klessen, R. S. (Dec. 2009). High- and Low-Mass Star-Forming Regions from Hierarchical Gravitational Fragmentation. High Local Star Formation Rates with Low Global Efficiencies. *The Astrophysical Journal* 707(2), 1023–1033.

Vázquez-Semadeni, E., González, R. F., Ballesteros-Paredes, J., Gazol, A., and Kim, J. (Oct. 2008). The nature of the velocity field in molecular clouds - I. The non-magnetic case. *Monthly Notices of the Royal Astronomical Society* 390(2), 769–780.

Vázquez-Semadeni, E., Palau, A., Ballesteros-Paredes, J., Gómez, G. C., and Zamora-Avilés, M. (Dec. 2019). Global hierarchical collapse in molecular clouds. Towards a comprehensive scenario. *Monthly Notices of the Royal Astronomical Society* 490(3), 3061–3097.

Villagran, M. A., Velázquez, P. F., Gómez, D. O., and Giacani, E. B. (Jan. 2020). Evolving supernova remnants in multiphase interstellar media. *Monthly Notices of the Royal Astronomical Society* 491(2), 2855–2863.

Weidner, C. and Kroupa, P. (2004). Evidence for a fundamental stellar upper mass limit from clustered star formation. *Monthly Notices of the Royal Astronomical Society* 348, 187–191.

Williams, G. M., Peretto, N., Avison, A., Duarte-Cabral, A., and Fuller, G. A. (May 2018). Gravity drives the evolution of infrared dark hubs: JVLA observations of SDC13. *Astronomy & Astrophysics* 613 A11, A11.

Wilson, R. W., Jefferts, K. B., and Penzias, A. A. (July 1970). Carbon Monoxide in the Orion Nebula. *The Astrophysical Journal Letters* 161, L43.

Young, K. E., Enoch, M. L., Evans Neal J., I., Glenn, J., Sargent, A., Huard, T. L., Aguirre, J., Golwala, S., Haig, D., Harvey, P., Laurent, G., Mauskopf, P., and Sayers, J. (June 2006). Bolocam Survey for 1.1 mm Dust Continuum Emission in the c2d Legacy Clouds. II. Ophiuchus. *The Astrophysical Journal* 644(1), 326–343.

Zhao, B., Pudritz, R. E., Pillsworth, R., Wadsley, J., and Robinson, H. (2022, in prep.). From Galaxy to Stars: Multiscale galactic simulations from GMCs to cluster formation.